THE ROLE OF MAGNETIC FIELD GRADIENTS IN NUCLEAR MAGNETIC RESONANCE

by

STANLEY DAVID LUCK

A THESIS SUBMITTED IN PARTIAL FULFILMENT OF
THE REQUIREMENTS FOR THE DEGREE OF
DOCTOR OF PHILOSOPHY

in

THE FACULTY OF GRADUATE STUDIES
Department of Chemistry

We accept this thesis as conforming
to the required standard

THE UNIVERSITY OF BRITISH COLUMBIA

November 17, 1986

In presenting this thesis in partial fulfilment of the requirements for an advanced degree at the The University of British Columbia, I agree that the Library shall make it freely available for reference and study. I further agree that permission for extensive copying of this thesis for scholarly purposes may be granted by the Head of my Department or by his or her representatives. It is understood that copying or publication of this thesis for financial gain shall not be allowed without my written permission.

Department of Chemistry

The University of British Columbia
2075 Wesbrook Place
Vancouver, Canada
V6T 1W5

Date: November 17, 1986

ABSTRACT

A high resolution NMR probe was modified with gradient coils (31 mm diameter) for the measurement of translational diffusion and for microscopic imaging, and a larger set of gradient coils (15 cm diameter) was constructed for surface coil diffusion measurements. The magnitudes of the gradients produced by these coils were determined from the linewidths and lineshapes of gradient spectra. In diffusion experiments using the pulsed gradient method of Stejskal and Tanner, induced eddy currents and slow variation of the magnetic field at the sample interfered with measurements at short echo times. For these experiments the known diffusion coefficient of water was used to determine the effective gradient in each experiment. The diffusion coefficient of acrylonitrile was measured from the decay of single, double and triple quantum echoes using a modified pulsed field gradient spin echo pulse sequence.

In the second part of this thesis, three examples of living systems were studied. The first involved the application of pulsed gradient spin echo measurements to characterize the motion of water and lipid, *in-vivo*, in human forearm. Spin echo spectra from human forearm gave a water signal that was attributed to extracellular water because of relatively long spin-spin relaxation time (0.8 s) compared to that of intracellular water (20-30 ms). Comparison of the diffusivity of water, from experiments at two different echo times suggest that the major part of the

motion of water, *in-vivo*, was due to directionally randomized bulk flow rather than molecular diffusion.

The second application involved the chemical shift resolved mapping of the proton distribution, in one-dimension, along the anteroposterior direction, of pupae of the Douglas-fir cone moth *Barbara colfaxiana*. Proton distribution maps showed that the distribution of the aqueous fluid depended upon the vertical orientation, head pointing upward or downward, of the pupae.

Finally, two dimensional images of mature caps of the marine alga *Acetabularia mediterranea* were obtained using the normal spin echo sequence as well as with T_1, T_2 and diffusion contrasting. D_2O-contrasting was obtained by briefly submerging the caps in D_2O. All of these images showed features resembling the radial structure of the caps. The resolution was estimated by comparison with microscopic views of the caps and was found to be 0.1 mm, determined as the smallest distinguishable feature in the image.

14.I.87

Table of Contents

LIST OF TABLES

LIST OF FIGURES

ACKNOWLEDGEMENTS

It is a pleasure to acknowledge many interesting and stimulating discussions with Dr. Laurie Hall. Special thanks are given to Dr. Lionel Harrison without whose ideas and efforts this thesis would not have come to fruition, to Dr. Robert Snider for many interesting discussions and for his critical comments, and to Tom Markus, Emil Matter and Cedric Neale for their beautiful work without which these experiments would not have been possible. I wish to thank V. Rajanayagam for his instruction in the art of imaging and assistance in running numerous biological samples, S. Talagala for discussions about how NMR imaging really works, and finally all of the other members of the lab who shared in the joys and sorrows of graduate school. Finally, special thanks to my wife, Ada, for her invaluable assistance in preparing this thesis.

I. INTRODUCTION

1. OVERVIEW

In the developing technologies for nuclear magnetic resonance (NMR) imaging and localized spectroscopy which have applications in medicine and biology, radiofrequency (rf) excitation and magnetic field gradients play key roles *(1-4)*. The importance of the radiofrequency excitation is in the generation of NMR signals whereas magnetic field gradients are applied to characterize the spatial location of the spins. In pulsed NMR methods, pulsed gradients and rf pulses are often combined to produce various kinds of spin echoes. Spin echoes are important because they offer a convenient means for the observation of the time dependence associated with the motion of the spins including translational diffusion and bulk flow *(5-9)*, and for so-called phase-encoding in multidimensional Fourier transform NMR *(10)*.

The first part of this thesis describes the modification of a high resolution NMR probe with gradient coils (31 mm diameter) for the measurement of translational diffusion and for microscopic imaging, and the construction of a larger set of gradient coils (15 cm diameter) to be used in a wide bore magnet for surface coil diffusion measurements. The smaller size of these gradient coils compared to those built into the respective superconducting magnets allows the generation of larger gradients with

shorter rise times. The magnitudes of the gradients produced by these coils were determined from the linewidths and the lineshapes of gradient spectra. These are NMR spectra obtained with the appropriate gradient applied to give a one-dimensional projection of the spin distribution. From these values and using the high resolution apparatus, an absolute value for the diffusion coefficient of water, 2.23×10^{-9} m^2s^{-1} at 23 °C, was obtained in a static gradient diffusion experiment. This value is in good agreement with the literature value of 2.19×10^{-9} m^2s^{-1} from tracer diffusion *(11)*.

The static gradient method for determining diffusion coefficients involves the application of a magnetic field gradient for the duration of the experiment and gives rise to inhomogeneously broadened lines, prohibiting measurements on multicomponent systems such as would be found in biological systems containing water and lipid. Consequently, the pulsed gradient method of Stejskal and Tanner *(12)*, in which gradient pulses are applied at specially timed intervals allowing the measurement of high resolution spectra, was implemented. It is then possible to simultaneously determine the diffusion coefficients of the different chemical components in the sample. Unlike the static gradient method, the pulsed gradient method is subject to the slower response of the magnetic field at the sample compared to the time for switching of the current passing through the gradient coils. By making measurements

for increasing time intervals after the application of gradient pulses, spin echo measurements provided a simple means for determining the settling times of the magnetic field at the sample. The cause of the slow response of the magnetic field was not investigated but interactions with either the large static field from the superconducting magnet, the shim coils and their power supplies, or the surrounding metal in the bore of the magnet may be responsible. It was found that by using sufficiently long delays after the gradient pulses, accurate diffusion measurements could be obtained using the pulsed gradient technique. Using the high resolution apparatus, the pulsed gradient method was used to determine the diffusion coefficients of D-glucose, 6.70×10^{-10} m^2s^{-1} (at infinite dilution) and dextran (T-10, MW 9000, 4.3 % W/V in D_2O), 6.24×10^{-11} m^2s^{-1}, and these were in agreement with the literature values of 6.75×10^{-10} *(117,118)* and 6.3×10^{-11} m^2s^{-1} *(102)* respectively.

Also, a modified pulsed gradient spin echo method was used to determine the diffusion coefficient of acrylonitrile from the decay of single, double and triple quantum echoes. As expected the higher order coherences are more sensitive to the applied gradient.

For the surface coil apparatus with the larger gradient coils, the eddy current effects were more severe and pulsed gradient spin echo measurements could be performed with less accuracy and precision. Using echo times of 220 ms,

diffusion coefficients for a 4:1 mixture of water and ethanol gave values which agreed within only 10 % of the values determined using the high resolution apparatus.

In imaging experiments, the imaging gradient serves to stabilize the formation of the echo; a strategy which has been used previously for diffusion measurements by Hrovat and Wade *(13)*. Thus imaging experiments with echo times as short as 7 ms could be performed. Using a model system of water and acetone it was demonstrated that accurate diffusion coefficients could be obtained from diffusion contrasting experiments.

Because NMR is a non-invasive technique without known serious effects on biological systems *(1-4)*, there is considerable interest in studying the spatial distribution and movements of substances *in-vivo*. Such systems can exhibit complexities of physicochemical behaviour quite different from the properties of inanimate chemical systems. The basic question addressed in the second part of this work is therefore: when one looks with field gradient NMR at living systems, what does one see?

Three examples of living systems have been studied in this work, each with a different kind of field gradient method and giving different kinds of information. Motion, both of water and of lipids, has been studied in a small region of the human forearm. If such measurements were made on a simple chemical solution one would expect to achieve a clear separation between bulk flow of the solution and

molecular diffusion. *In-vivo*, however, there can be many kinds of liquids which undergo bulk flows that are not random on the molecular scale, but in which numerous flow paths are randomized in direction on a spatial scale small compared to the total sample observed. Two examples are blood flow in small capillaries (as well as the poolings and back eddies which can randomize flow-rate and flow direction in somewhat larger veins) and intracellularly, cytoplasmic streaming. Does *in-vivo* field gradient NMR measure mainly these processes or true molecular diffusion?

For the human forearm study reported here, the answer is that neither for aqueous material nor for lipids was there very much contribution from true diffusion. Under the conditions required for accurate diffusion measurements, the signal due to intracellular water had decayed because of short T_2 relaxation times and the resulting spectra showed signals attributed to extracellular water and intracellular lipid. Consequently, the bulk flow of randomized direction measured for water protons is most probably blood flow. Lipids, on the other hand, move 100 times faster than expected from molecular diffusion in the time-scale of the experiment, and it is not clear what type of motion is involved.

The other two biological applications both use two-dimensional NMR methods. In this, the signal intensity is a function of two variables. In the first instance, these are two independent time intervals under the control of the

experimenter. By Fourier transformation, they can be converted into two frequencies and the resulting array of data constitutes a two dimensional spectrum. But ultimately, one of them is converted into a position along some fixed direction, and the other either into a chemical shift or into position in an orthogonal direction. In the first case, one can obtain simultaneous information on the distribution of two or more substances along one dimension of a organism. In the second case, one can obtain a two-dimensional projection of its shape. This thesis describes one *in-vivo* example of each kind of application of two-dimensional NMR.

Chemical shift imaging was used to distinguish distributions of the aqueous fluid and lipid along the anteroposterior direction of pupae of the Douglas Fir Cone Moth, *Barbara colfaxiana.* The aqueous fluid is the haemolymph, which serves the insect for the purposes of both the blood and the lymphatic system of higher animals. The simple experiment of turning pupae upside-down produced changes indicating a shift in the distribution of the haemolymph.

The very large single-celled marine alga *Acetabularia mediterranea,* at the culmination of its life cycle, produces a discoid reproductive cap which is a very suitable object for study with a good magnifying glass or the lowest powers of the optical microscope. It has features radially tapering in size from 0.3 mm near the rim to tens of microns near the center. This is a very suitable object for imaging

in two spatial dimensions to determine the spatial resolution actually achieved in the image. The size of its features challenges the present state-of-the-art limits of spatial resolution. Since there is no tomography, slice selection, or sectioning involved, NMR images and ordinary optical photographs can be compared in detail.

Proton NMR imaging, however, makes visible the roughly 95 % of such an organism which is water, while optical observation and photography sees the other 5%. It is perhaps remarkable that the NMR image and the photograph have any resemblance whatever to each other, beyond giving the shape of the outer margin of the object. In fact, they show a wealth of precisely corresponding details down to 0.1 mm dimensions. An object such as the *Acetabularia* cap, which is wet throughout, provides a good test of means of contrasting different types of water in the sample, in the NMR imaging, by relaxation times, diffusion rates, or rates of exchange with D_2O. The contrasts which exist are another property of living systems which have no close analogue in most simple chemical systems.

What does one see *in-vivo*? The current visibilities, in proton field-gradient NMR, seem to be:-

(1) A greater variety of directionally-randomized flows of water than the chemist envisages.

(2) Some rather generalized indications of differing physiological interactions of water, spatially resolved along one dimension; and a clear separation of aqueous and

lipid phases.

(3) Spatial features on the scale of observations with a good magnifying glass, even in an object which seems almost uniformly full of water.

2. HISTORICAL SURVEY: DIFFUSION AND FLOW

The study of molecular motion in liquids and of bulk flow began soon after the first observations of nuclear induction by the research groups of F. Bloch *(14)* and E.M. Purcell *(15)*. The capability of NMR to directly measure the translational motion of molecules arose from the discovery by E. Hahn of spin echoes *(16)*. Spin echoes are secondary signals produced by the application of two or more rf pulses in an NMR experiment. Hahn found that the decay of the spin echo was governed not only by spin-spin relaxation but also by the translational diffusion of the spins in the inevitably inhomogeneous field of the magnet. Motion of the spins or more precisely of the molecules containing the spins, in such a field is accompanied by the variation of the Larmor frequency of the spins. The random variation of frequency which is obtained in the presence of Brownian motion leads to an uncertainty in the phase of the spins and eventually to a decrease in the intensity of the spin echo. Shortly thereafter, Carr and Purcell *(17)* applied static gradients to determine the diffusion coefficient of water. Following a suggestion by McCall *et al*. *(18)*, Stejskal and Tanner developed an alternate method using pulsed field

gradients (PFGs) *(12)*. Further modifications involving multiple gradient pulses *(19)* and alternating gradient pulses *(20)* have also been described. More recently techniques using multiquantum (MQ) spin echoes have been used to measure diffusion in liquid crystals *(21, 22)*. The general theory of the measurement of diffusion by NMR was reviewed by Reeves *(23)* whilst the application to the study of restricted diffusion was reviewed by Tanner *(24)*.

All of these techniques require some means for determining the gradient magnitude to allow calculation of the diffusion coefficient from the variation in echo amplitude. Methods which have been used for the determination of gradient magnitudes include theoretical calculations from coil geometry without measurement *(25)*, measurements of resonant frequency as a function of position in the field with a sample of small dimensions *(26, 27)*, and from the shape of the free induction decay (FID) or spin echo signal *(17, 28)*. But because of the experimental difficulties in obtaining accurate values of gradient magnitudes, especially from the shape of the FID or spin-echo, calibration using the diffusion coefficient of water obtained from tracer diffusion data is still preferred *(29, 30)*.

Motion due to bulk flow and Brownian motion, by their nature, have different effects upon the spin dynamics. Translational diffusion causes the spin echo to decay whereas flow affects its phase *(5-9)*. The first experiments

with flowing liquids were reported by Suryan in 1950 *(31)*. The experiments involved measurements of the variation of the steady state signal with flow-rate for the determination of the spin-lattice relaxation time, T_1. The first measurements of blood flow *in-vivo* were performed by V. Kudravcev and R.L. Bowman *(32)* in human forearm using a two-magnet, time of flight technique and by J.R. Singer *(33)* in tails of mice using a technique similar to that of Suryan.

Later, J.R. Singer and T. Grover *(34)* exploited the properties of spin echoes to determine the velocity distribution function for blood-flow in rat tails and human fingers. Spin echoes have also been applied to the measurement of flowing water in plants *(35)*. By observing the variation in the amplitude of the steady-state signal, various experimental arrangements have been developed by Battocletti *et al.* to measure pulsatile arterial blood flow in many parts of the human body in real-time *(36)*. As described in the reviews by van As and Schaafsma *(37)* and Stepisnik *(38)* there is now interest in combining flow measurement with imaging.

3. HISTORICAL SURVEY: IMAGING

The concept that NMR data can reflect the shape of the sample was first discussed by Gabillard *(39)* who went on to study the NMR response from glass objects, filled with water, in the presence of gradients. The full realization of

the mapping of a spatial distribution of spins required three dimensions, and NMR imaging had to wait for the development of computers with the capability of handling large arrays of data.

In 1973 Lauterbur published work dealing with the two dimensional imaging, using a continuous wave method, of a set of capillaries *(40)*. The spectrum was scanned in the presence of a gradient with varying direction and the image was obtained by a projection reconstruction algorithm. Later, another method for imaging was developed by Kumar *et al. (41)* who showed how the properties of Fourier transformation, applied to the measured time response NMR signal, could be used to map spatial distribution. The strategy was to cause the time evolution of the spin system to vary as a function of two or more independent time intervals. The corresponding Fourier transformations would each yield one dimension of a multidimensional spectrum. This proved to be a very versatile scheme and has found much application in spectroscopic experiments where maps show correlations of the couplings between spins and with applied fields *(10,42)*. At the same time, Mansfield applied gradients for investigating periodic structures by the NMR diffraction method *(43)*. Further work has led to many variations of the NMR imaging process, and while some effort was made to develop methods for scanning through an object *(44,45)*, techniques using transient methods of detection and Fourier transformation have proven to be very versatile and

are favored *(1-4)*.

The range of application of NMR imaging is determined by several factors which affect image quality. These include signal to noise ratio and spatial resolution. To date, most of the work has dealt with biological systems because of the high abundance of mobile protons which also have high sensitivity *(1-4)*. Images of parts of the human body show detail that equals or even surpasses that of other techniques such as Computer Assisted Tomography (CAT) which involves scanning with X-rays. In CAT scans the radiation that passes through the object unabsorbed is detected. The scans show structure which reflects differing degrees of electron density. In NMR the signal that is measured arises from radiation that is first absorbed and then emitted by the nuclear spins. Proton NMR imaging maps the distribution of water and fat, and the images largely depict the tissue structure. The resolution in such images is slightly less than one millimeter for slice thicknesses of 2-3 mm.

A primary advantage of the NMR method is the ability to perform these measurements noninvasively on objects which are opaque. Furthermore, the response varies depending upon the properties of the spins and so chemical environment is important. Thus NMR imaging provides a means for studying the internal structure and chemical composition of objects.

4. ORGANIZATION OF THE THESIS

The remainder of the thesis is organized into three parts. In chapter II, the basic theory of NMR taking account of the effect of magnetic field gradients is reviewed. A method based upon the analysis of lineshapes for determining gradient magnitudes and linearity, and methods for imaging and diffusion measurement are described. The modification of a high resolution NMR probe with gradient coils for imaging and diffusion measurement, apparatus for surface coil diffusion measurements and measurements on model systems using both instruments will also be described.

Chapter III deals with the measurement of proton translational motion by NMR. First to demonstrate the range of quantitation and possible applications for chemical shift resolved measurements, the diffusion of glucose and dextran was studied. Secondly, the pulsed gradient method is used to characterize the motion of water and fat *in-vivo* in human forearm (muscle and connective tissue).

Chapter IV describes the application of two-dimensional NMR imaging methods to map proton distribution in two biological systems: pupae of *Barbara colfaxiana* and mature caps of *Acetabularia mediterranea*.

II. MAGNETIC FIELD GRADIENTS IN NMR

In this chapter, the principles and the apparatus for diffusion measurement and imaging by NMR, and experimental results for model systems will be described. The discussion begins with a review of standard NMR theory in section A.1. In section A.2, it is shown that the NMR spectrum, broadened by the application of a gradient, is directly related to the spin distribution provided the natural linewidth is small compared to the overall linewidth. This relationship can then be used to determine gradient magnitude and linearity. In section A.3, NMR methods for obtaining two-dimensional spectra with two spatial coordinates and with one coordinate replaced by chemical shift are then described. The factors which affect the relative intensities or contrast, and the spatial resolution between features in NMR images are also discussed.

In sections A.4 and A.5, the application of magnetic field gradients for studying translational motion due to diffusion and bulk flow of the spins is discussed. The description of the effects of diffusion and flow by the modification of the Bloch equations, follows the discussion of Stejskal *(5)*. In section A.4, the pulsed gradient spin echo pulse sequence of Stejskal and Tanner *(12)* is introduced, wherein gradient pulses are applied equally before and after the 180° pulse. For multi-component systems, since the spin echo signal is measured in the absence of gradients, high resolution spectra can be

obtained and the diffusion coefficients can be determined for each chemical shift.

In section A.5, the effect of randomized flow is obtained by first solving for uniform motion and then averaging over a Gaussian distribution of velocities. It is shown that the spin echo decays with an effective diffusivity that increases with the echo time. Thus it is possible to distinguish between true diffusion and randomized flow both of which may occur in a living biological system.

In the experimental section, the apparatus used for diffusion measurements and microscopic imaging (section B.1) and the apparatus used for surface coil, pulsed gradient spin echo measurements (section B.2) are described. Gradient coils were constructed for both systems, using standard designs suitable for the cylindrical bore of superconducting magnets. The smaller size of these gradient coils compared to those built into the respective superconducting magnets allows the generation of larger gradients with shorter rise times. To maximize the working area for samples, the current windings were only approximately placed. However, the diameters of the coils were large enough so that the variation of the magnetic field over the sample was linear. For microscopic imaging, the gradient coils were wound on a Perspex former which was then mounted on a high resolution NMR probe. For measurements with surface coils, the gradient coils were wound on a PVC former which was then placed in

the bore of the magnet. In section B.3, the NMR methods including data acquisition procedures, apodization and the equalization of the field of view for imaging are described.

In the first part of the results and discussion section, C.1-C.4, the determination of gradient magnitudes from lineshapes will be described. After ensuring that the rf distribution is uniform and that the effects of receiver dead time were minimized, gradient spectra were obtained with lineshapes that agree quite well with the expected lineshape. In particular, with the gradient applied across a capillary containing water, the gradient magnitude was obtained allowing the absolute determination of the diffusion coefficient of water using the static gradient technique.

The determination of the diffusion coefficient of water using the pulsed gradient method is described in section C.5. Measurements were performed with both the modified high resolution apparatus (B.1) and the surface coil apparatus (B.2). Eddy current effects, causing unequal dephasing and rephasing of the spins and resulting in a reduction of the echo amplitude, were observed on both systems. These effects were minimized by varying the experimental parameters including the gradient magnitude, duration of the gradient pulse and the echo time. In section C.6, the measurement of the diffusion coefficient of acrylonitrile from single, double and triple quantum echoes is described. The single quantum measurement was performed using the standard pulsed

gradient method. For the double and triple quantum measurements a modified pulsed gradient spin echo sequence was used to select double and triple quantum echoes.

In section C.7, the two dimensional imaging of the proton distribution in capillaries containing water and acetone will be described.

A. THEORY OF NUCLEAR MAGNETIC RESONANCE

In this review, the rotating frame is introduced for describing the effect of radiofrequency magnetic fields on the spin system *(46,47)*. The Bloch equations are adopted to give a description of the combined effects of external fields and relaxation of the spin system. For liquids, the Bloch equations predict that the frequency spectrum of the response, after the application of a 90° pulse, consists of a series of Lorentzian lines corresponding to spins with different chemical shifts.

1. GENERAL

Many atomic nuclei have a non-zero spin angular momentum, $I\hbar$, and a dipolar magnetic moment, $\underline{\mu} = \gamma\hbar\underline{I}$, collinear with it. The constant of proportionality, γ, is called the gyromagnetic ratio. In a static magnetic field, B_0, different orientations of the nuclear spin or more briefly, spin, with respect to the field are described by different values of the quantum number, $I_z = m$, of the spin quantized along the field and correspond to different

magnetic energies, E_m.

The interaction energies are given by the hamiltonian

$$\mathcal{H}_o = -\underset{\sim}{\mu}\cdot\underset{\sim}{B}$$

$$= -\gamma\hbar B_o I_z. \qquad [2.1]$$

The latter expression holds if the field is chosen to lie along the z-direction, $\mathbf{B} = B_o\hat{z}$.

At equilibrium, a preferential alignment of the nuclear spins along the direction of the field gives rise to a net magnetization, M_{eq}, and is described by a Maxwell-Boltzmann distribution of populations of the energy levels

$$M_{eq} = \frac{N\gamma\hbar \sum_{m=-I}^{I} me^{\gamma\hbar mB_o/kT}}{\sum_{m=-I}^{I} e^{\gamma\hbar mB_o/kT}}. \qquad [2.2]$$

Nuclear magnetic resonance is a technique for measuring the magnetism by the application of an oscillating magnetic field, perpendicular to the static field, in the form of radiofrequency radiation. Resonance is the condition where the angular frequency of the applied radiation must match energy differences between levels in order that energy be absorbed, i.e., $\hbar\omega = \Delta E$.

For a system such as this, a convenient description in terms of a statistical ensemble of quantum mechanical systems (the spins), involves the density operator ρ which is defined so that for any observable Q, the expression for

the expectation value is given by *(48,49)*

$$\langle Q \rangle = \mathrm{Tr}(Q\rho). \qquad [2.3]$$

The density operator ρ must satisfy the three conditions:

(i) $\mathrm{Tr}\rho = 1$

(ii) ρ must be Hermitian

and

(iii) ρ is positive definite.

The physical interpretation of these conditions is that the diagonal elements of ρ constitute the probabilities of finding the system in the corresponding pure state. The sum of the probabilities equals unity, and expectation values of operators corresponding to any physical observable are real. At equilibrium, the density operator takes the form

$$\rho_{eq} = \frac{1}{Z} e^{-\mathcal{H}_0/kT} \qquad [2.4]$$

where

$$Z = \mathrm{Tr}(e^{-\mathcal{H}_0/kT}). \qquad [2.5]$$

The equilibrium magnetization is given by

$$\begin{aligned} M_{eq} &= \gamma\hbar\langle I \rangle_{eq} \\ &= \gamma\hbar\mathrm{Tr}(I\rho_{eq}) \\ &= \gamma\hbar\frac{1}{Z}\mathrm{Tr}(I_z e^{-\mathcal{H}_0/kT}). \end{aligned} \qquad [2.6]$$

In the high temperature approximation, $\mathcal{H}_0/kT \ll 1$, and

expanding the exponential terms gives Curie's law for the magnetization

$$M_{eq} = \frac{\gamma^2 \hbar^2 I(I+1)}{3kT} B_o . \qquad [2.7]$$

The equilibrium magnetization is aligned with the field and is directly proportional to the magnitude of the field.

The time evolution of the system in the Schrödinger picture is given by the von Neumann equation

$$i\frac{d\rho}{dt} = \frac{1}{\hbar}[\mathcal{H}, \rho] \qquad [2.8]$$

which may also be written as

$$i\frac{d\rho}{dt} = \frac{1}{\hbar}\mathcal{L}\rho \qquad [2.9]$$

using the notation $\mathcal{L}$ for $[\mathcal{H}, \ ]$, a superoperator.
For spin 1/2, the density operator can be expressed as *(48)*

$$\rho = \frac{1}{2}(1 + \underset{\sim}{P}\cdot\underset{\sim}{\sigma}) \qquad [2.10]$$

where **P** is the polarization vector and the components of $\underset{\sim}{\sigma}$ are the Pauli spin matrices. The time evolution of the x and y components of the polarization are then given by the expressions

$$\frac{dP_x}{dt} = -\omega_0 P_y$$
$$\frac{dP_y}{dt} = \omega_0 P_x \qquad [2.11]$$

which has the solution

$$P_y = P_{y,0}\cos\omega_0 t$$
$$P_x = P_{y,0}\sin\omega_0 t \qquad [2.12]$$

for the initial value, $P_{y,0}$ of P_y. The motion given by equation [2.12] can be represented in a precession diagram[1] as follows

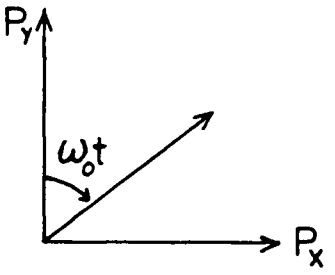

This result is directly analogous to that of the classical description where a magnetic moment **M** experiences in a field **B**, a torque **M** x **B** equal to the rate of change $\hbar \frac{d\underset{\sim}{I}}{dt}$ of its angular momentum. Since $\mathbf{M} = \gamma\hbar\mathbf{I}$ the motion of the magnetic moment is described by the equation

$$\frac{d\underset{\sim}{M}}{dt} = \gamma \underset{\sim}{M} \times \underset{\sim}{B}. \qquad [2.13]$$

---

[1]M. BLOOM, Lectures, UBC, 1981.

If now an oscillating field with frequency ω_2 is applied,

$$\underset{\sim}{B}_1 = 2B_1 \cos\omega_2 t \ \hat{x} \qquad [2.14]$$

to describe the motion it is useful to transform to a coordinate system rotating around the z-direction at frequency $-\omega$. The oscillating field may be written as the sum of two counter rotating components and the hamiltonian becomes[2]

$$\mathcal{H}_R = e^{-i\omega \underset{\sim}{J}_z t}(\mathcal{H}_0 + \mathcal{H}_1) \qquad [2.15]$$

$$= -\hbar\omega_0 I_z - \frac{\hbar}{2}\omega_1\left\{[e^{i(\omega_2-\omega)t} + e^{-i(\omega_2+\omega)t}]I_+ + [e^{i(\omega_2+\omega)t} + e^{-i(\omega_2-\omega)t}]I_-\right\}$$

where $\omega_1 = \gamma B_1$. If $\omega_2 = \omega$ then

$$\mathcal{H}_R = -\hbar\omega_0 I_z - \frac{1}{2}\hbar\omega_1(I_+ + I_-) + \frac{1}{2}\hbar\omega_1(e^{-2i\omega t}I_+ + e^{2i\omega t}I_-). \qquad [2.16]$$

In the rotating frame approximation, the effect of the rapidly oscillating terms is small giving

$$\mathcal{H}_R \cong -\hbar\omega_0 I_z - \hbar\omega_1 I_x. \qquad [2.17]$$

---

[2] Note: $\underset{\sim}{J}$ is the rotation generator for operators.

Now, applying the same transformation to the density operator

$$\rho_R(t) = e^{-i\omega \mathcal{I}_z t} \rho(t) \qquad [2.18]$$

the time derivative is

$$i\frac{d\rho_R(t)}{dt} = \omega \mathcal{I}_z \rho_R + e^{-i\omega \mathcal{I}_z t} i\frac{d\rho}{dt}$$

$$= \frac{1}{\hbar}(\mathcal{L}_0 + \mathcal{L}_{1R} + \hbar\omega \mathcal{I}_z)\rho_R(t)$$

$$= [-(\omega_0 - \omega)\mathcal{I}_z - \omega_1 \mathcal{I}_x]\rho_R(t)$$

$$= -\omega_{eff} \mathcal{I}_{eff} \rho_R(t), \qquad [2.19]$$

The effective field in the rotating frame is in the direction of $\underset{\sim}{\mathcal{I}}_{eff}$ and causes a precession with frequency

$$\omega_{eff} = [(\omega_0 - \omega)^2 + \omega_1^2]^{1/2}. \qquad [2.20]$$

At resonance, $\omega_0 = \omega$ and

$$\omega_{eff} \mathcal{I}_{eff} = \omega_1 \mathcal{I}_x. \qquad [2.21]$$

Then the application of the B_1 field for a time t' causes polarization along the z-axis to rotate through an angle α

$= \omega_1 t'$ around the x-axis:

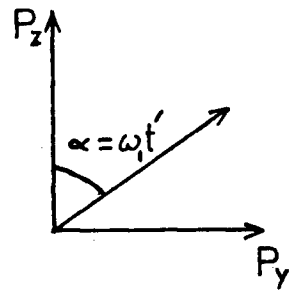

and is said to constitute an α_x° pulse; the subscript indicates the direction of the applied B_1 field. In the absence of radiofrequency radiation, the precession around the z-direction occurs at a frequency $\omega' = \omega_0 - \omega$ in the rotating frame.

In a sample, there is likely to be a distribution of Larmor frequencies and the resonance condition will not be exactly fulfilled for all of the spins simultaneously. However, in pulsed NMR sufficiently intense rf radiation is applied that the relationship in Eq. [2.21] is approximately true, i.e. $\omega_1 >> (\omega_0 - \omega)$ for all ω_0 in the sample.

Thus in a typical experiment, a 90° pulse rotates magnetization which is initially along z at equilibrium to the y-axis. The action of the static field causes the transverse components of magnetization to precess around the z-direction, inducing a voltage in a coil which is measured. Fourier transformation of this time domain signal yields the

frequency spectrum of the response *(50)*

$$S(\omega) = \int_{-\infty}^{\infty} f(t) e^{i\omega t} dt. \qquad [2.22]$$

With a phase sensitive detector, information about projections of the rotating magnetization along any axis in the xy plane can be obtained *(51)*.

Until now only the action of external fields on the system has been discussed. There are several mechanisms by which the system may return to equilibrium but all require a randomly fluctuating field to be experienced by the spins. Various properties of nuclear magnetism therefore undergo substantial changes when liquid (or gaseous) samples are used. These changes are brought about by the existence of rapid molecular motions of large amplitude and random character, inside these samples, which generate the fluctuating fields for relaxation. These motions include rotational tumbling of individual molecules, relative translational motion of molecules and even, because of chemical exchange, migrations of atoms or groups of atoms from one molecule to another.

Mechanisms for relaxation include dipole-dipole coupling, quadrupole relaxation, chemical shift anisotropy, spin-rotation and scalar coupling *(46,47)*. The calculations required for a quantum mechanical description of spin relaxation processes are not needed and too bulky to be given here.

From phenomenological arguments, Bloch proposed a set of simple equations that provide in most cases a correct quantitative description, sufficient for the purpose here, of the magnetic properties of ensembles of nuclei in external magnetic fields *(52)*. These consist of the following

$$\frac{d\underset{\sim}{M}}{dt} = \gamma \underset{\sim}{M} \times \underset{\sim}{B} - \frac{M_x \hat{i} + M_y \hat{j}}{T_2} - \frac{M_z - M_0}{T_1}\hat{k} \qquad [2.23]$$

where i',j',k' are the unit vectors of the rotating frame, T_1 and T_2 are the longitudinal and transverse relaxation times respectively. Longitudinal relaxation involves the return of the magnetization towards thermal equilibrium with loss of energy to the lattice. The latter consists of the translational and rotational degrees of freedom. Transverse relaxation involves the dephasing of components of the magnetization due to various local fields arising from interactions between spins and with the surroundings.

The rate of decay is dependent upon details of the motion of the molecules containing the spins and these are often described in terms of correlation functions *(53)*. For example, the correlation function, $G(\tau)$, for a fluctuating local field, $\mathbf{b}(t)$, could be expressed as

$$G(\tau) = \langle \underset{\sim}{b}_l(t) \cdot \underset{\sim}{b}_l(t+\tau) \rangle$$
$$= \langle b_l^2 \rangle \, e^{-|\tau/\tau_c|} \qquad [2.24]$$

where the angular brackets imply an ensemble average and the second equality is an often made assumption as to the form of G(t). The correlation time τ_c characterizes the time scale of the fluctuations.

Nuclear relaxation rates are related to the time correlation functions of the fluctuating local interations by Fourier transformation. This gives rise to the so-called spectral density or power spectrum, $J(\omega)$, of the fluctuations. For the $G(\tau)$ given above this has the form

$$J(\omega) = \langle b_l^2 \rangle \frac{2\tau_c}{(1+\omega^2\tau_c^2)} \quad [2.25]$$

For magnetic dipole-dipole interactions between like spins the general forms of the relaxation rates are

$$(T_1)_d^{-1} = 2/3\ \overline{\Omega_d^2}\left[j(\omega_o) + 4j(2\omega_o)\right]$$

and [2.26]

$$(T_2)_d^{-1} = 2/3\ \overline{\Omega_d^2}\left[3/2\, j(0) + 5/2\, j(\omega_o) + j(2\omega_o)\right]$$

where $j(\omega)$ is a 'reduced' spectral density which for the form given in equation [2.25] would be $J(\omega)/2\langle b_l^2\rangle$, and $\Omega_d^2 = \gamma^2\langle b_l^2\rangle$ is a measure of the appropriate mean-squared dipolar coupling strength. The frequencies 0, ω_o and $2\omega_o$ result from a quantum mechanical description of the spins and indicate that energy can only be exchanged in discrete quanta.

Neglecting the effect of **B**, the Bloch equations give

$$M_z = M_o(1-e^{-t/T_1})$$
$$M_{xy} = M_{xy,o}\, e^{-t/T_2}\,. \qquad [2.27]$$

The signal obtained after the application of a 90° pulse is referred to as a free induction decay (FID), and takes the form of a damped oscillating function of time

$$M_y = M_{y,o}\, e^{-t/T_2} \cos \omega_o t\,. \qquad [2.28]$$

The frequency spectrum, obtained after Fourier transformation, is the sum of real (absorption) and imaginary (dispersion) components

$$S(\omega) = \frac{M_o}{2}\left(\frac{T_2}{1+(\omega-\omega_o)^2 T_2^2} + \frac{i(\omega_o-\omega)T_2^2}{1+(\omega-\omega_o)^2 T_2^2}\right) \qquad [2.29]$$

The counter rotating components were neglected and the real component has the form of a Lorentzian function with a linewidth at half maximum of $2/T_2$. In liquids, the rapid tumbling of molecules with reorientational correlation times of 10^{-12} to 10^{-11} s leads to motional averaging of the dipole-dipole and quadrupole interactions, and chemical shift anisotropies *(46, 47)*. The spectra that are obtained

consist of narrow lines. The linewidths are typically of the order of a hertz and are determined largely by magnetic field inhomogeneity.

Further structure in these spectra arises from the magnetic shielding of the nuclei by electrons and the indirect coupling of one nucleus with another via the electrons. The motion of the orbital electrons produces a field at the nucleus which is proportional and in opposition to the applied field, B_0. The local magnetic field at the nucleus will be given by

$$B_{local} = B_0 (1 - \sigma) \qquad [2.30]$$

where σ is the chemical shift.

The indirect coupling *via* the electrons causes one nuclear spin to experience a field which varies depending upon the orientation of the other. This interaction causes characteristic splittings of the lines in high resolution spectra and is described by the expression *(54)*

$$\mathcal{H}_J = J \underset{\sim}{I}^{(A)} \cdot \underset{\sim}{I}^{(B)}. \qquad [2.31]$$

The constant J is usually of the order of several hertz for protons. While these effects will be observed in some spectra, they are not of concern here and will not be discussed any further.

2. LINESHAPE: RELATION TO GRADIENT AND SAMPLE SHAPE

While the effect of inhomogeneity of magnetic fields has often been discussed, particularly in terms of a shortened transverse relaxation time, T_2^* *(55)*, no explicit evaluation of the effect of linear gradients on lineshapes, in the frequency domain has appeared. In this section, the NMR lineshape for a cylindrical object measured in the presence of a magnetic field gradient will be discussed. Following the analysis of Kumar *et al.(41)*, the frequency spectrum is shown to be the convolution of the spin distribution function with a Lorentzian lineshape function for liquids. When the natural linewidth is small compared to the overall linewidth with the gradient applied, the Lorentzian lineshape can be approximated by a delta function and the frequency spectrum is then given by the spin distribution function directly. The relation is also only valid when the variation of the magnetic field gradient is small. Otherwise, spins at different parts of the sample may resonate at the same frequency and the correspondence between frequency and position would not be unique. The magnitude of the gradient can be determined from the linewidth or, for a cylindrical sample, by inverting the relationship between lineshape and spin distribution function.

The NMR signal in the frequency domain, $S(\omega)$, is a composite of the contributions from the various volume

elements of the sample and can be expressed in the form

$$S(\omega) = \iiint c(\underset{\sim}{r})\, S(\underset{\sim}{r}, \omega)\, dv \qquad [2.32]$$

where c(r) is the three-dimensional nuclear spin distribution function and S(r,ω) is the NMR signal from a volume element. For a single gradient applied along the x axis S(ω) is given by

$$S(\omega) = \int c(x)\, S(x, \omega)\, dx \qquad [2.33]$$

where c(x) represents the projection of the nuclear spin density onto the x axis. The NMR signal, S(ω), after a change of coordinates and neglect of the counter-rotating component, is the sum of absorption, A(ω), and dispersion, D(ω), components

$$S(\omega) = \frac{1}{2}\left(A(\omega) + iD(\omega)\right). \qquad [2.34]$$

In liquids, the absorption signal is Lorentzian and the contribution due to spins at position x', in a linear magnetic field gradient, G_x, is given by

$$A(x, \omega) = \frac{M_o / T_2}{(1/T_2)^2 + (\omega_{x'} - \omega)^2}$$

$$= \frac{M_o / T_2}{(1/T_2)^2 + (G_x x' - \omega)^2} \qquad [2.35]$$

where M_0 is the equilibrium magnetization and T_2 is the

spin-spin relaxation time. For convenience the Larmor frequency was chosen equal to zero. For an object of length, l, with D_{nh} symmetry, and a linear field gradient along its principal axis, c(x) is constant, and the normalized absorption signal can be obtained exactly

$$A_{D_{nh}}(\omega) = \frac{1}{\pi l}\left(\tan^{-1} G_x T_2 (l/2 - \omega/G_x) - \tan^{-1} G_x T_2 (-l/2 - \omega/G_x)\right) \qquad [2.36]$$

with a linewidth at half-height

$$W_{1/2, D_{nh}} = \left(4/T_2^2 + \gamma^2 G^2 l^2\right)^{1/2} \qquad [2.37]$$

For NMR imaging, the natural linewidth imposes a limit on the spatial resolution attainable with a particular gradient. If we let l be the smallest resolvable element, then the magnitude of the gradient which is required is given by the expression

$$G > \frac{2}{\gamma l T_2} \qquad [2.38]$$

A similar expression that also incorporates the effect of inhomogeneity of the magnetic field has been given by Bottomley *(56)*. A common situation, for which the analytical solution of Eq. [2.33] has not been obtained, is that of a cylinder with the gradient applied perpendicular to its principal axis.

To extend the analysis and to incorporate the effects of gradient nonlinearity, we simplify the integration in Eq. [2.33] by considering systems for which the contribution of spin-spin relaxation to the linewidth (as in Eq. [2.38]) is small compared to that of the gradient; i.e., $\gamma G_x l >> 2/T_2$. For a sample contained in a 5 mm NMR tube in a weak gradient of 1 mTm^{-1}, T_2 should be greater than 15 ms. Now the contribution to the signal from spins at position x', $A(x',\omega)$, can be replaced by a delta function:

$$\begin{aligned} A(\omega) &= \int c(x')\, A(x',\omega)\, dx' \\ &\simeq \int c(x')\, \delta(G_x x' - \omega)\, dx'. \end{aligned} \qquad [2.39]$$

In a linear field gradient, with ω directly proportional to x

$$\begin{aligned} A(\omega) &= A(G_x x) \\ &= \int c(x')\, \delta(x' - x)\, dx' \\ &= c(x). \end{aligned} \qquad [2.40]$$

The absorption lineshape directly measures the spin distribution.

For a cylindrical object of radius r, with a linear

gradient applied perpendicular to its principal axis, the spin distribution function can be expressed as (Fig. 2.1)

$$c(x) = \frac{2}{\pi r^2}(r^2 - x^2)^{\frac{1}{2}} \qquad -r \leq x \leq r. \qquad [2.41]$$

The corresponding expression for the FID or time domain signal is obtained by taking the Fourier transform of Eq. [2.41] which gives the Bessel function $J_1(G_x rt)$ *(17)*. By analogy with Eq. [2.37], the linewidth at half height is

$$W_{\frac{1}{2}} = \left(\frac{4}{T_2^2} + 3\gamma^2 G_x^2 r^2\right)^{\frac{1}{2}} \qquad [2.42]$$

Before proceeding further it is worthwhile to note that NMR lineshapes are also affected by the inhomogeneity of the distribution of the radiofrequency field used to elicit the nuclear responses. Identical nuclear spins at different positions in the sample do not contribute equally to the observed signal. The resultant spectrum can be represented as

$$A(\omega) = \int f(x')\, c(x')\, \delta(G_x x' - \omega)\, dx' \qquad [2.43]$$

when T_2 effects are neglected and where $f(x')$ is a reduced radiofrequency field distribution function. In the following discussion $f(x')$ is assumed to be constant across the sample and is omitted.

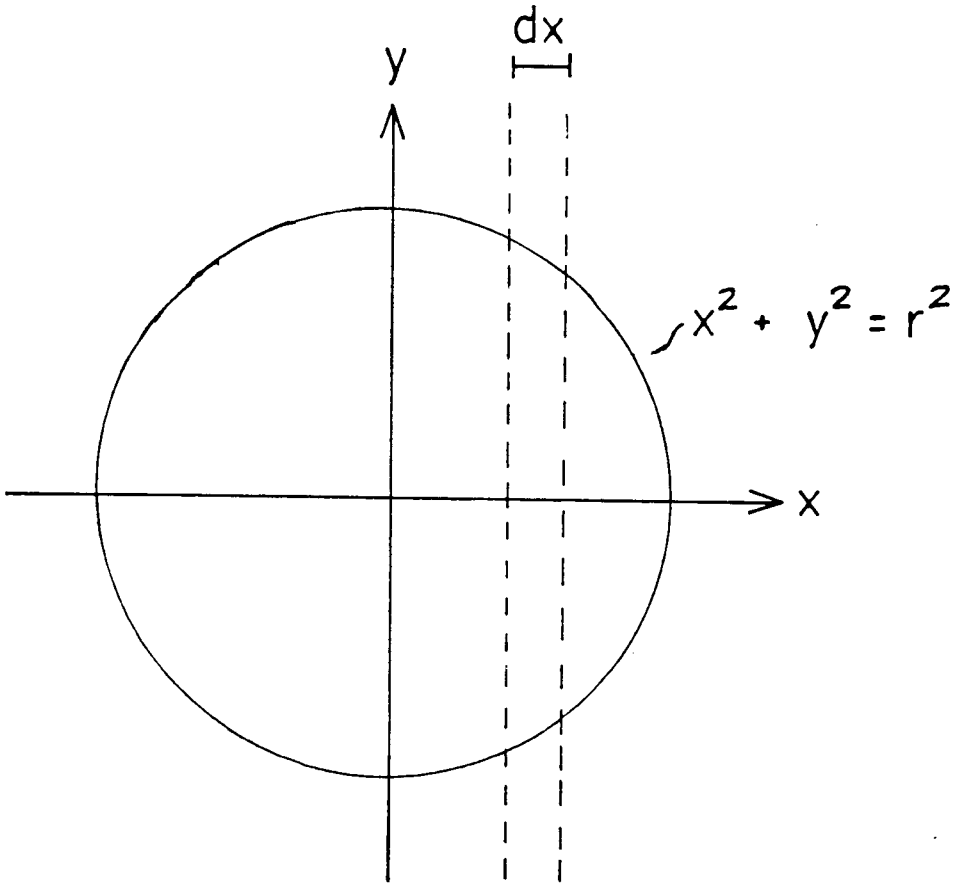

Fig. 2.1 The number of spins in a thin slice, dx, through a cylinder is proportional to $y = 2(r^2 - x^2)^{1/2}/\pi r^2$ where r is the radius.

To describe the effect of chemical shift it is useful to introduce a frequency offset, ω_f. Equation [2.39] then becomes

$$A(\omega+\omega_f) = \int C(x')\ \delta(\omega_o+G_x x'-(\omega+\omega_f))\,dx'. \qquad [2.44]$$

When the frequency offset, ω_f, is equal to the Larmor frequency, ω_o, we obtain

$$A(\omega+\omega_o) = C(x). \qquad [2.45]$$

The spectrum still measures the spin distribution but the position of the line is shifted depending upon the Larmor frequency and chemical shift. In a sample with spins having different Larmor frequencies, the result would be a set of overlapping lines each giving the distribution of a particular set of spins.

In general, the frequency, ω, of spins at position x is given by

$$\begin{aligned}\omega &= \omega_o + G_x x \\ &= \omega_o + G_x(0)x + \frac{\partial G_x(0)}{\partial x}x^2 + \frac{1}{2!}\frac{\partial^2 G_x(0)}{\partial x^2}x^3 + \ldots\end{aligned} \qquad [2.46]$$

where the magnetic field gradient is expressed as a Taylor series. In a nonlinear gradient, caused by the higher order terms in Eq. [2.46], identical spins at different positions in the object may resonate at the same frequency. The net

absorption signal can then be represented as

$$A_{net}(\omega) = \sum_{i=1}^{n} c(x_i) \qquad x_i < x_{i+1} \qquad [2.47]$$

such that $\omega = G_x x_i$. However in NMR, nonlinearities over the sample are usually sufficiently small so that $c(x_i) = 0$ for $i > 1$. In this situation the appearance of the spectrum from a square-profile object will not reflect the nonlinearities.

Thus we have shown that when the effects of spin-spin relaxation are negligible and the nonlinearity of the gradient is small, the NMR signal is given by the mapping of the spin distribution function from the x domain into the frequency domain. In the absence of the effect of inhomogeneity of the applied radiofrequency field, the spectrum should reflect the one-dimensional projection of the spin distribution. For a NMR tube the lineshape would then be given by Eq. [2.41] and measurement of intensity allows the calculation of the spatial coordinates corresponding to the displacement of the spins along the direction of the gradient. A graph of Larmor frequency as a function of displacement can then be prepared and the variation of the gradient across the sample can be determined from the slope. This procedure cannot be applied to situations where the reduced spin distribution function is independent of x because then the relation in Eq. [2.40] cannot be inverted. In NMR imaging experiments where gradients are applied along three axes of a spherical

object, analysis of the spectra will yield frequency as a function of x, y and z coordinates and allow the determination of the displacement of the object and the magnetic field gradient distribution for the three coils.

3. TWO-DIMENSIONAL NMR IMAGING

By varying the excitation, further properties of the magnetism can be studied. In the following, a pulse sequence used in this work for imaging will be described. The factors which determine the relative intensities or the contrast between features in the image and spatial resolution in NMR imaging will be briefly discussed in the next two sections.

So called two-dimensional NMR spectroscopy requires measurements as a function of two independent time intervals to give an array of signals, $S(t_1,t_2)$ *(10)*. Following convention, the pulse sequence for such experiments is divided into periods for preparation, evolution and detection (Fig. 2.2). During the detection period, the time evolution is governed by the hamiltonian $\mathcal{H}^{(2)}$ and Fourier transformation of the signal will give the corresponding frequency spectrum, $S(t_1,\omega_2)$. The evolution under the influence of $\mathcal{H}^{(1)}$ during t_1, will cause the phase, amplitude or both, of the acquired signal to be modulated and Fourier transformation will again yield the associated spectrum, $S(\omega_1,\omega_2)$.

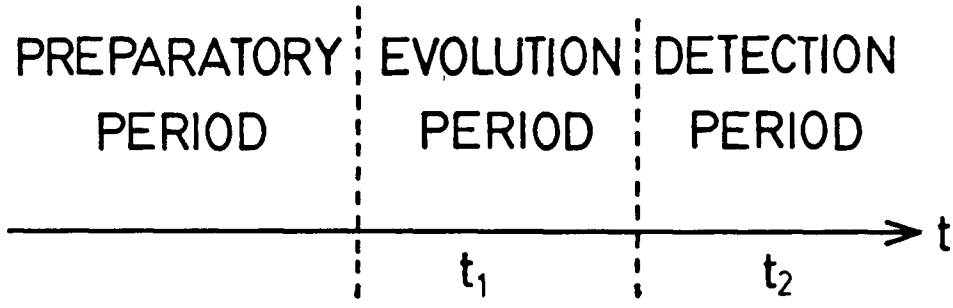

Fig. 2.2 The general scheme for a two dimensional experiment wherein the time axis is partitioned into two independent time intervals t_1 and t_2. The time evolution is governed by the hamiltonians $\mathcal{H}^{(1)}$ and $\mathcal{H}^{(2)}$ during the evolution and detection periods respectively.

The pulse sequence using magnetic field gradients that was used in this work for two dimensional imaging is shown in Fig 2.3. Starting from equilibrium with the magnetization aligned along the z-axis, a 90°_x pulse rotates the magnetization to the y-direction. Subsequently the magnetization will precess around the z-direction giving rise to an observable signal (see p. 21). In the presence of an inhomogeneous field, such as that caused by the application of the y-gradient, the spins will precess with different Larmor frequencies

$$\omega_i = \gamma(B_o + G_y y_i). \qquad [2.48]$$

For a y-gradient pulse applied for a duration d and followed by a delay T, the phase prior to the 180°_y pulse will be

$$\phi_i = \omega_o T + \omega_y d. \qquad [2.49]$$

As shown in Fig 2.4, the rotation of the spins around the y-direction by 180° causes the phase to decrease by $-2(\omega_o T + \omega_i d)$. The subsequent precession causes the phase ϕ_i to increase. At first with a frequency of ω_o until time $T + \tau$, then at frequency ω_i when the y-gradient is applied. All of the spins are re-aligned along the y-direction at $2\tau = 2T + 2d$. The refocussing of the spins produces another observable signal referred to as a spin echo *(16)* and the time, 2τ, is called the echo time. The spin echo is measured

Fig. 2.3 Timing diagram for a two dimensional imaging experiment. Starting at equilibrium the application of 90°_x and 180°_y rf pulses induce the formation of a spin echo at 2τ. A y-gradient pulse of fixed magnitude is applied immediately following the 90°_x pulse for a duration d. After a time delay T such that τ = d + T and a further delay T, the y-gradient is switched on again at τ + T for the duration of the detection period, t_2. The x-gradient is switched on for a time t_1 immediately after the 180°_y such that $t_1 < T$. The grill work indicates that the experiment is repeated as the magnitude G_x is varied, usually in 128 equal increments from a negative value.

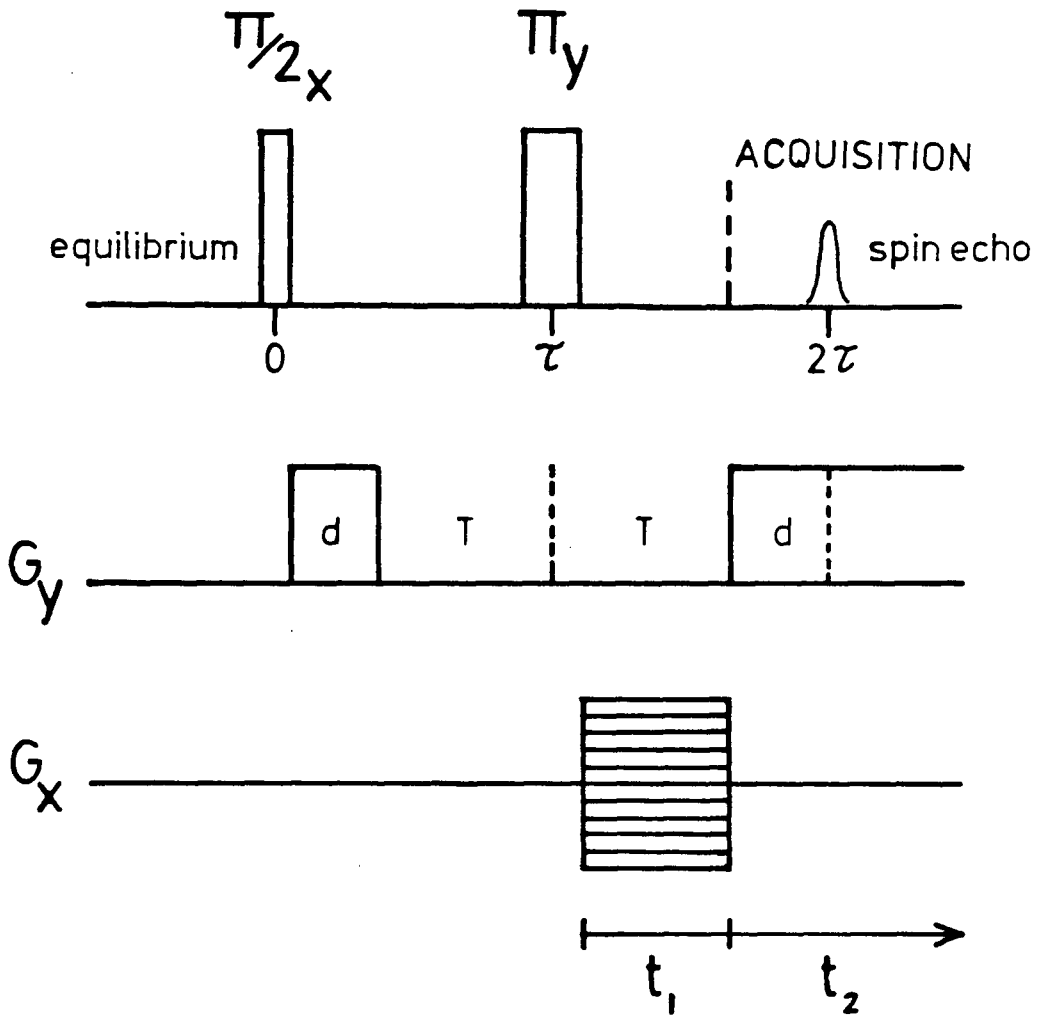
π/2x
πy
ACQUISITION
equilibrium
spin echo
0
τ
2τ
d
T
T
d
Gy
Gx
t1
t2

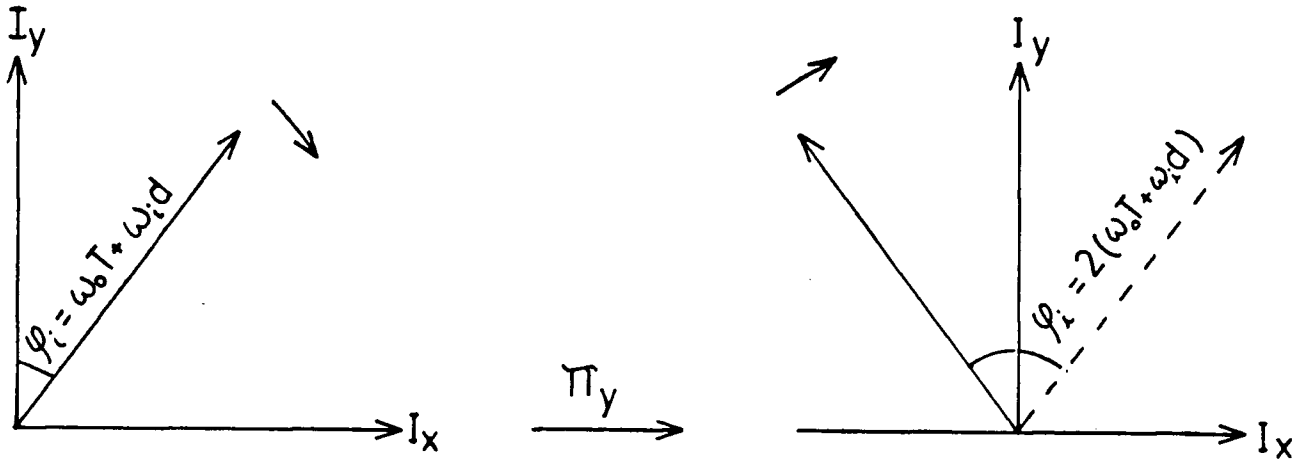

Fig. 2.4 Precession diagram showing the effect of the 180°_y pulse for the pulse sequence in Fig. 2.3. The arrows indicate the direction of precession. As indicated the motion following the 180°_y brings the magnetization back to the y-direction at time 2τ.

as a function of the observation time t_2, forming one dimension of the experiment. The second dimension is obtained by applying a x-gradient pulse for a duration t_1, in the interval T, following the 180°_y pulse. The spin echo acquisition procedure is repeated for various values of the gradient G_x. The application of G_x causes the Larmor frequency of the spins to vary along the x-direction. The phase that is gained by the spins during t_1 from G_x causes the refocussing of the spins at time 2τ to be incomplete, hence G_x is referred to as the phase encoding pulse. The amplitude of the echo quickly decreases as G_x becomes larger.

The resulting array of data constitutes a two-dimensional measurement of the time response $S(G_x,t_2)$ with

$$\mathcal{H}^{(1)} = -\gamma (B_0+G_x x) I_z \quad \text{and} \quad \mathcal{H}^{(2)} = -\gamma (B_0 + G_y y) I_z . \qquad [2.50]$$

If now the vector **k** of reciprocal space is defined such that $k_1 = \gamma G_x t_1$ and $k_2 = \gamma G_y t_2$ then the Fourier transformation with respect to **k** gives the spatial distribution of the NMR signal *(57)*

$$S(\underset{\sim}{r}) = \int_{-\infty}^{\infty} S(\underset{\sim}{k})\, e^{i \underset{\sim}{k}\cdot\underset{\sim}{r}}\, d\underset{\sim}{k} . \qquad [2.51]$$

A third component for **k** would be required for the three dimensional version of the experiment. In general, the

signal S(r) is a convolution of the spin distribution function c(r) with a lineshape function *(41)* which is Lorentzian for liquids.

A variation of the procedure in which the spins are allowed to evolve freely during the detection in the absence of a gradient allows the measurement of chemical shift resolved spectra (Fig. 2.5). A z-gradient pulse is applied during the evolution period and the signal is measured for various values of G_z. The resulting data set may be represented as $S(k_z,t_2)$ with $k_z = \gamma G_z t$ and the corresponding Fourier transformations gives a two-dimensional spectrum $S(z,\omega)$ with z-coordinate on one axis and Larmor frequency along the other. The two dimensional spectrum shows the intensity of the NMR signal as a function of one spatial coordinate, for each chemical shift and will be referred to as a proton distribution map.

4. IMAGE CONTRAST

An image is obtained by displaying, usually in two spatial dimensions, the distribution of the intensity of the NMR response from the sample. Variations in the intensity due to differences in the density and relaxation of the spins, give rise to patterns which generally reflect the internal structure of the sample. By varying the experimental parameters such as the echo time it is possible to change the relative intensities or contrast between different features in the image. For the pulse sequences

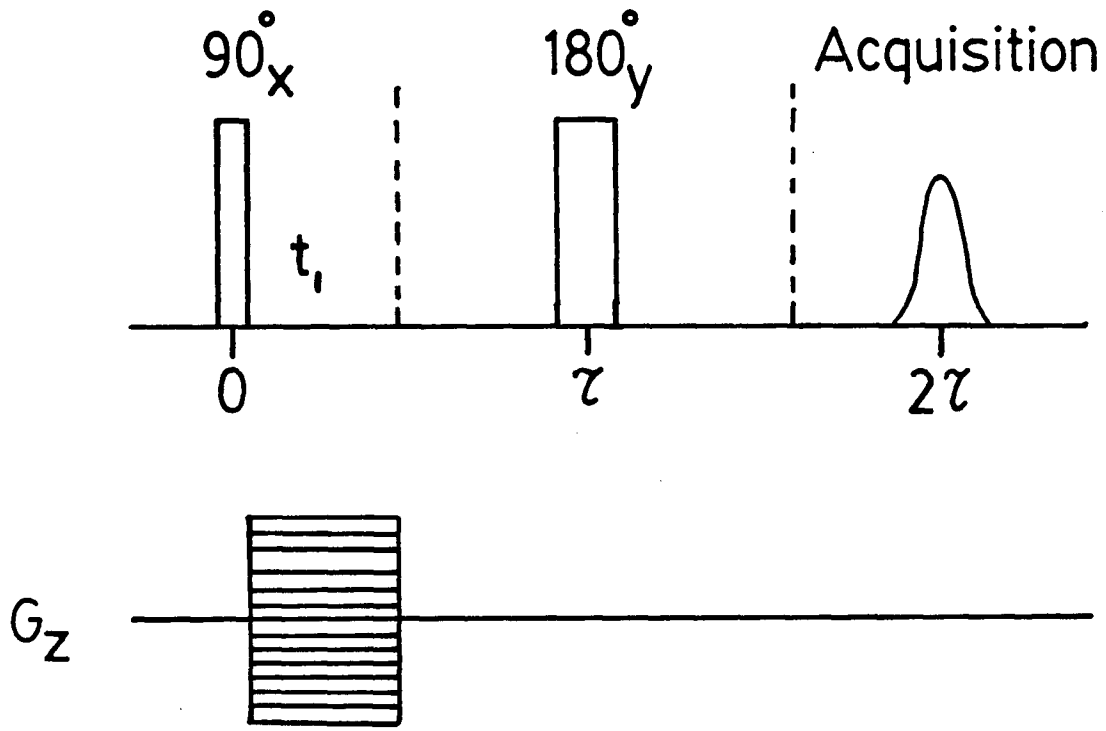

Fig. 2.5 Pulse sequence for the chemical shift resolved mapping of the spin distribution along the z-direction. The echo is acquired in the absence of gradients and a z-gradient pulse is applied during the evolution period, t_1.

shown in Figs. 2.3 and 2.5, the relative intensity for two sets of spins with spin-spin relaxation times, $T_{2,a}$ and $T_{2,b}$, is given by

$$\frac{A_a}{A_b} = \left(\frac{A_a}{A_b}\right)_o e^{-(1/T_{2a} - 1/T_{2b})\,2\tau} \qquad [2.52]$$

where $(A_a/A_b)_o$ is the initial relative intensity. If $T_{2,a}$ is larger than $T_{2,b}$, the relative intensity A_a/A_b can be increased by making the echo time longer.

It is also possible to contrast features according to differences in spin-lattice relaxation times. This can be achieved by applying an inversion-recovery sequence which consists of a 180°-pulse followed by a delay in which the spins are allowed to evolve freely, to a system at equilibrium (Fig. 2.6). The 180° pulse rotates the equilibrium magnetization to the -Z direction and during the subsequent delay, the magnetization returns to equilibrium according to the expression

$$M_z(t) = M_{eq}\,(1 - 2e^{-t/T_1}) \qquad [2.53]$$

where M_{eq} is the equilibrium value.

Following the inversion-recovery sequence, a 90°-pulse may be applied for the spectroscopic determination of spin-lattice relaxation times or an imaging pulse sequence such as that in Fig. 2.3 may be applied to give a T_1 contrasted image. The relative intensities of signals from

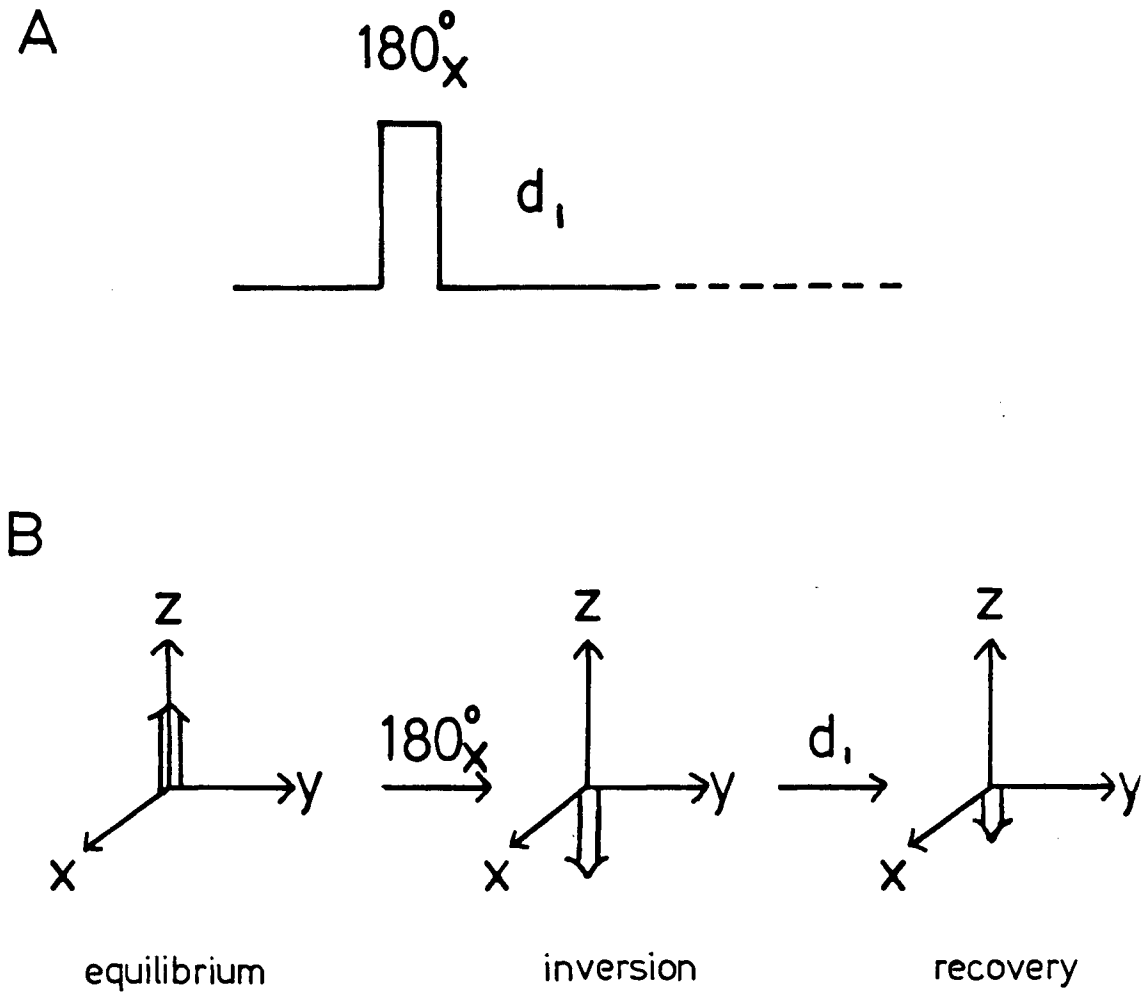

Fig. 2.6 (A) Inversion-recovery pulse sequence. Following the delay, d_1, a 90°-pulse may be applied for the spectroscopic determination of T_1 or an imaging pulse sequence such as that in Fig. 2.3 may be applied to give a T_1 contrasted image. (B) The effect of an inversion-recovery sequence on a spin system, initially at equilibrium.

spins with spin-lattice relaxation times $T_{1,a}$ and $T_{1,b}$, will be given by the expression

$$\frac{M_{z,a}}{M_{z,b}} = \frac{M_{eq,a}}{M_{eq,b}} \frac{(1-2e^{-t/T_{1,a}})}{(1-2e^{-t/T_{1,b}})}. \qquad [2.54]$$

The contrast will be highest when the signal from one of the components is completely removed by satisfying the condition

$$t = T_{1,a \text{ or } b} \ln 2. \qquad [2.55]$$

5. SPATIAL RESOLUTION IN NMR IMAGING

As discussed in the two previous sections, NMR methods for the mapping of spin distributions rely upon the application of magnetic field gradients which cause the Larmor frequency of the spins to vary according to their positions. Factors such as magnetic field inhomogeneity, and spin-spin relaxation, which cause the Larmor frequency to vary further, limit the spatial resolution of these methods. Also, translational diffusion (Brownian motion) contributes an uncertainty in the position of the spins and is thought to be the process ultimately limiting the resolution of NMR imaging methods *(1)*.

For an unwanted dispersion of frequencies characterized by the linewidth at half-height, $W_{1/2}$, the limiting spatial resolution, l, can be estimated from the expression

$$l = \frac{W_{\frac{1}{2}}\ (Hz)}{\gamma G/2\pi (Hz/cm)}. \qquad [2.56]$$

The combined effects of magnetic field inhomogenity, spin-spin relaxation and translational diffusion on the limiting resolution can be estimated from the expression *(1)*

$$l = \frac{G_x^* x}{G_x} + \frac{2}{\gamma G_x T_2} + \sqrt{2Dt} \qquad [2.57]$$

where G_x^* indicates the effective x-gradient due to magnetic field inhomogeneity, t is the measurement time, x indicates the position of the spin and the gradient is considered to be applied along the x-direction. The expression suggests that spatial resolution may be improved by increasing the gradient and by using short measurement times. The G_x^* term also implies that for imaging of larger objects the homogeneity of the magnetic field must be higher.

A further source of frequency variation is from chemical shifts. For spins with chemical shifts σ_1 and σ_2, an apparent displacement, Δx, between the spins is observed and is given by

$$\Delta x = \frac{(\sigma_2 - \sigma_1)\, B_o}{G_x}. \qquad [2.58]$$

For a field of 6.3 T, the apparent displacement for water (4.8 PPM) and lipid protons (1.2 PPM) is 2 mm and 0.2 mm for gradients of 10 and 100 mTm^{-1} respectively. Thus, for imaging it is necessary to suppress chemical shift differences between spins by using large gradients.

In high resolution NMR experiments, the distinction between chemical shifts is optimum and the chemical composition can be determined whereas information about the spatial distribution of spins is minimized. In chemical shift resolved imaging experiments it is possible to determine the spatial distribution of the spins at each chemical shift and a composite image would give the structure of the object *(58)*.

Other factors which affect the resolution are the signal to noise ratio, receiver coil dimension, and the experimental repetition rate. Mansfield and Morris *(1)* have derived an expression, under optimum conditions, for the imaging time needed to resolve a volume element, $(\Delta x)^3$, as follows

$$t_{VOL} = \left(\frac{S}{N}\right)^2 a^2 \left(\frac{T_1}{T_2}\right) \frac{2.8 \times 10^{-5}}{f^{7/2}} \left(\frac{1}{\Delta x}\right)^6 \qquad [2.59]$$

where S/N is the desired signal to noise, "a" the coil radius, and f the spectrometer frequency in megahertz. From this expression, for an imaging time of 1000 seconds Eccles and Callaghan *(59)* estimated the attainable resolution for

small-scale or microscopic imaging at 600 MHz to be 12 μm, but suggested that 30 μm would be a more reasonable value. At a frequency of 270 MHz used in this work, the predicted optimal resolution is 19 μm. This estimation does not include line broadening effects from anisotropic magnetic susceptibility or from chemical-shift variation.

6. SPIN ECHO: PULSED FIELD GRADIENT TECHNIQUE FOR DIFFUSION

Consider an ensemble of identical spins in an inhomogeneous magnetic field, in a liquid so that there is rapid tumbling and motional narrowing prevails. A 90° pulse applied along the x-axis rotates the magnetization to the y-axis. Spins at different positions in the sample will precess at different frequencies and will dephase accompanied by the disappearance of the transverse magnetization. The application of a 180° pulse along the y-axis will change the sign of the phase and the subsequent motion will result in a complete rephasing at time 2τ, if one neglects effects of spin-spin relaxation and diffusion. All of the magnetization will be aligned along the y direction giving rise to another signal or spin echo. The effect of Brownian motion of the molecules is to cause the Larmor frequency of the associated spins to vary correspondingly. As a result, the positions of the molecules and the phase of the spins can be predicted only with some uncertainty which will increase with time. So instead of a sharp distribution, a Gaussian distribution of phases is

obtained causing an averaging and the signal is attenuated. The amplitude of the signal will also be lessened by the effects of relaxation.

The effect of diffusion has been discussed in terms of random walk *(17)* or by adding a diffusion term to the Bloch equation *(12,50)*

$$\frac{d\underset{\sim}{M}}{dt} = \gamma \underset{\sim}{M} \times \underset{\sim}{B} - \frac{M_x \hat{i} + M_y \hat{j}}{T_2} - \frac{M_z - M_0}{T_1} \hat{k} + \underset{\sim}{\nabla} \cdot \underset{\approx}{D} \cdot \underset{\sim}{\nabla} \underset{\sim}{M}. \qquad [2.60]$$

For M_x and M_y the following is obtained

$$\begin{aligned} \frac{dM_x}{dt} &= \gamma B_z M_y - \frac{M_x}{T_2} + \underset{\sim}{\nabla} \cdot \underset{\approx}{D} \cdot \underset{\sim}{\nabla} M_x \\ \frac{dM_y}{dt} &= -\gamma B_z M_x - \frac{M_y}{T_2} + \underset{\sim}{\nabla} \cdot \underset{\approx}{D} \cdot \underset{\sim}{\nabla} M_y. \end{aligned} \qquad [2.61]$$

Combining the expressions for M_x and M_y to give an expression for the complex magnetization, $m = M_x + iM_y$, we obtain

$$\frac{dm}{dt} = -i\omega_0 m - \frac{m}{T_2} + \underset{\sim}{\nabla} \cdot \underset{\approx}{D} \cdot \underset{\sim}{\nabla} m - i\gamma \underset{\sim}{G} \cdot \underset{\sim}{r} m. \qquad [2.62]$$

Transforming to the rotating frame and allowing for the transverse relaxation, set

$$m = \psi e^{-(i\omega_0 + 1/T_2)t}. \qquad [2.63]$$

Then taking the derivative with respect to time

$$\frac{dm}{dt} = \left[\frac{d\Psi}{dt} - (i\omega_o + 1/T_2)\Psi\right] e^{-(i\omega_o + 1/T_2)t} \qquad [2.64]$$

and by comparison with Eq. [2.62] obtain

$$\frac{d\Psi}{dt} = \underline{\nabla}\cdot\underline{\underline{D}}\cdot\underline{\nabla}\Psi - \gamma\underline{G}\cdot\underline{r}\Psi. \qquad [2.65]$$

For D and G depending only on time, a formal solution to the expression for ψ and hence for m can be obtained *(12)*

$$m = m_o e^{-t/T_2} e^{-\gamma^2\left[\int_o^t \underline{F}\cdot\underline{\underline{D}}\cdot\underline{F}\,dt' - 4\zeta\underline{f}\cdot\underline{\underline{D}}\cdot\int_\tau^t \underline{F}dt' + 4\zeta\underline{f}\cdot\underline{\underline{D}}\cdot\underline{f}(t-\tau)\right]} \qquad [2.66]$$

with

$$\zeta = 0 \quad \text{for } 0<t<\tau \qquad \underline{F} = \int_o^t \underline{G}\,dt' \text{ and } \underline{f} = \underline{F}(\tau).$$
$$\zeta = 1 \quad \text{for } t>\tau, \qquad [2.67]$$

The quantity m/m_o is independent of spatial coordinates for the principal echo which occurs at $t = 2\tau$. As discussed by Stejskal and Tanner *(12)*, the formation of the echo may occur at any time or not at all depending upon the sample and the applied gradient. Any inequivalence of the time

evolution induced by the gradients before and after the 180° pulse will cause the echo to be shifted or attenuated.

In the pulsed gradient modification of the experiment, Fig. 2.7, gradient pulses of magnitude G, duration δ, and separation Δ, are applied before and after the 180° pulse of a spin echo pulse sequence *(12)*. For isotropic, time independent diffusion, the decay of the echo amplitude is given by

$$m(2\tau) = m_o e^{-\frac{2\tau}{T_2}} e^{-\gamma^2 G^2 D \delta^2 (\Delta - \delta/3)} . \qquad [2.68]$$

Thus a determination of D, the diffusion coefficient, can be obtained by varying G, δ or Δ. When the duration of the gradient pulse, δ, is much less than the time, Δ, the PFG method measures the motion that occurred during Δ *(12)*. This is useful when diffusion is bounded as found in porous media and biological tissue *(24,61)*. Over short times, the molecules will not travel very far and will not encounter barriers to motion. Thus the diffusion will be unrestricted. For longer times, the motion of the molecule will be limited by the boundaries and the effective diffusion coefficient will be reduced. By performing measurements over a range of diffusion intervals, the size of the restrictions can be determined *(24)*.

For the static gradient experiment δ, Δ and τ are

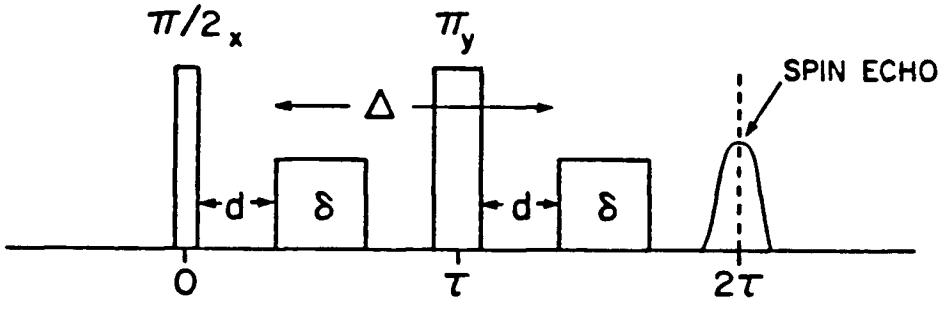

Fig. 2.7 Pulse sequence for the measurement of translational diffusion using pulsed gradients. Gradient pulses of duration δ and separation Δ are applied before and after the 180° pulse of a Hahn echo pulse sequence.

equal, so the decay is given by

$$m(2\tau) = m_o e^{-\frac{2\tau}{T_2}} e^{-\frac{2}{3}\gamma^2 G^2 D \tau^3} . \qquad [2.69]$$

The decay is independent of the amplitudes and lengths of the rf pulses provided these do not vary during the experiment *(62)*. For experiments using a surface coil (see experimental), the decay will then be given by these same expressions despite the rf inhomogeneity.

The spin echo may also be modulated by the effect of scalar spin-spin coupling *(54,63)*. It is thus advantageous to vary the gradient magnitude or the duration of the gradient pulse whilst keeping the echo time 2Δ, fixed. This would make the effects due to J-coupling and spin-spin relaxation constant, simplifying the analysis *(64)*. Compared to static gradient measurements the pulsed gradient technique has the advantage of giving chemical shift resolution. This allows the simultaneous determination of diffusion coefficients for mixtures such as aqueous solutions, micellar solutions and microemulsions.

The factors which affect the accuracy and reproducibility of diffusion measurements have been the subject of several papers *(13,29,65)*. The static field gradient method suffers from the experimental limitation that as the gradient is increased, the NMR linewidth also increases. In order to measure a more rapidly decaying signal, the bandwidth of the detection system will have to

be increased to improve its transient response, a procedure which will admit more noise. With increasing linewidth, the power output of the transmitter will have to be increased to keep the rf field amplitude B_1 greater than the linewidth. The pulsed gradient technique encounters difficulty in the generation of clean gradient pulses requiring stable power supplies and means for elimination and compensation of eddy currents. Callaghan has provided experimental evidence that if the effects of eddy currents, sample movement and pick-up are minimized, acccuracies of 1% can be achieved *(65)*.

For diffusion contrasting in NMR imaging experiments, further gradient pulses are applied in the imaging pulse sequence *(66-68)*. Such a pulse sequence is shown in Fig. 2.8, where the x and y gradients are used for imaging and z-gradient pulses are applied to cause a further attenuation of the signal proportional to the diffusion coefficients of the molecules containing the spins. In comparing the normal and diffusion contrasted images, the change in intensities for a given set of spins is given by Eq. [2.68] and the relative intensities for spins with diffusion coefficients D_a and D_b is

$$\left(\frac{A_a}{A_{a,0}}\right)\Big/\left(\frac{A_b}{A_{b,0}}\right) = e^{-\gamma^2 G^2 \delta^2 (\Delta - \delta/3)(D_1 - D_2)} \qquad [2.70]$$

with $\Delta = 2\tau$. Since the y-gradient is applied in a similar

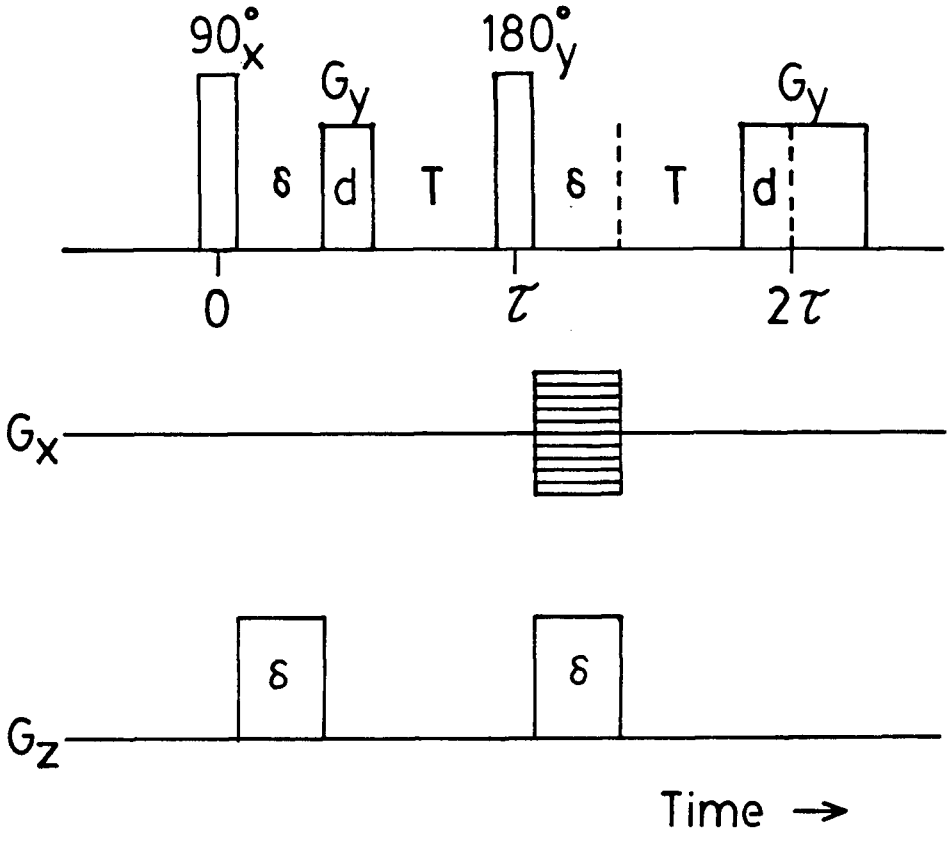

Fig. 2.8 Pulse sequence for diffusion contrasted imaging. The spin echo is acquired in the presence of the y-gradient starting at time 2τ-d. The experiment is repeated for incremental values of phase encoding x-gradient pulses of duration δ. Fixed z-gradient pulses also of duration δ, are applied to cause diffusion contrasting.

fashion, a normal image is already diffusion contrasted.

7. MEASUREMENT OF DIFFUSION BY MULTIPLE QUANTUM SPIN ECHOES

Multiple quantum spectroscopy, by allowing manipulations of the higher order coherences between coupled spins, has been shown to be useful in filtering out resonances in complex overlapping spectra *(69)*. Multiple quantum coherences also show an increased sensitivity to applied gradients *(70-73)* and would allow the measurement of slower diffusional motion than by single quantum coherences. We now describe the measurement of diffusion using pulsed gradients to select multiple quantum spin echoes. The method was used previously for measuring the anisotropic diffusion of oriented molecules in liquid crystals *(21,22)*. While this work was being completed a similar method, using phase cycling of the radiofrequency excitation pulses for the detection of double quantun spin echoes, has been used for measuring the diffusion of fluorinated molecules *(74)*.

In normal pulsed NMR experiments where the free induction decay is measured in the absence of rf radiation, the measured components of the polarization, described by the operators I_x and I_y, correspond only to single quantum coherences, $\Delta M = \pm 1$. Zero quantum and coherences correponding to $\Delta M \geq 2$ are described by combinations of the operators I_x, I_y and I_z *(75,76)* and cannot be directly observed *(77)*. However, two-dimensional NMR methods provide a convenient means for observing multiple quantum

transitions.

The pulse sequence, shown in Fig. 2.9, uses the rf pulse sequence

$$90_x - \tau/2 - 180_x - \tau/2 - 90_x - \tau/2 - 180_x - \tau/2 - 90_x \quad [2.71]$$

to prepare all orders of coherence *(78)*. The coherences are allowed to evolve freely during the period $2\tau < t < t_1 + 2\tau$ and at $t = t_1 + 2\tau$, a 90°_x mixing pulse is applied to transform the unobservable MQ coherences into observable single quantum coherences. Selective detection of magnetization from different orders of coherences is achieved by applying a gradient pulse and delay during the multiple quantum evolution period followed by n identical gradient-delay periods in the mixing period.

The spin echo signal obtained is due only to magnetization which evolved during t_1 as an n quantum coherence *(71,79)*. The pulse sequence is modified for measuring diffusion by further applying gradient pulses equally, before and after a 180° pulse during the time evolution period. The first gradient pulse serves to label the spins with a spatially dependent phase which is proportional to the order of coherence n, and to gradient magnitude. The 180° pulse applied along the y-axis changes the sign of the phase. Then the second gradient pulse causes only partial rephasing because the positions of the spins may have changed during the intervening time. The spin echo

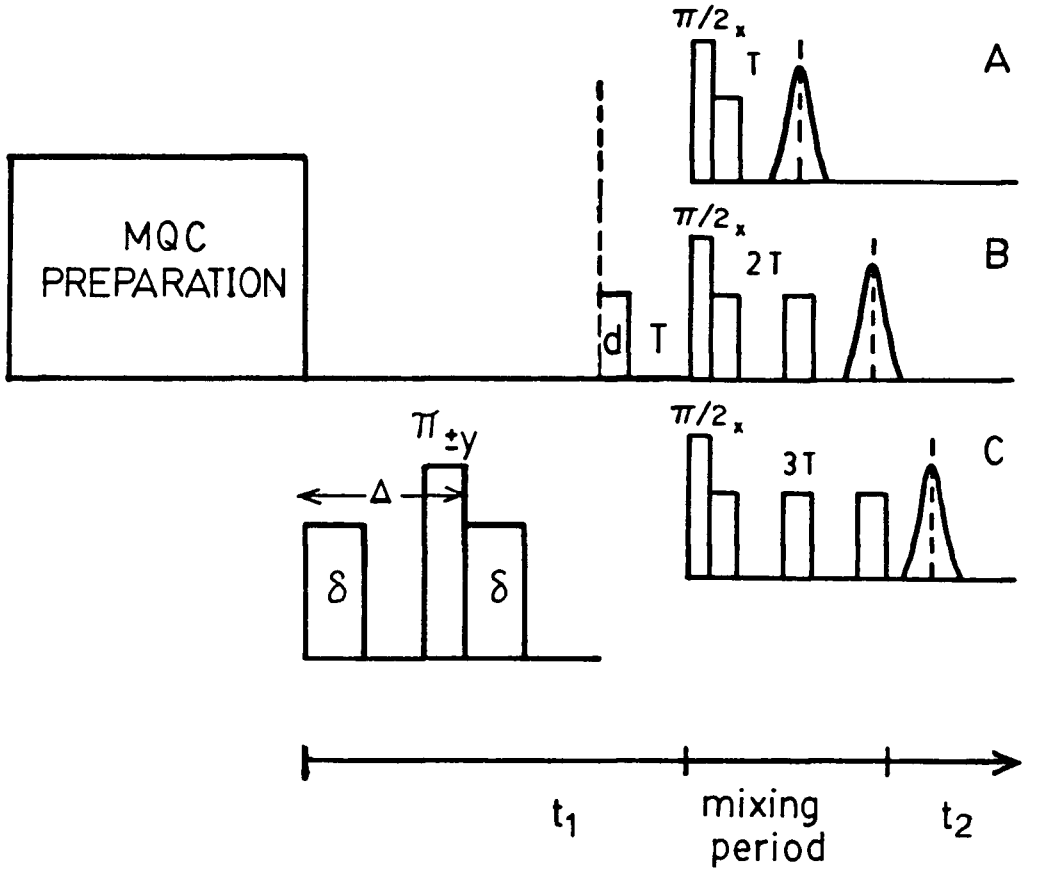

Fig. 2.9 Pulse sequence for the preparation and selective detection of multiple quantum spin echoes. The pulse sequence in Eq. [2.71] is applied during the MQC preparation period to prepare all orders of coherence. After the $(\pi/2)_x$ mixing pulse, gradient pulses are applied to produce single (A), double (B) and triple (C) quantum echoes. A $\pi_{\pm y}$ pulse with gradient pulses of duration δ, before and after, are applied for diffusion measurement.

will decay according to Eq. [2.68] modified for n quantum evolution, by replacing G by nG, to give

$$A(2\tau) = A_0 e^{-2\tau/T_2} e^{-\gamma^2 n^2 G^2 D \delta^2 (\Delta - \delta/3)} . \qquad [2.72]$$

8. SPIN ECHO: THE EFFECT OF RANDOMIZED FLOW

Flow will diminish the spin echo signal by moving spins out of the region of the coil and will, in the presence of the gradient, also cause the Larmor frequency of the spins to vary with their velocities

$$\begin{aligned} \omega(t) &= \omega_0 + \gamma \underset{\sim}{G} \cdot \underset{\sim}{r}(t) \\ &= \omega_0 + \gamma \underset{\sim}{G} \cdot \underset{\sim}{r}(0) + \gamma \underset{\sim}{G} \cdot \int_0^t \underset{\sim}{v}\, dt \\ &= \omega_0' + \gamma \underset{\sim}{G} \cdot \int_0^t \underset{\sim}{v}\, dt \end{aligned} \qquad [2.73]$$

where ω_0' is the initial Larmor frequency, and the velocity v may depend upon position and time. As discussed earlier, the phase that is gained by the spins due to the constant term ω_0' is completely removed at time 2τ in a spin echo experiment consequently, only the displacement of the spins from their initial positions is measured. The variation of the Larmor frequency is described by an additional term in the Bloch equations *(5)*

$$\left(\frac{d\underset{\sim}{M}}{dt}\right)_f = - \underset{\sim}{\nabla} \cdot \underset{\sim}{v}\, \underset{\sim}{M} . \qquad [2.74]$$

The f indicates the contribution due to flow. For a spin echo experiment, the expression for the complex magnetization becomes

$$m(\tau)_f = m(0)\, e^{\{-i\gamma[H(\tau)-2\zeta h]\}} \qquad [2.75]$$

where ζ was defined previously and

$$H(t) = \int_o^t \underset{\sim}{S}\cdot\underset{\sim}{G}\, dt', \quad h = H(\tau)$$
$$S(t) = \int_o^t \underset{\sim}{v}\, dt', \quad s = S(\tau). \qquad [2.76]$$

For a pulsed gradient experiment with steady, uniform flow with velocity v_o, the amplitude of the echo shows oscillatory behaviour

$$m(2\tau)_f = e^{-i\gamma G v_o \tau \delta}. \qquad [2.77]$$

The weighted average for a Gaussian distribution of velocities is

$$\bar{m}(2\tau)_f = \frac{1}{\sqrt{2\pi\langle v^2\rangle}} \int_{-\infty}^{\infty} e^{-\frac{1}{2\langle v^2\rangle}(v-\langle v\rangle)^2}\, e^{-i\gamma G v \tau \delta}\, dv \qquad [2.78]$$

where <v> is the average velocity. If the average velocity is zero, for motion which is random in orientation then the echo will decay according to

$$\bar{m}(2\tau)_f = e^{-\frac{1}{2}\langle v^2\rangle \gamma^2 G^2 \tau^2 \delta^2} \qquad [2.79]$$

with an apparent diffusivity, by comparison of Eqs. [2.69] and [2.79]

$$D_f = 3\langle v^2 \rangle \tau/4. \qquad [2.80]$$

The combined effects of diffusion and random flow, for a single system, would give rise to a net diffusion coefficient of

$$D_{net} = D_o + 3\langle v^2 \rangle \tau/4. \qquad [2.81]$$

The observed apparent diffusion coefficient would increase with the observation time.

A. EXPERIMENTAL

The following is a discussion of the requirements, aspects of gradient coil design and modifications which were implemented, first, for microscopic imaging using the 6.3 T magnet and then for surface coil, pulsed gradient spin echo measurements on the 1.9 T magnet. Specifications of the gradient coils are summarized in Table 2.1.

1. APPARATUS FOR DIFFUSION MEASUREMENT AND MICROSCOPIC IMAGING

Measurements of diffusion and imaging for samples contained in 5 mm NMR tubes including *Barbara colfaxiana* (see chapter IV) and on *Acetabularia mediterranea* (see

chapter IV) were made with a spectrometer based on a 6.3 T, 54 mm bore superconducting magnet made by Oxford Instruments, with a Nicolet 1180 computer and 293B pulse programmer. The lock channel of the spectrometer was not used in these experiments since the gradients interfere with the lock and vice-versa. While the magnet was already supplied with shim coils which produce gradients of 1 mTm^{-1} for the x, y and z directions, it was necessary to construct another system of coils to generate larger gradients which are required for accurate diffusion measurements and higher spatial resolution in imaging.

A gradient coil consists of an arrangement of wires such that the passage of an electric current produces a linearly varying magnetic field over the region of the sample. The criteria for the gradient coils were that gradients of about 100 mTm^{-1} be achieved to allow imaging of objects which might range in size up to approximately 1 cm in length. Nonlinearity of the gradient produces distortions of the image and interferes with diffusion measurements, and should be kept at a minimum. Several configurations have been described in the literature, but for superconducting magnets coils which can be wound cylindrically to conform with the shape of the NMR probe are preferred. This simplifies the construction and samples can be inserted into the probe in the usual way. Such coils include Golay coils for G_x and G_y, and Maxwell coils for G_z *(56, 80)*. Presumably these same designs were used for the x, y and z shim coils.

One other design which gives uniform gradients with an inductance 10 times less than that of a Maxwell is the quadrupole coil *(81,82)*. However the distribution of windings is such that it is more difficult to construct these for a superconducting magnet.

The magnetic field, **B**, produced at a point P by an electric current passing through a wire is given by the Biot-Savart law *(83)*

$$B(\underset{\sim}{r}_2) = \frac{\mu_o I}{4\pi}\oint \frac{d\underset{\sim}{\ell} \times (\underset{\sim}{r}_2 - \underset{\sim}{r}_1)}{|\underset{\sim}{r}_2 - \underset{\sim}{r}_1|^3} \qquad [2.82]$$

where I is the current, $\mathbf{r}_1$ and $\mathbf{r}_2$ are the position vectors for the point P and the current element **dl** respectively (Fig. 2.10). The integral is over every element **dl** of the closed loop in which the current flows. The magnetic induction due to two or more current loops is the vector sum of the magnetic induction produced by the individual elements separately.

The magnetic field produced by any coil is inhomogeneous. A simple illustration of this is the field produced by a single current loop. Along the axis of the loop, the direction of **B** parallel to the axis and its magnitude is given by

$$|\underset{\sim}{B}| = \mu_o I \frac{r^2}{2(z^2 + r^2)^{\frac{3}{2}}}. \qquad [2.83]$$

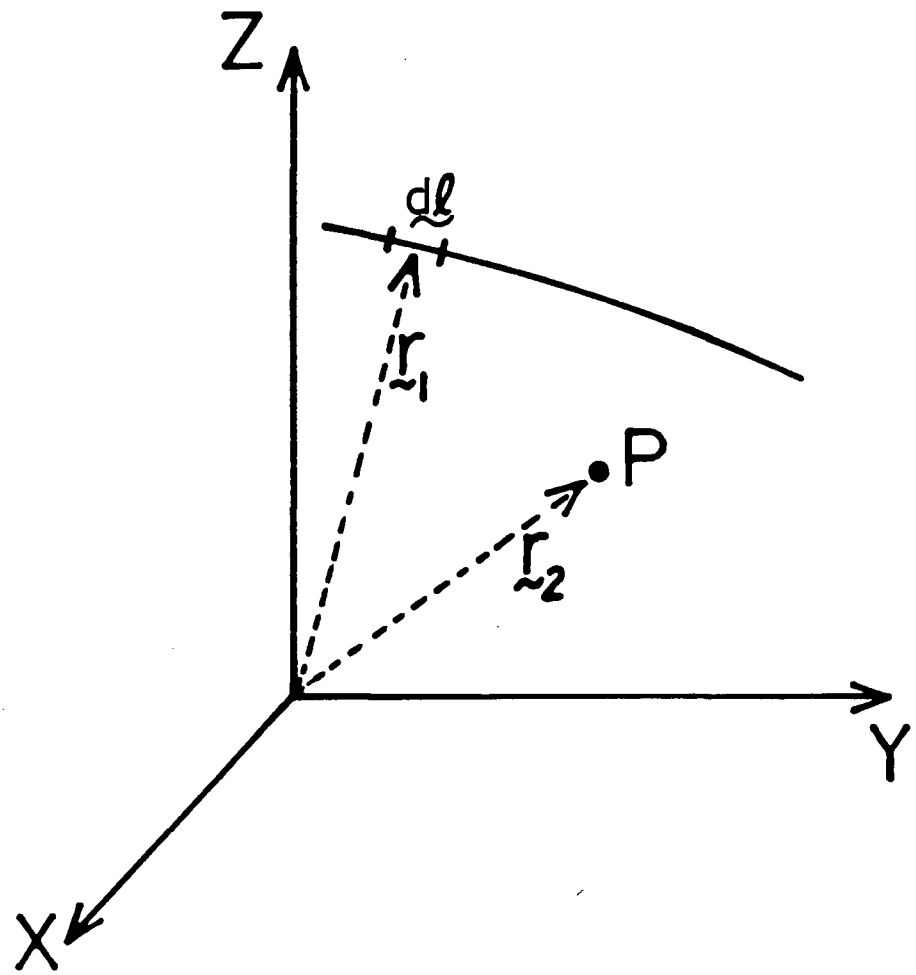

Fig. 2.10 The coordinates of the current element **dl** which produces a magnetic field at point P, with position vectors $\mathbf{r}_1$ and $\mathbf{r}_2$ respectively.

In general, the gradient of a magnetic field, **B**, is a second rank tensor,

$$\underset{\approx}{g} = \underset{\sim}{\nabla}\underset{\sim}{B} = \sum_{i,j} \frac{\partial B_i}{\partial j} \hat{i}\,\hat{j} \qquad i,j = x,y,z \qquad [2.84]$$

but in the presence of a much larger field $\mathbf{B}_0$, only those components with B parallel to the main field contribute significantly and to good approximation *(1)*

$$\underset{\sim}{G} = \frac{\partial B_z}{\partial x}\hat{x} + \frac{\partial B_z}{\partial y}\hat{y} + \frac{\partial B_z}{\partial z}\hat{z} \qquad [2.85]$$

Thus for the field along the axis of the current loop, the gradient, G_z, is given by

$$G_z = -\frac{3}{2}\mu_o I \frac{r^2}{(z^2 + r^2)^{\frac{5}{2}}} \qquad [2.86]$$

which is also not constant. However a uniform gradient is required to produce an undistorted image and the resolution depends upon the inhomogeneities of the applied fields.

The Maxwell[1] coil consists of two sets of circular loops of wire connected so that current passing through them will generate opposing magnetic fields. By symmetry, the even order derivatives of the fields cancel. The separation of the opposing loops is chosen so that the third derivative is zero at the coil center *(84)*. The resulting geometry is shown in Fig. 2.11(B).

---

[1]Originally referred to as anti or opposed Helmholtz coil.

Fig. 2.11 (A) Cross-sectional view through the sample chamber of the NMR probe with the outer aluminium can removed. Only the slots for the coil windings which are concentric with the Perspex former are shown. The former also has four slots at right angles to each other for the vertical windings.

(B) & (C) The positions and the directions of the windings for the z-gradient (Maxwell) coil and the y-gradient (Golay) coil respectively. The x-gradient coil is the same as in (C) but rotated through 90°.

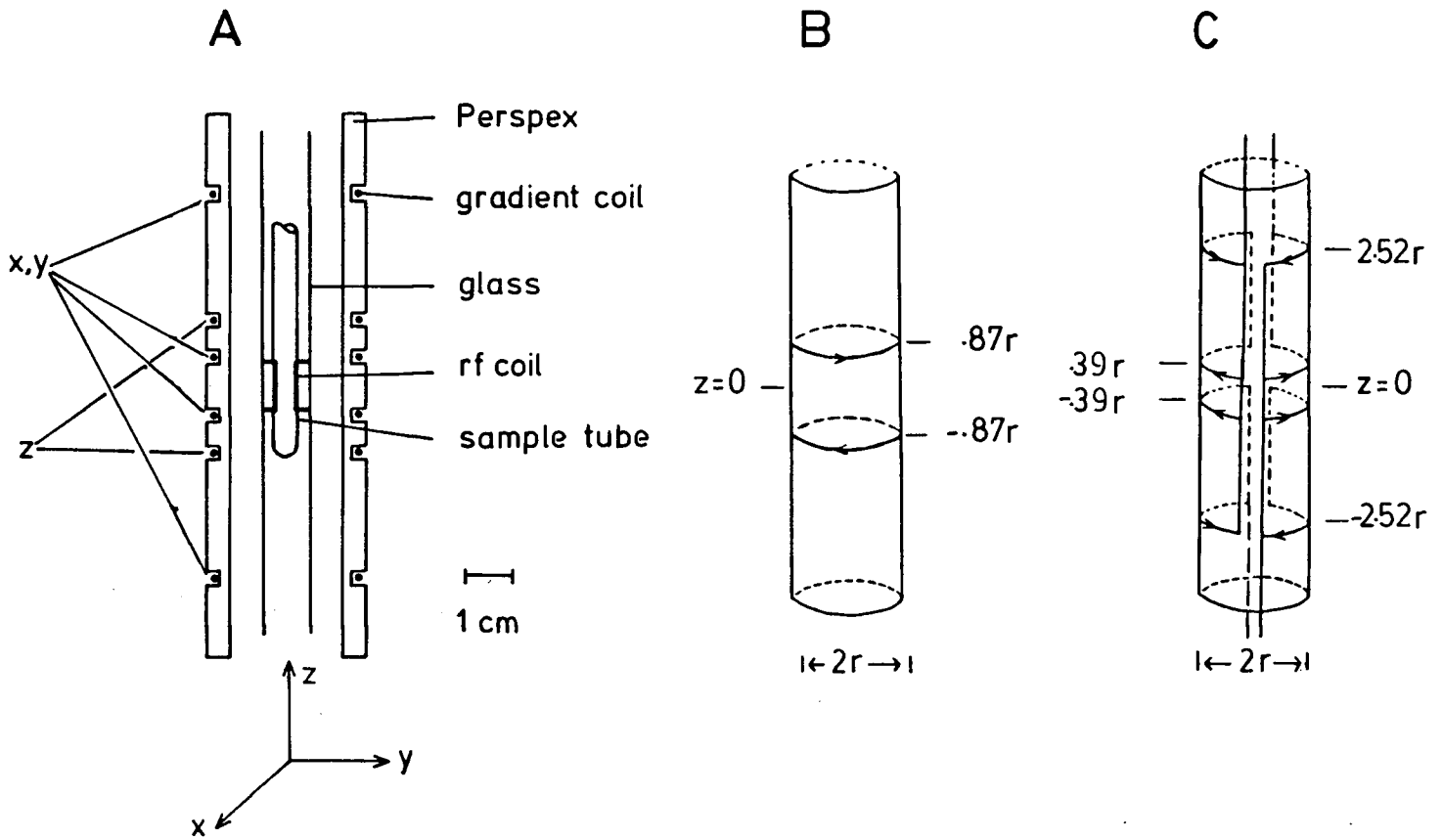
A
B
C
Perspex
gradient coil
glass
rf coil
sample tube
x,y
z
1 cm
z
y
x
z=0
.87r
-.87r
I← 2r →I
2·52r
·39r
-·39r
z=0
-2·52r
I← 2r →I

The Golay coil design is based upon the expansion of the magnetic field in terms of spherical harmonics *(85)*

$$\underset{\sim}{B} = -\underset{\sim}{\nabla}\Phi$$

where

$$\Phi = -\sum_{n=1}^{\infty}\sum_{m=0}^{n} r^n P_n^m(\cos\theta)[A_n^m \cos m\phi + B_n^m \sin m\phi]. \qquad [2.87]$$

In the presence of a strong magnetic field B_0 chosen to lie along z, the z component and its derivatives may be expressed in terms of the spherical expansion

$$B_z = -\cos\theta \frac{\partial\Phi}{\partial r} + \frac{\sin\theta}{r} \frac{\partial\Phi}{\partial\theta}. \qquad [2.88]$$

The first few terms of this expansion include those which vary with x, y, z and x^2-y^2 *(84)*. Originally such coils were constructed by positioning conductors on the surface of a sphere along the locus of a particular spherical harmonic function where the function vanished, keeping track of the positive and negative values of the function. These geometrical configurations of the current flow loci were then projected, viewed from the center of the sphere, to flat pole faces for an electromagnet. A modified version for producing x and y gradients for a superconducting magnet is described by Hoult and Richards *(80)*.

Numerical evaluation of the Biot-Savart law shows that the Golay coil produces gradients which are linear to within

-5% over a region $r \leq 0.5a$ where a is the coil radius *(56)*.

The specifications for the location of current elements in Fig. 2.11(B) & (C) define surfaces on which the coils should be wound so that optimal linearity of the gradients is achieved. When coils for x, y and z gradients were all to be wound on the same former, it was necessary to simplify these shapes to slots as shown (Fig. 2.11(A)).

The probe used in this work consisted of the usual components of a high resolution device, fitted inside an aluminium tube of 37 mm outer diameter. The outer glass Dewar, which normally provides thermal insulation for variable temperature operation was removed and replaced by a Perspex cylinder of outer diameter 34 mm and wall thickness 5 mm. Grooves, 3 mm deep and 3 mm wide, machined into the outer surface provided the physical localization of the 27 gauge, insulated copper wire used for the gradient coils (Fig. 2.11(A)). Initially, 8 turns each were used for the three coils but another set with 12 turns for x and y, and 20 turns for z was used for the majority of the work. The magnitudes of the gradients produced by these coils are given in Table 2.1, and were determined by methods to be discussed in the results section. High frequency filters (Fig. 2.12(A)) on both leads of each coil minimized the inductive coupling with the rf coil. Resistors connected in series with the coils served to increase the impedance and reduce problems with feedback. An interface with DAC (digital to analog converter) input from the computer and

Coils for 270	Number of turns	Gradient Magnitudes ($mTm^{-1}A^{-1}$)	Resistance (Ω)	Inductance (μH)
A. X	8	38·9	1·1	35
Y	8	38·2	1·1	32
Z	8	—	0·6	12
B. X	12	48·3	1·8	60
Y	12	50·4	1·6	62
Z	20	65·5	1·0	43
Radius of coils	1·6 cm			
Gauge of wire	27			
C. X,Y shims	—	1·1 mTm^{-1}		
D. Coils for 80				
X	10	1·82	1·1	360
Y	10	1·82	1·1	370
Z	15	1·85	0·5	110
Radius of coils	8 cm			
Gauge of wire	12			

Table 2.1 Specifications and gradient magnitudes of gradient coils for the modified high resolution probe in (A) and (B), the x and y shim coils of the high resolution magnet in (C), and for the surface coil apparatus in (D).

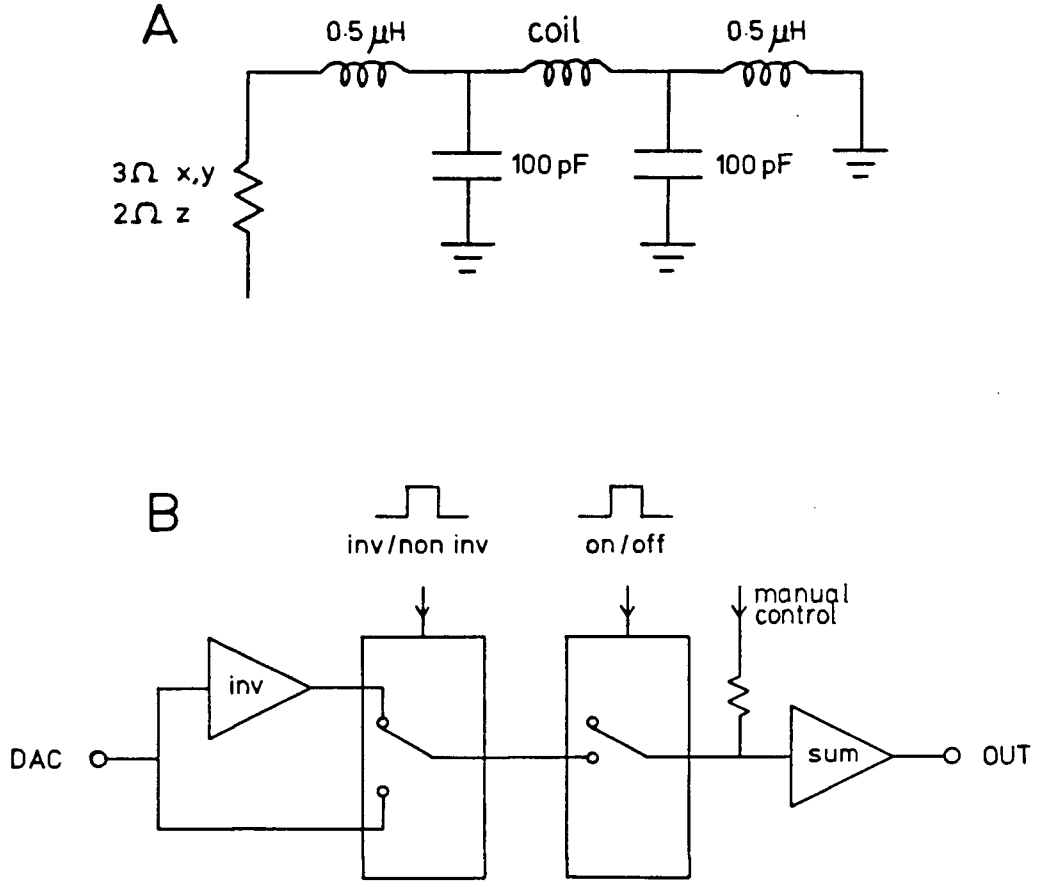

Fig. 2.12 (A) Circuit diagram for the high frequency filters placed on each lead of the gradient coils.

(B) Schematic diagram of the gradient control unit.

control lines from the Nicolet 293B pulse programmer allowed the generation of variable amplitude TTL control pulses (Fig. 2.12(B)). Audio amplifiers (AMCRON M-600 and TECRON 7560, supplied by CROWN INTERNATIONAL) working in the constant voltage mode and with variable gain controls provided currents up to 20 A. However, the amplifiers were susceptible to feedback at high gains and in electronic testing it was found that up to 15 A could be produced safely. Measurement of the voltage across the resistors in series with the coils using an oscilloscope, showed rise times were 60 μs for the achievement of 98 % of gradient pulse. The linearity of output was better than 99 % (Fig. 2.13). Correspondingly, gradient pulses were applied for a minimum of 1 ms. NMR signals were measured using a saddle shaped transmitter-receiver coil, 11.5 mm in diameter, with a 180° pulse length of 29 μs.

Further complications were observed in actual NMR experiments. The first was from eddy currents induced by gradient pulses in the aluminium covering of the probe and the wall of the magnet. Slots, 2 mm wide and 5 cm long, were cut into the covering to minimize eddy currents there. No attempt was made to eliminate such effects in the magnet itself. While eddy currents should decay away in times of about 5-10 ms, much longer variations in the fields lasting for up to 50 ms were observed for moderate gradients of 50 mTm^{-1}. These effects were seen most often in spin echo experiments with gradient pulses applied. The source of

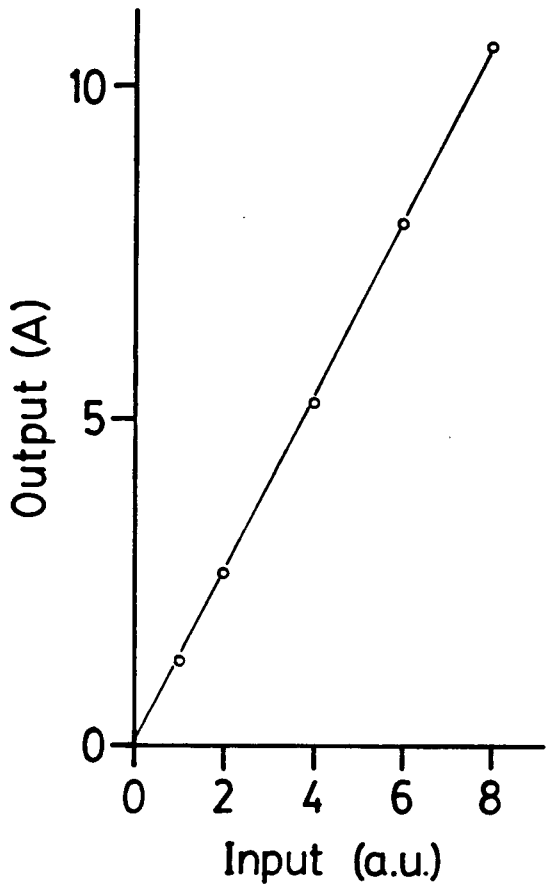

Fig. 2.13 Graph of amplifier output (A) as a function of DAC input (arbitrary units).

these variations is unknown. Interactions with either the shim coils or the main field may be the cause.

2. APPARATUS FOR SURFACE COIL, PULSED GRADIENT SPIN ECHO MEASUREMENTS

Pulsed gradient spin-echo measurements on human forearm (see chapter III) were performed using a 1.9 T, 30 cm bore Oxford Instruments superconducting magnet with a modified Nicolet NT-300 NMR console. The built-in gradient coils of the magnet gave 10 mTm^{-1} for x, y and z directions but were inadequate for diffusion measurements because of long rise-times, which could only be partially overcome by pre-emphasis, and large eddy-current effects. Hence another set of gradient coils was constructed to provide higher gradients with shorter rise times. The x and y coils were wound around pegs on a PVC former, 6.5 inches in outer diameter with 0.25 inch wall thickness. The locations of the pegs were determined using an effective radius of 8.3 cm for the coils. The Z coil was wound in grooves, 3 mm deep and 9 mm wide. The current was provided using the same audio amplifiers as before (section B.2) except the Tecrons were operated in constant current mode. The magnitudes of the gradients produced by the gradient coils were determined by the measurement of linewidths for spectra taken with a spherical bulb[2] (4 cm diameter) filled with

---

[2] $y = 3(r^2 - x^2)/4r^3$ and $W_{1/2} = (4/T_2^2 + 2\gamma^2 G^2 r^2)^{1/2}$ [2.89]

water (Table 2.1).

NMR signals were measured using a 27 mm diameter surface coil consisting of two loops of copper wire with Teflon tape insulation. The distribution of the rf field produced by a surface coil is inhomogeneous and correspondingly the flip angle and contribution of spins to the signal depends upon their position in the coil. For NMR, only the component $B_{1,xy}$ in the xy plane is important. Along the axis of the coil, the magnitude of $B_{1,xy}$ decreases monotonically to a few percent at a distance of 1.5r from the center of the coil, where r is the coil radius *(86,87)*. The exact flip angle distribution and the region from which the signal is obtained will depend upon the pulse length. It is assumed that the signal is detected from a roughly hemispherical region of the diameter of the coil. The surface coil was mounted on a Perspex plate which also provided support for the matching and tuning capacitors (Fig. 2.14). Placement of the surface coil was such that insertion of the arm caused the palm to rest on the plate. It was found necessary to wrap the plate and capacitors with aluminium foil to minimize inductive coupling of the transmitter-receiver coil system, except for the coil itself, with the sample.

The magnet was shimmed using the surface coil and a beaker of water, using an optimal pulse length of 10 μs to produce spectra with linewidths of about 14 Hz.

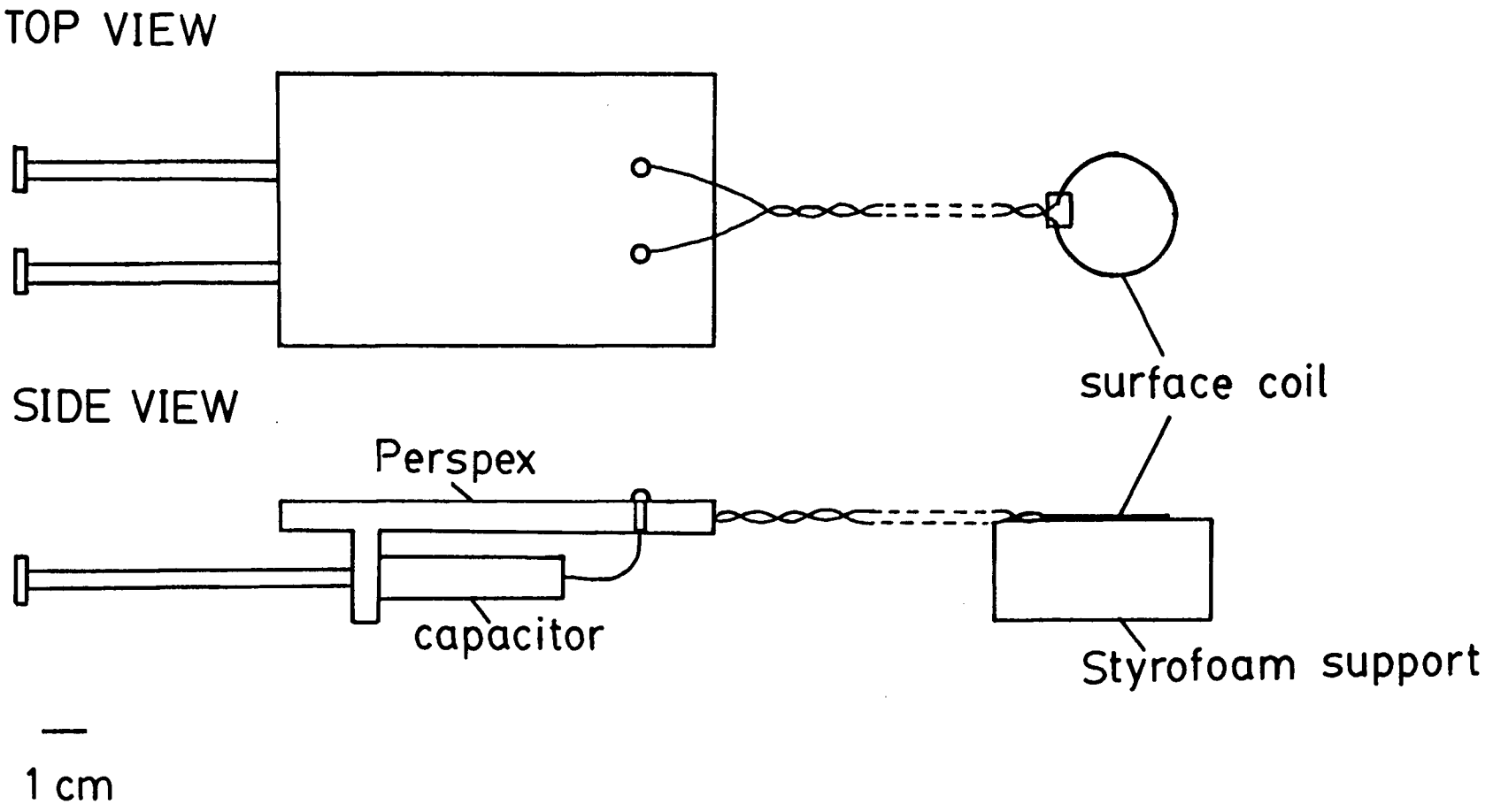

Fig. 2.14 Schematic diagram of surface coil probe.

3. PARAMETERS FOR NMR EXPERIMENTS

All experiments were performed with quadrative phase cycling and automatic baseline correction. In all spin echo experiments, for imaging and diffusion measurement, the 180° pulse was applied alternately along the y and -y directions to compensate for pulse imperfections. In diffusion experiments, data acquisition was initiated at the echo time so that phase sensitive spectra could be obtained. In imaging experiments, the echo time was chosen to coincide with the middle of the data acquisition period.

All NMR signals were baseline corrected and apodized before Fourier transformation. Apodization refers to the multiplication of the time domain NMR signal with a weighting function before Fourier transformation and is used here to improve the signal to noise ratio. For normal 90° pulse and diffusion experiments the weighting function was a decaying exponential e^{-jk}, where integer j = 0 to N-1 for an N point FID, and k is given by

$$k = \frac{\pi \times \text{line broadening}}{2 \times \text{sweep width}}. \qquad [2.90]$$

The line broadening was 0.3 Hz and 3 Hz for high resolution and surface coil spectra respectively. In NMR imaging, a weighting function of the form $\sin(\pi\, j/N)$, where j =0 to N-1 for an N point FID was applied before each Fourier transformation. After the second Fourier transformation, the power spectrum was calculated to produce the image.

The field of view (FV) in a dimension of the NMR image is given by the relation[3]

$$FV = \frac{\text{sweep width (Hz)}}{\frac{\gamma}{2\pi}\,\text{gradient magnitude (Hz/cm)}}. \qquad [2.91]$$

The sweep width must be large enough to encompass the entire spectrum of frequencies in the sample. Also, in order that an undistorted image be obtained, the field of view must be the same in each of the spatial dimensions in the image. For the pulse sequence in Fig. 2.3, this results in the condition $dk_1 = dk_2$ or $\gamma t_1 dG_x = \gamma G_y dt_2$ where k_1 and k_2 are the components of the vector **k** in reciprocal space.

In imaging, the smallest available dwell time was 14 μs so that for 8 mm diameter samples, the maximum gradient which could be used in the detection period is 210 mTm^{-1}.

Images were displayed either as stacked plots of proton signal amplitude versus x-coordinate, each for a fixed y or as images with 16 color levels, from dark to light for increasing proton signal.

Measurements of diffusion from high resolution spectra were by integration of the appropriate signal. For measurements of relaxation times, T_1 and T_2, for biological samples (chapters III and IV) and surface-coil diffusion, peak heights were used because of overlap between peaks.

Straight line fits to data from lineshapes, for the determination of spin-spin relaxation times, and diffusion

---

[3] Sweepwidth of the receiver, see footnote number 6, p.85.

coefficients were obtained by linear least squares. The error was estimated from the uncertainty in the slopes and correspond to ± two standard deviations. For curve fitting to lineshape data a Nicolet data reduction routine for quartic polynomials was used.

Spin-lattice relaxation times were calculated from inversion-recovery data using a three parameter fit to the function *(88)*

$$y = A\{1-[1+W(1-e^{-k/T})]\ e^{-x/T}\} \qquad [2.92]$$

where A is the equilibrium value, W accounts for the initial magnetization, T_1 is the spin-lattice relaxation time and k is the relaxation delay.

All measurements were performed at room temperature.

B. RESULTS AND DISCUSSION

1. GRADIENT MAGNITUDES

Normal NMR spectra for water in an NMR tube, recorded after the application of a 90°_{x}-pulse in the presence of a static gradient, are shown in Fig. 2.15. The gradients were obtained using the x and y shim coils of the superconducting magnet.

The magnitude of the gradient produced by the shim coil calculated from the linewidth at half-height, $G_x = 1.11\ mTm^{-1}$, is consistent with values calculated from a

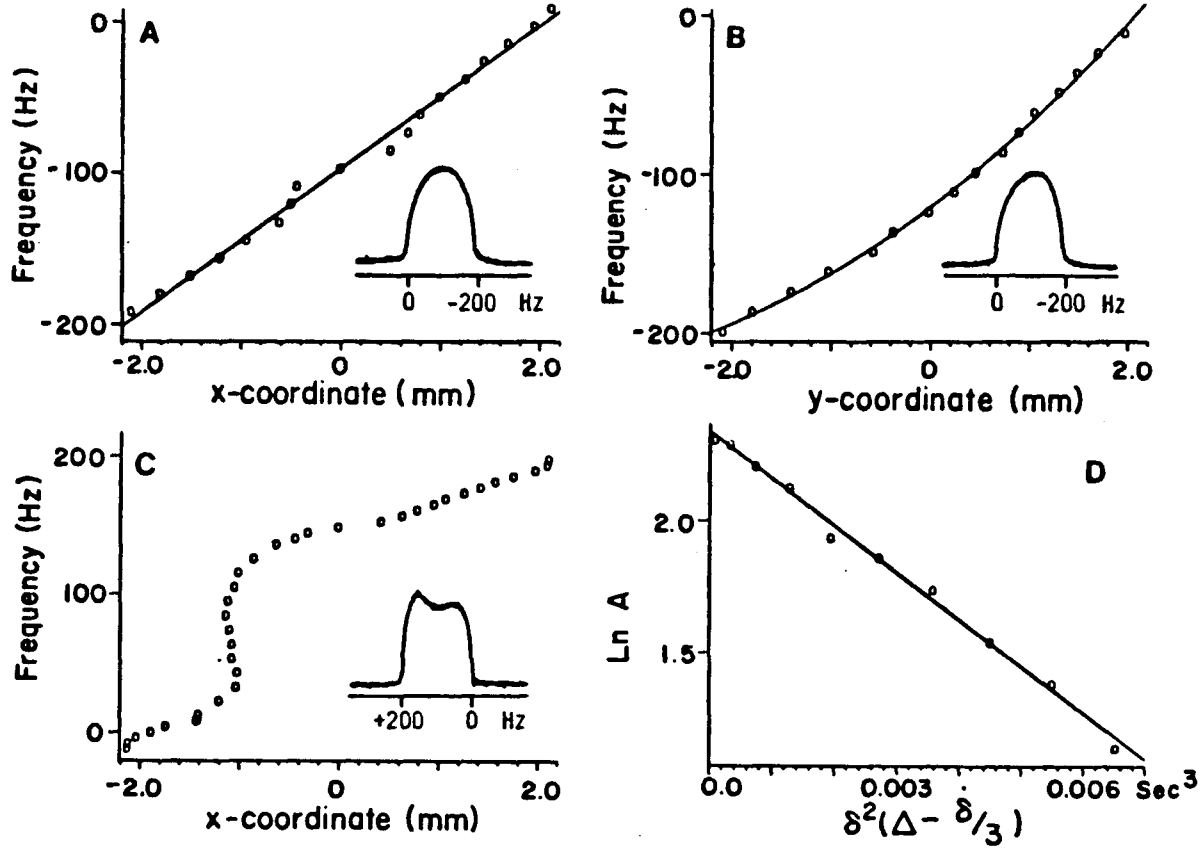

Fig. 2.15 Spectra and graphs of Larmor frequency *vs* position for the x shim coil (A), y shim coil (B) and x shim coil (C) with a smaller transmitter-receiver coil (6 mm diameter). (D) shows the attenuation of the spin echo in pulsed gradient diffusion experiment (Δ = 280 ms, δ = 20-200 ms).

graph of Larmor frequency as a function of position (Fig. 2.15(A)) and calibration via a spin echo experiment with pulsed gradient using known values for the self-diffusion coefficient of water (Table 2.2). The value, G_x = 2.5 mTm^{-1}, obtained by taking the average from the first five zeroes of $J_1(G_x rt)$ was much too large. When larger gradients were used, the values of G_x obtained from the four methods were in excellent agreement suggesting that nonlinearities were affecting the values from the $J_1(G_x rt)$ calculation for weak gradients produced by the shim coils. In an experiment in which the magnet was not optimally shimmed, an asymmetric spectrum for the y shim coil was obtained (Fig. 2.15(B)). The asymmetry was independent of the orientation of the probe, confirming our supposition that nonlinearity of the effective y gradient and not an inhomogeneous distribution of radiofrequency power was the cause. The graph of Larmor frequency *vs* y coordinate was a smooth curve corresponding to a linear gradient of 1.08 mTm^{-1}, which is similar in magnitude to that produced by the x shim, and a $\frac{d^2B_z}{dy^2}$ component of 1.2 mTm^{-2}. The other methods only allowed the estimation of the linear component of the gradient (Table 2.2). The nonlinearity observed in the gradients is dependent on how well the magnet is shimmed; the x^2-y^2 shim can be adjusted to cause either the x or y gradient to be nonlinear. The distortion shown in the spectrum and the discontinuity in the graph of Fig. 2.15(C) are due to an inhomogeneous distribution of

Method of calculation	x-shim	y-shim	x-gradient
Linewidth	1.11 ± 0.02[a]	1.08 ± 0.02	2.43 ± 0.03
Lineshape[b]	1.12 ± 0.04	1.10 ± 0.06[c]	2.51 ± 0.09
Calibration[d]	1.11 ± 0.05	1.04 ± 0.09	2.39 ± 0.11
$J_1(Grt)$	2.47 ± 0.3	2.79 ± 0.3	2.45 ± 0.3

[a] Uncertainties are $\pm 2\sigma$

[b] From graphs of frequency vs. position

[c] $G'_y(o) = 1.2 \pm 0.2$ mTm^{-2}

[d] By a pulsed field gradient diffusion experiment.

Table 2.2 Gradient magnitudes by linewidths, lineshapes, $J_1(Grt)$ and calibration by diffusion.

radiofrequency power from a smaller transmitter coil (diameter 6 mm).

A Golay coil of radius 15 mm consisting of 8 turns of number 27 gauge wire was found to produce a gradient of about 38 $mTm^{-1}A^{-1}$. In an experiment with a current of 64 mA, the magnitude of gradient calculated from the linewidth, $G = 2.43\ mTm^{-1}$, was in good agreement with that obtained from a diffusion experiment, $G = 2.39\ mTm^{-1}$.

2. EFFECT OF RECEIVER DEAD TIME

A difficulty with the analysis of lineshapes with large frequency dispersion, as will arise when large gradients are used, is associated with the fast decay of the time domain signal (Fig. 2.16). Normal procedure is to allow a delay before beginning acquisition to avoid breakthrough of the radiofrequency pulse *(55)*. The loss in intensity and information content when the initial part of a rapidly decaying signal is not acquired, leads to a reduction in signal to noise ratio and a characteristic base line distortion. With the signal set equal to zero during the deadtime, the resulting spectrum is a convolution of the ideal spectrum with $(-\sin x)/x$. Those problems have been surmounted by utilizing a natural feature of spin-echo experiments: the formation of the echo produces a secondary signal which can be acquired without the effect from dead time provided the echo time is much longer than the dwell

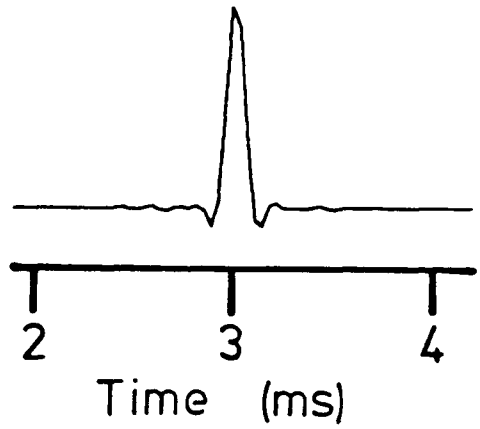

Fig. 2.16 The spin echo signal is acquired in the presence of a y-gradient of 76 mTm^{-1} and lasts for about 0.3 ms.

time[4].

The gradient spectra in Figs. 2.17(A) and (C) were acquired after the application of a 90° pulse in the presence of a static y-gradient of 21 mTm^{-1} and with dwell times of 100 μs and 50 μs respectively while Figs. 2.17(B) and (D) show the corresponding spin echo spectra, obtained by magnitude calculation[5]. Comparison of the spectra shows that the spin echo spectra give much better signal to noise and lineshapes. The spectrum in Fig. 2.17(C) shows some improvement over that of Fig. 2.17(A) because of reduced dwell time, and shorter dead time.

3. EFFECT OF RADIOFREQUENCY INHOMOGENEITY

As observed in spectrum (C) of Fig. 2.15, a further difficulty in lineshape measurements stems from radiofrequency inhomogeneity. Consideration of the standard arrangement for NMR probes wherein the sample extends beyond the region of the transmitter coil (Fig. 2.11(A)), to maximize signal strength and minimize susceptibility variations, shows that the distribution of B_1 along the z direction is inhomogeneous. In order that lineshape analysis be valid for x and y gradients it is required that $B_1(x)$ and

---

[4] Dwell time: The time interval between successive samples of the time domain NMR signal by the digitizer. For quadrature detection the width of the observed spectrum or sweep width, is given by $\pm$ (2 x dwell time)$^{-1}$. Usually the dead time is automatically set equal to the dwell time.

[5] Magnitude calculation: The real and imaginary parts of the spectrum S are combined to give $S = (ReS^2 + ImS^2)^{1/2}$.

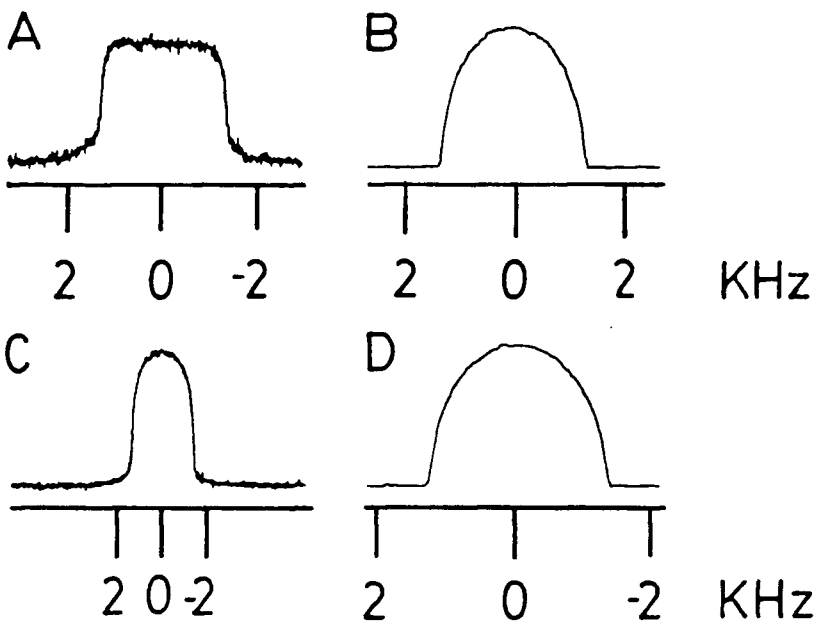

Fig. 2.17 (A) & (C) Spectra recorded after the application of a 90° pulse in the presence of a gradient with dwell times 100 μs and 50 μs respectively. (B) & (D) The corresponding spin echo spectra obtained by magnitude calculation with dwell times 100 μs and 50 μs respectively. These spectra were acquired with 90° and 180° pulse lengths of 13 μs and 27 μs respectively; a 10 ms, 21 mTm^{-1}, y-gradient pulse immediately after the 90° pulse then a delay of 40 ms before the 180° pulse. The y-gradient was switched on again 40 ms after the 180° pulse. The echo time was 100 ms and the relaxation delay was 6 s.

$B_1(y)$ be uniform. These conditions were verified by mapping the distribution of B_1 across the sample.

A two-dimensional experiment for mapping $B_1(x)$ and $B_1(z)$ consists of a spin-echo pulse sequence with the duration of the excitation pulse incremented for the evolution period and the acquisition of the signal in the presence of a gradient for the detection period (Fig. 2.18). The resulting map shows the distribution of frequencies, $\omega_1 = \gamma B_1$, along one direction across the sample. In Fig. 2.19(A) showing the z-distribution of ω_1, the non-uniformity observed at 0.5 cm or greater away from the center corresponds to the extent of the transmitter-receiver coil which is 1 cm in length. The y-distribution of ω_1 extends across the NMR tube and shows much better uniformity (Fig. 2.19(B)). The width of the peaks indicates a distribution of ω_1 that exists over a given slice through the sample. The frequency at the center of the peaks, 19.7 KHz, corresponds to a 90° pulse length of 12.7 μs, in good agreement with the value 13 μs obtained by measuring intensities of normal high resolution spectra. Thus the distribution of radiofrequency radiation across the sample that is produced by the transmitter-receiver coil is uniform in the y direction and non-uniform in the z-direction. Consequently, gradient magnitudes can be determined from lineshapes for the y-gradient but not for the z-gradient.

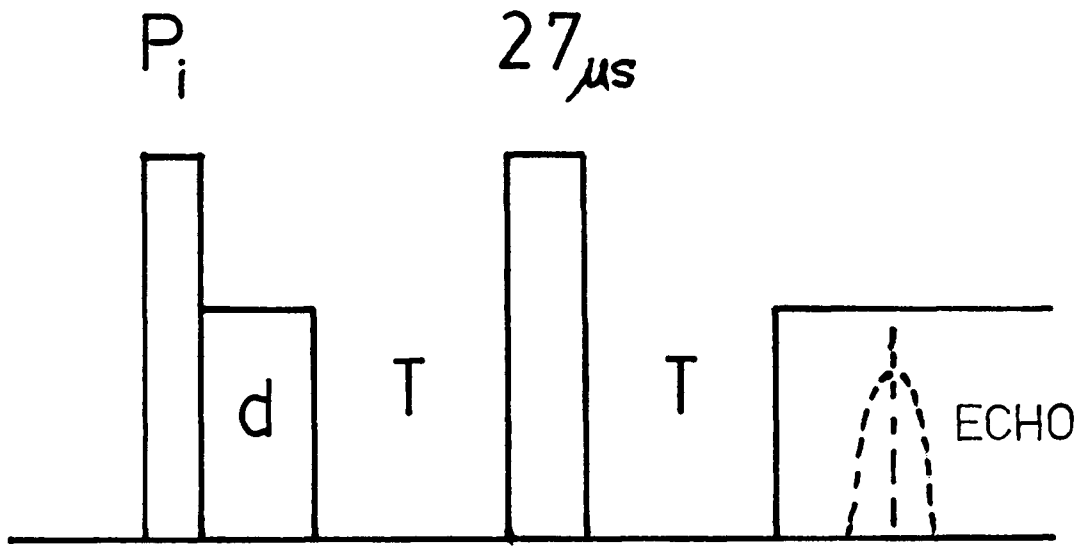

Fig. 2.18 Pulse sequence for the one dimensional mapping of the distribution of the rf field across the sample. The excitation pulse P_i is incremented for the evolution period. A gradient pulse of duration d, followed by a delay T, a 180° pulse, a further delay T and finally a gradient pulse during the detection period produces an echo at 2(d+T).

Fig. 2.19 The one dimensional maps for the distribution of ω_1 for the z (A) and y (B) directions. The spectra were recorded using the pulse sequence in Fig 2.13 with d and T intervals of 5 and 20 ms respectively, 180° pulse of 27 μs and excitation pulse, P_i, incremented from 15 μs to 960 μs in increments of 15 μs. For (A) the fixed z-gradient was 24 mTm^{-1} and for (B) the fixed y-gradient was 25 mTm^{-1}. The saddle shaped transmitter-receiver coil was 11.5 mm in diameter.

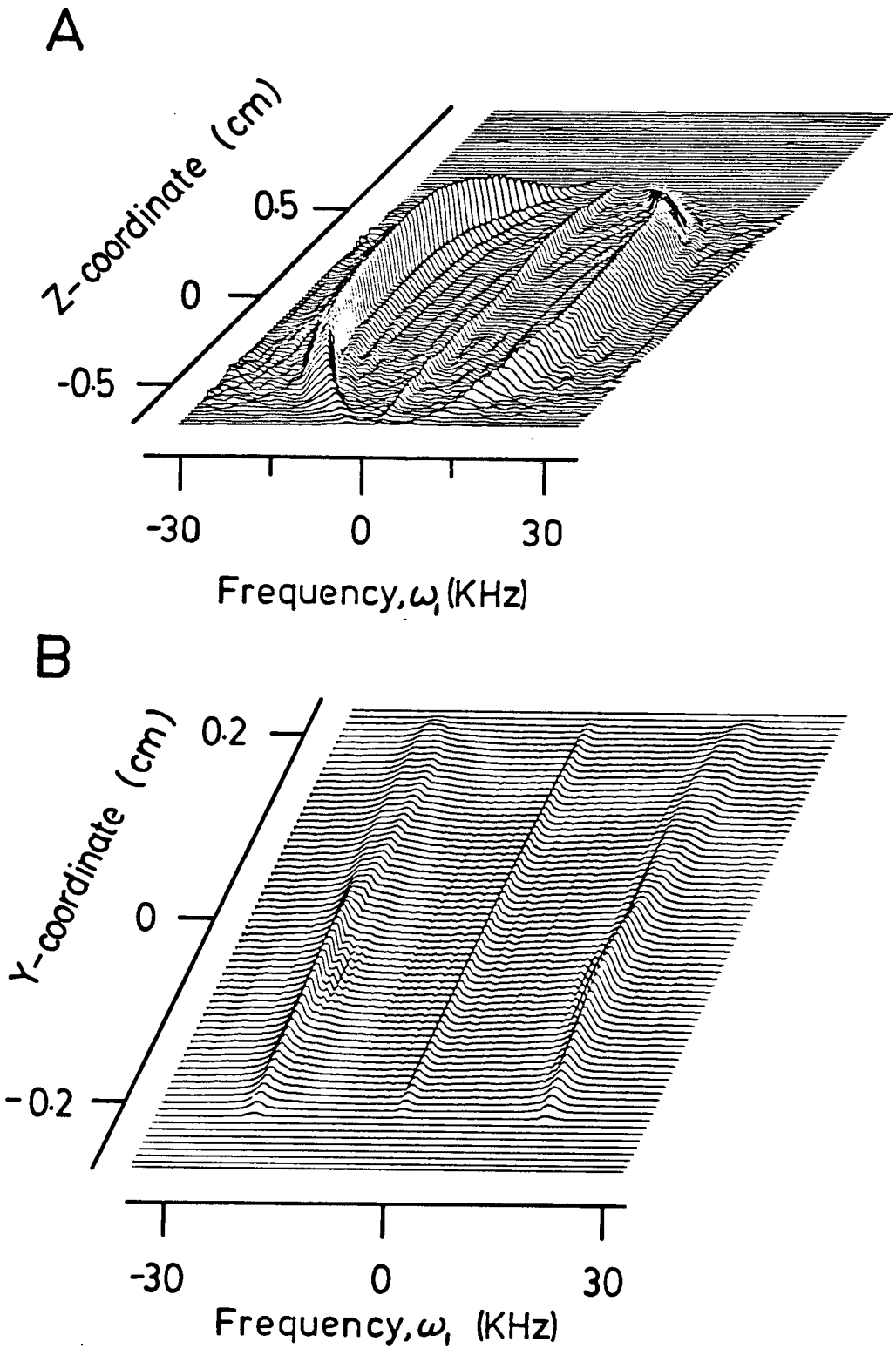
A
Z-coordinate (cm)
0.5
0
-0.5
-30
0
30
Frequency, ω_1 (KHz)
B
Y-coordinate (cm)
0.2
0
-0.2
-30
0
30
Frequency, ω_1 (KHz)

4. STATIC GRADIENT DIFFUSION MEASUREMENT

For comparison with the previous experiments with gradients of 1.1 mTm^{-1} and 2.4 mTm^{-1} (Fig. 2.15), spectra with gradients of 75 mTm^{-1} and 151 mTm^{-1} are shown in Fig. 2.20. Despite the background gradients produced by the gradient coil system, the magnet can still be shimmed to produce linewidths of 4 Hz for an NMR tube (Fig. 2.20(A)). The spectrum in Fig. 2.20(C) is in good agreement with the expected lineshape as indicated by the graph of frequency *vs* position from Eq. 2.47 (Fig. 2.20(D)). In Fig. 2.21(A) a stacked plot of spectra from a static gradient diffusion experiment for water in a glass capillary is shown. A capillary was chosen since this would allow the use of large gradients without significant resonance offset effects[6] during the rf pulses which would further complicate the lineshape *(89)*. The intensity of the spectra decreases as the echo time, 2τ, is increased. From the linewidth at half-height, the effective gradient is 130 mTm^{-1} and from the slope of the line in Fig. 2.21(B), an absolute value for the diffusion coefficient of water, 2.23 x 10^{-9} m^2s^{-1}, was obtained. This value was in agreement with the literature value of 2.19 x 10^{-9} m^2s^{-1} for a temperature of 23 °C *(11)*, a difference of about 2 %. Possible sources of error in the measured diffusion coefficient include temperature, which is only known approximately since the sample was not thermostated, imprecision in the value for the radius of the

---

[6] The condition $\omega_1 >> (\omega_0-\omega)$ for all of the spins in the sample may no longer apply.

Fig. 2.20 (A) Normal 90° pulse spectrum for water in a NMR tube; the linewidth is about 4 Hz.

(B) Spin echo spectrum with 90° and 180° pulse lengths of 13 and 27 μs, y-gradient pulse of 151 mTm^{-1} and duration 1.5 ms following the 90° pulse, delay 2 ms immediately before and after the 180° pulse and acquisition with the y-gradient on. The echo time was 7 ms and the dwell time 16 μs.

(C) Spin echo spectrum with the same pulse sequence as in (B) but with y-gradient pulse of 75 mTm^{-1} and duration 1 ms followed by a delay of 4 ms. The echo time was 10 ms and the dwell time 33 μs.

(D) Graph of ω *vs* x for data from (C); a gradient of 74.6 mTm^{-1} was calculated from the slope.

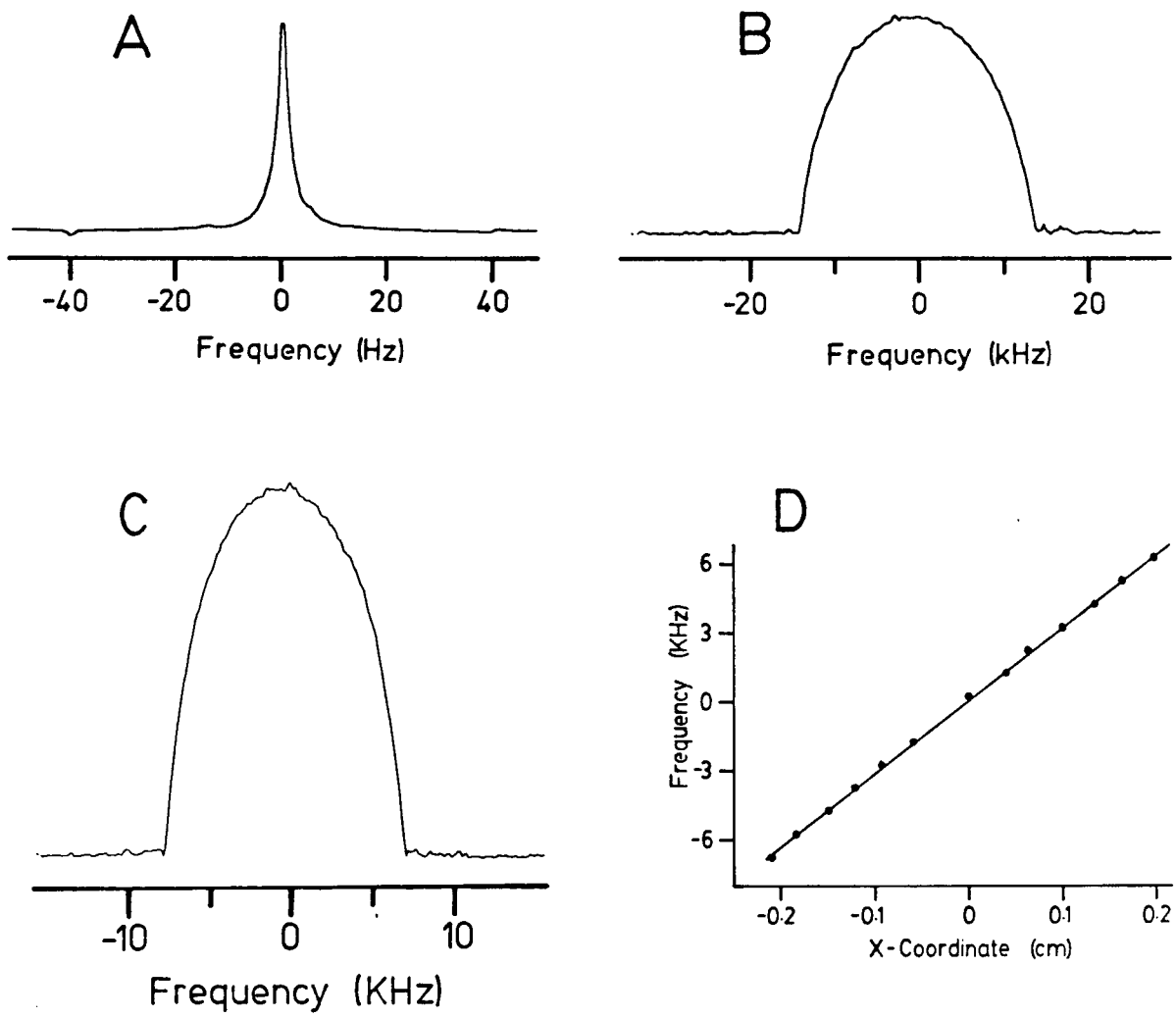
A
-40
-20
0
20
40
Frequency (Hz)
B
-20
0
20
Frequency (kHz)
C
-10
0
10
Frequency (KHz)
D
6
3
0
-3
-6
Frequency (KHz)
-0·2
-0·1
0
0·1
0·2
X-Coordinate (cm)

Fig. 2.21 (A) Spectra from a static gradient diffusion experiment for water in a glass capillary. The radius, 0.610 mm, of the capillary was estimated from the volume of water (assuming a density of 1 g/ml) in a length, l, of the tube ($V=\pi r^2 l$). From the linewidth the effective gradient is 129 mTm^{-1}. The data were acquired using a Hahn echo pulse sequence with the y-gradient applied throughout. The echo time (2τ) was incremented from 5 ms to 25 ms in 20 increments of 1 ms. The decay of the water signal over this time interval was negligible and no correction for T_2 was needed. Room temperature was 23 °C.
(B) Plot of $Ln(A/A_0)$ *vs* τ^3 for the spectra in (A).

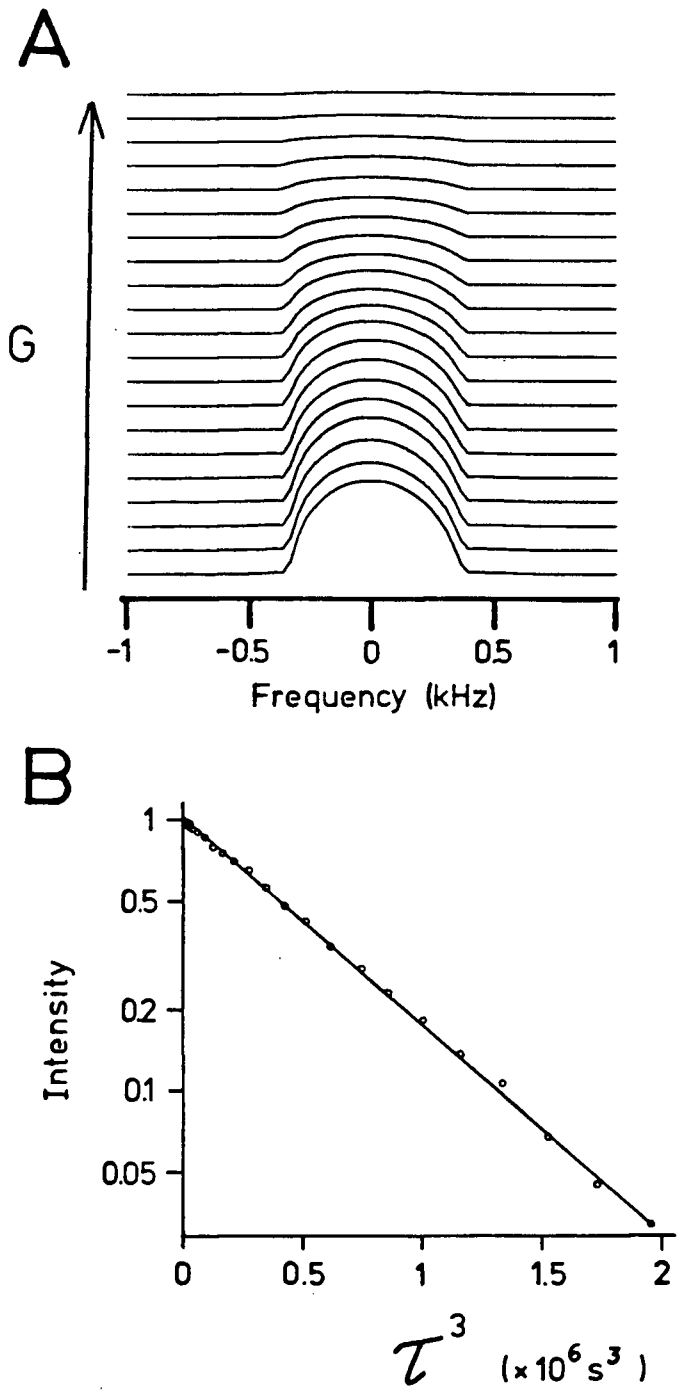
A
G
-1
-0.5
0
0.5
1
Frequency (kHz)
B
Intensity
1
0.5
0.2
0.1
0.05
0
0.5
1
1.5
2
τ³ (×10⁶ s³)

capillary tube and misalignment of the tube.

5. PULSED GRADIENT DIFFUSION MEASUREMENTS

The pulsed gradient experiment requires gradient pulses to be applied equally before and after the 180° pulse (Fig. 2.7). The decay of the echo is given by Eq. [2.68]. Pulsed field gradient spectra acquired with varying delay times after the gradient pulse and the corresponding graph of intensity *vs* delay time are shown in Fig. 2.22. The reduction in intensity for delay times less than 25 ms is due to the effect of either eddy currents or trailing of the gradient pulse. The application of the 180° pulse in the presence of either of these would result in an unequal dephasing and rephasing of the spins. This would cause either a time shift, a decrease in the amplitude of the echo or both. In either of these cases, the effect is most severe for the shortest delays. However at delays longer than 25 ms the echo decays in a normal fashion. The overlap between the 180° pulse and the "tail" of the gradient pulse is small, and the effective applied gradient is the same before and after the 180° pulse for those delays. The decay of the spin echo from water at 23 °C, in a pulsed gradient diffusion experiment is shown in Fig. 2.23. Gradient pulses of 3 ms and a separation of 43.5 ms between the pulses were sufficient to produce a linear plot of $Ln(A/A_0)$ *vs* $\gamma^2G^2\delta^2(\Delta-\delta/3)$. Using values for the gradient magnitude obtained from lineshape analysis, the diffusion

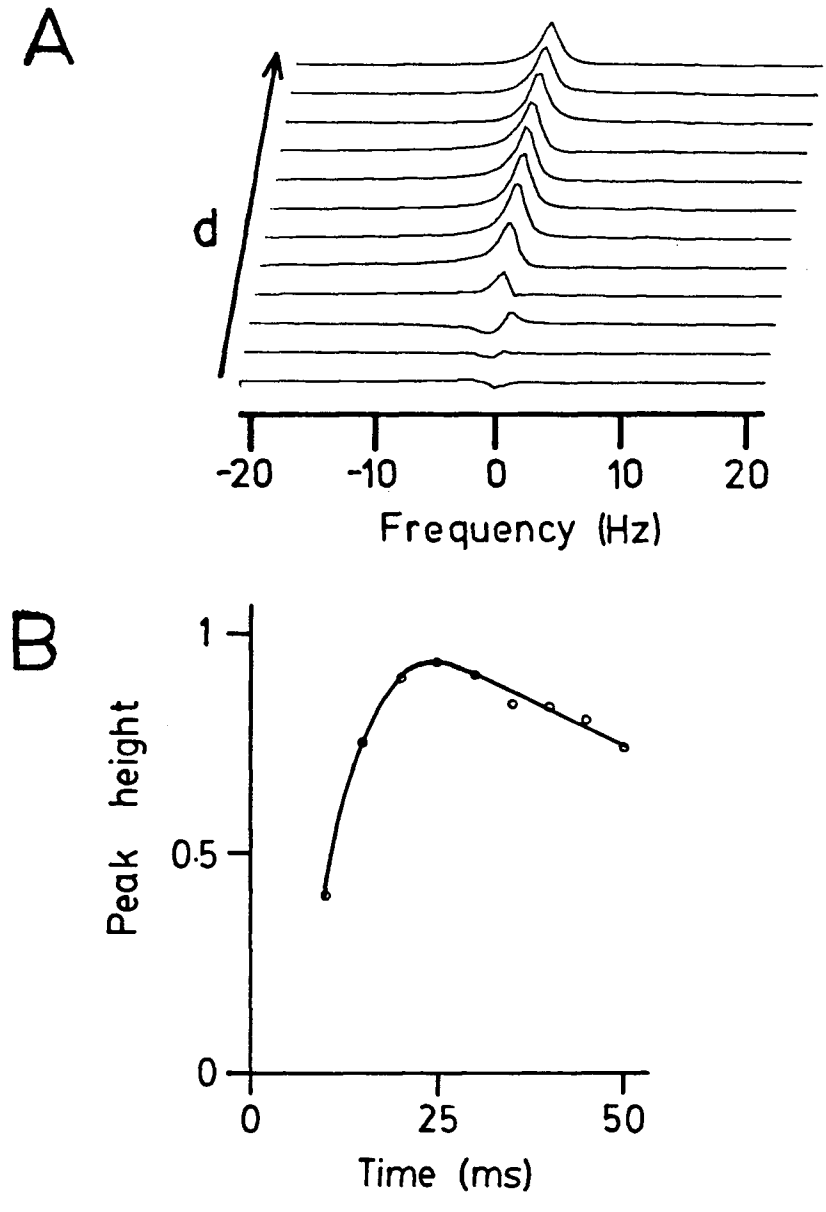

Fig. 2.22 (A) Pulsed field gradient spin echo spectra for water. Y-gradient pulses of 25.2 mTm^{-1} and 10 ms in duration were used. The delay, d, following the gradient pulses varied from 1, 2, 4, 10, 15, 20, 25, 30, 35, 40, 45 and 50 ms. Acquisition was triggered at time 2τ.

(B) Graph of peak height *vs* time d.

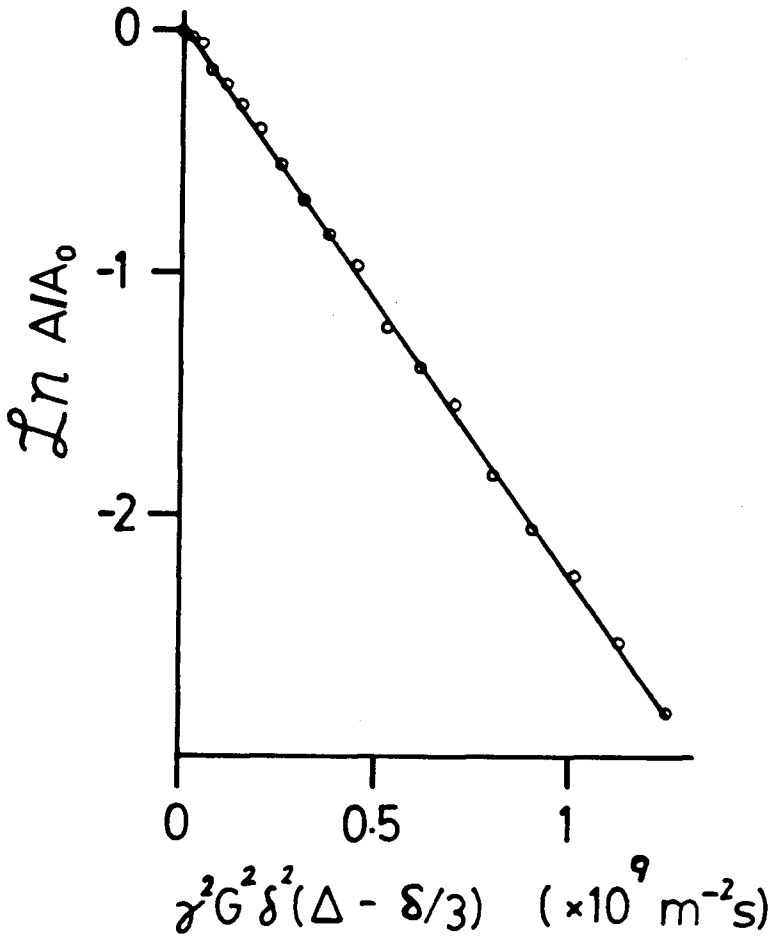

Fig. 2.23 Decay of the spin echo from water in pulsed gradient diffusion experiment. The gradient pulses were 3 ms in duration and varied from 2.13 mTm^{-1} to 83.1 mTm^{-1} in 19 increments of 4.26 mTm^{-1}. The time between the gradient pulses was 43.5 ms. Room temperature was 23 °C.

coefficient of water calculated from the slope was 2.27 x 10^{-9} m^2s^{-1}; the literature value is 2.19 x 10^{-9} m^2s^{-1} *(11)*, a difference of 3.7 %. The larger observed value is probably due at least in part to the effects described above since these would serve to increase the effective duration of the gradient pulse, thereby tending to cause the echo to decrease further than would otherwise be the case. Another possible source of error lies in the variation in temperature since the sample was not thermostatted. With these experimental uncertainties in mind, in pulsed field gradient diffusion experiments it is still preferrable to use water as the standard for determining the effective gradient for a particular experiment, thereby allowing for both trailing of the gradient pulses and eddy currents.

Similar effects were observed with the larger gradient coils constructed for surface coil measurements. In Fig. 2.24, the echo attenuation from pulsed gradient diffusion experiments for water, in which the y-gradient was incremented from 1.1 to 8 mTm^{-1} with gradient pulse duration of 20 ms and echo time of 1.04 s, is shown. Data obtained normally by integration of the water signal are indicated by a closed circle, with the copper shield[7] removed, by an open triangle, and from peak heights with the shield in place, by an open circle. The expected decay using values for gradient magnitude from Table 2.1 is shown by the straight line. In

---

[7] copper cylinder, 26.5 cm o.d. and 1/16 in wall thickness, which lines the bore of the magnet and acts as shielding from unwanted radiofrequency radiation.

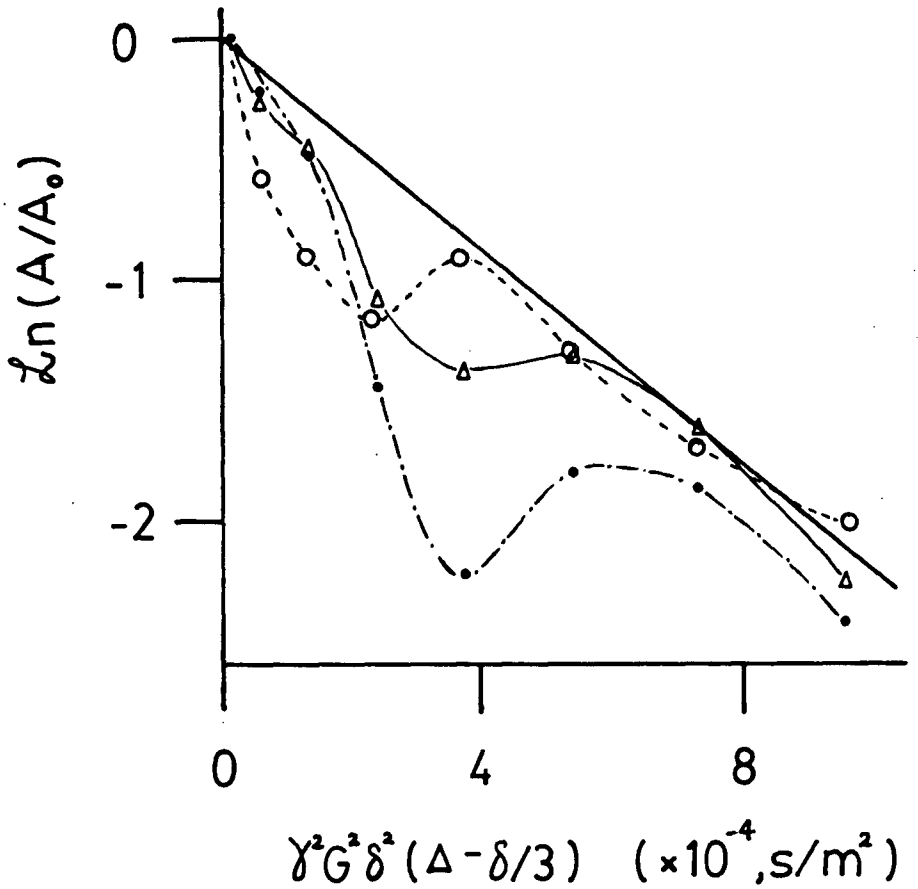

Fig. 2.24 Decay of the spin echo in pulsed gradient diffusion experiments for water with echo time 1.0 s and 1.1 mTm^{-1}, y-gradient pulses of duration 20 ms. Data indicated by (O) and (●) were obtained with the copper shield in place, by measurement of peak heights and integration of the signal respectively. (Δ) indicates data obtained by integration, with the shield removed. The predicted behaviour is shown by the straight line.

all cases the observed decay deviated from the expected behaviour indicating that effects from gradient pulses last for as long as 0.5 s. The reduced relative echo amplitude (A/A_0) obtained with the copper shield in place compared with the shield removed, shows that the presence of the shield enhances the eddy current effects. For measurements with the shield in place, the lower relative values of echo amplitude (A/A_0) from integration compared with peak heights result from significant variation in the phase of the each lineshape. This can be seen from the spin echo FID which does not decay exponentially. Data from another experiment using the gradient coils provided with the magnet are shown in Fig. 2.25. The data were acquired after the application of a pulsed gradient spin echo pulse sequence starting at the echo time, 0.13 s in (A) and 0.63 s in (B). The FID observed at the shorter echo time is 26 times less intense due to improper refocussing of the spins and also shows deviation from the exponential decay which is observed with the longer echo time.

However, by varying the duration and amplitude of gradient pulses, and the echo time, it was possible to obtain echo attenuation data which show more linear behaviour. Data obtained from pulsed gradient spin echo experiments on water, using the x and z gradient coils, are shown in Fig. 2.26. The expected behaviour for water with a diffusion coefficient of 2.19×10^{-9} m^2s^{-1} at 23 °C and gradient magnitudes from linewidths, is also shown.

Fig. 2.25 Spin echo, FID signals from a pulsed gradient diffusion experiment for water using the surface-coil apparatus, with 1.0 mTm^{-1} x-gradient pulses of duration 15 ms, and echo times 0.13 and 0.63 s in (A) and (B) respectively.

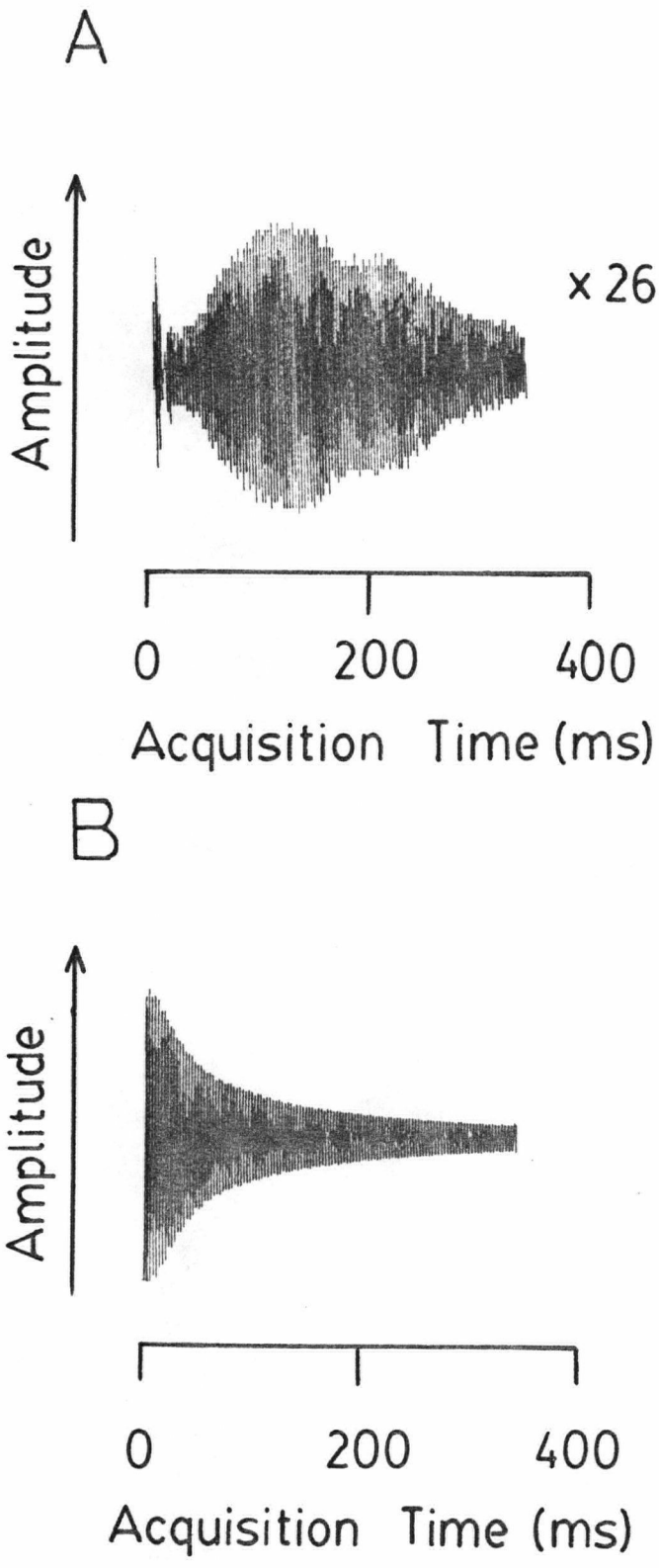
A
Amplitude
x 26
0
200
400
Acquisition Time (ms)
B
Amplitude
0
200
400
Acquisition Time (ms)

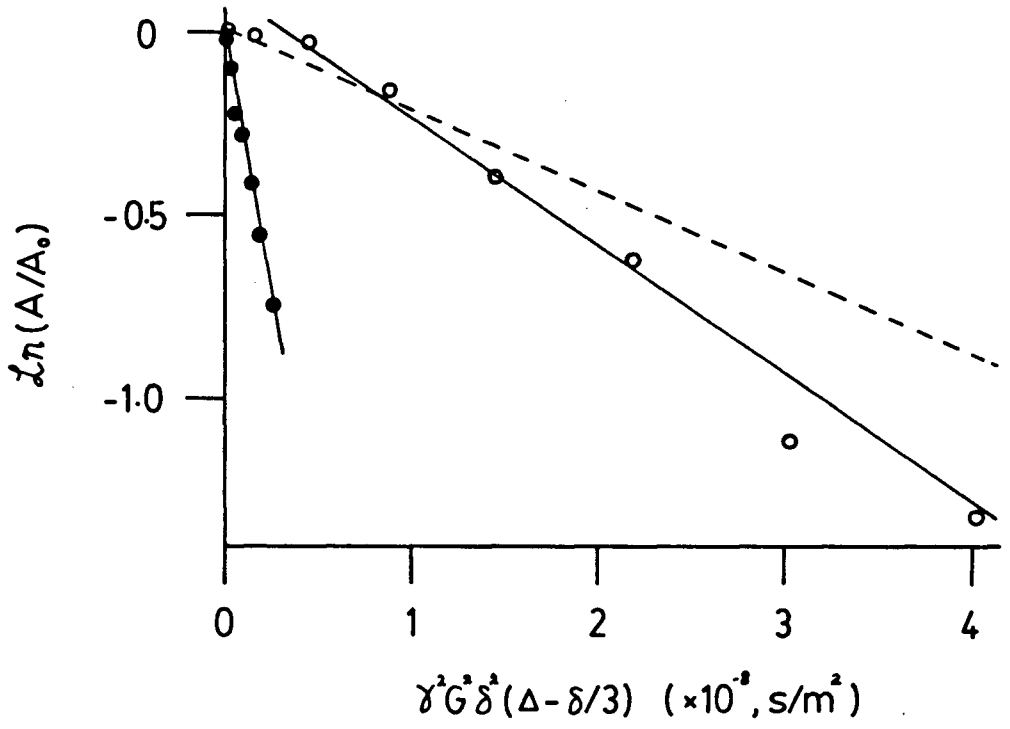

Fig. 2.26 Decay of the spin echo in pulsed gradient diffusion experiments for water, using the surface coil apparatus with x (●) and z (○) gradients. The predicted behaviour is shown by the dashed line. Data for the z-coil were obtained with z-gradient increment 2.1 mTm^{-1}, gradient pulse duration 16 ms and echo time 0.19 s. For the x-coil, the x-gradient increment was 0.65 mTm^{-1}, gradient pulse duration was 12 ms and the echo time 225 ms.

The observed decay is faster than expected, by factors of 1.6 and 12 for the z and x coils respectively. Pulsing of the x-gradient coil also produced a louder acoustical noise than the z coil. The behaviour of the y-coil was similar to that of the x-coil. These observations indicate that x and y gradient pulses induce stronger eddy currents than the z coil. In Fig. 2.27, surface coil diffusion data are shown for a 4:1 mixture of water and ethanol. The values of the diffusion coeficients obtained from the data in Fig. 2.27, 1.26×10^{-9} m^2s^{-1} for water and 8.0×10^{-10} m^2s^{-1} for ethanol are in agreement with the values obtained independently using the high resolution NMR apparatus, 1.19×10^{-8} and 7.04×10^{-10} m^2s^{-1} respectively.

Thus, accurate diffusion measurements could be performed using the pulsed gradient method provided the delay following each gradient pulse was long enough to allow the magnetic field to settle down, but with less precision on the surface coil apparatus than the high resolution apparatus. The precision of surface coil measurements was improved later (chapter III) by extending the measurement over a wider range of echo attenuation.

6. DIFFUSION OF ACRYLONITRILE BY MQ ECHOES

The modified pulsed gradient spin echo sequence of Fig. 2.9 was used to determine the diffusion coefficient of acrylonitrile the proton resonances of which constitute an AMX spin system. By allowing the selective detection of

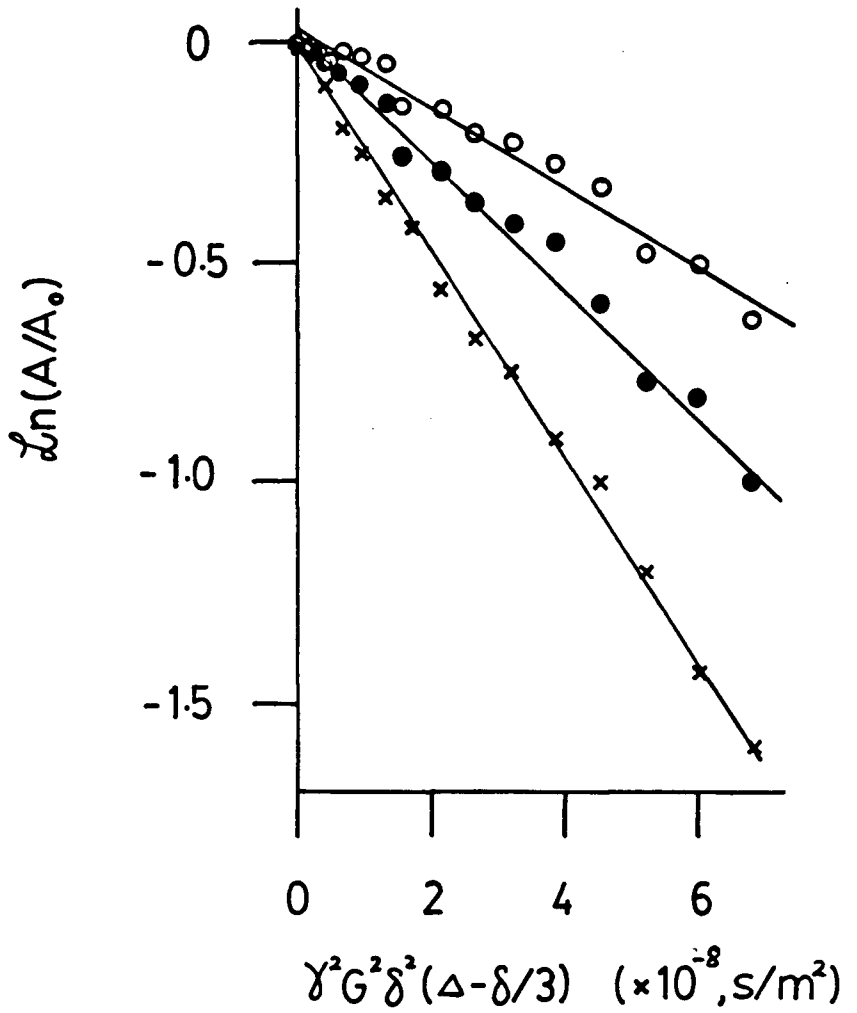

Fig. 2.27 Data for the diffusion of a mixture of water (●) and ethanol (o), 4:1 (v/v), obtained using the pulsed gradient method with effective z-gradient increment of 1.6 mTm^{-1}, gradient pulse duration, 12 ms, and echo time 0.112 s. The data for calibration using water are indicated by "x".

multiple quantum echoes, gradients offer an alternative means for optimizing the excitation parameters in MQ experiments. The variation in the echo amplitude with preparation time arising from single, double and triple quantum coherences, is shown in Fig. 2.28. The oscillatory behaviour is due to the precession of the magnetization components giving rise to the coherence. The preparation time τ, the multiple quantum evolution time t_1, and the delay period T were optimized to give the maximum signal.

Spectra and decay of the spin echoes for the three orders of coherences are shown in Fig. 2.29. The lines were obtained by linear least squares fit to Eq. [2.72]. Figure 2.30 shows the energy level scheme for an AMX system. There should be one triple and six double quantum transitions and all are observed in the spectra. The larger negative slopes for the second and third orders of coherence shows the greater sensitivity to diffusion. The calculated diffusion coefficients are summarized in Table 2.3.

This method will be useful in studies of complex mixtures, and also for the measurement of slower diffusion rates when technical limitations preclude the use of gradients large enough for single quantum measurements. However, the relative inefficiency of conversion of single quantum into higher order coherences, and the relatively long echo times may present some difficulty when the T_2 is short and the system is dilute. In this context, we note the recent publication of double quantum images of human forearm

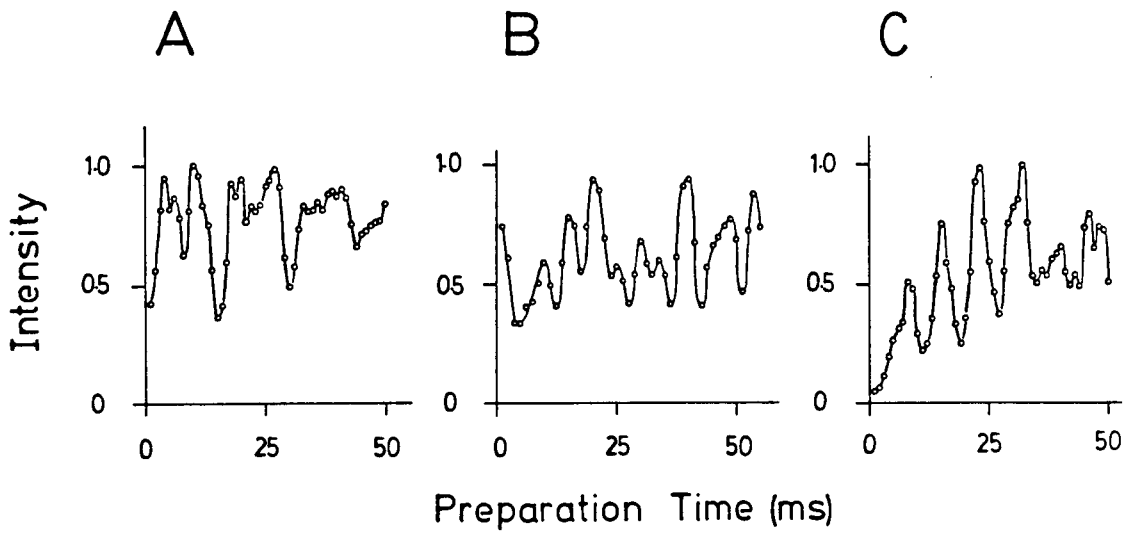

Fig. 2.28 The variation in the amplitude of the single (A), double (B) and triple (C) quantum echoes with preparation time, τ.

Fig. 2.29 Spectra and decay of the spin echoes for single, double and triple quantum coherences of acrylonitrile. The single quantum spectrum was obtained with a normal 90° pulse. The double quantum spectrum is the projection of a two dimensional data set acquired with τ of 30 ms, y-gradient pulse of 3.8 mTm^{-1}, d of 8 ms and T of 300 ms. The incremental MQ evolution time was 0.8 ms and 256 increments were used. The triple quantum spectrum was acquired with τ of 21 ms, y-gradient pulse of 25.2 mTm^{-1}, d of 1 ms and T of 100 ms. The incremental MQ evolution time was 1.67 ms and 256 increments were used. For the diffusion experiments, a δ of 10 ms, Δ of 110 ms with x-gradient increments of 1.61 mTm^{-1}, 0.77 mTm^{-1} and 0.54 mTm^{-1} were used for the single, double and triple quantum echoes respectively. Relaxation delays of 3 s were allowed for equilibration.

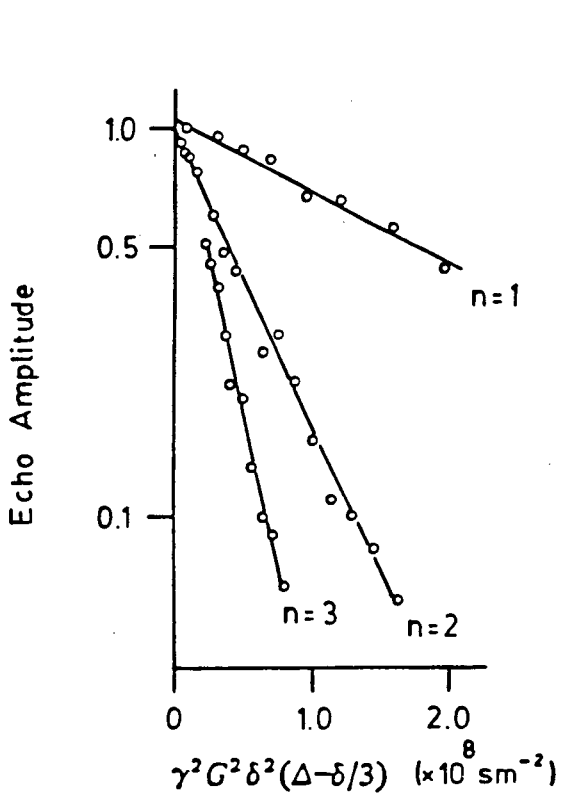
Echo Amplitude
1.0
0.5
0.1
n=1
n=2
n=3
0
1.0
2.0
$\gamma^2G^2\delta^2(\Delta-\delta/3)$ ($\times 10^8$ sm^{-2})

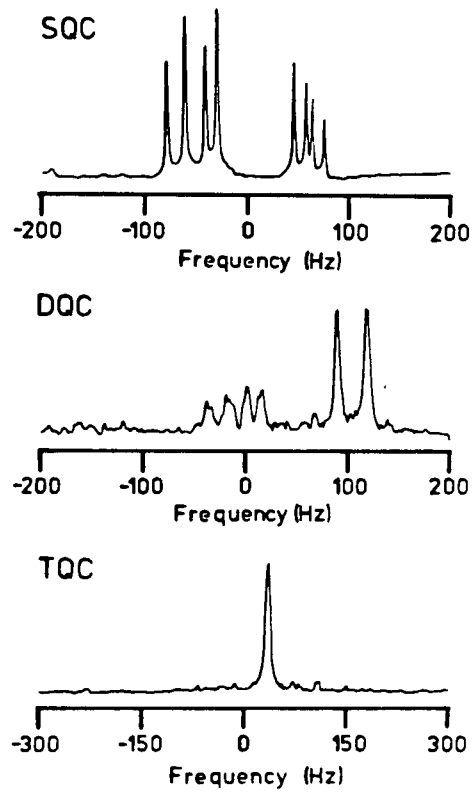
SQC
-200
-100
0
100
200
Frequency (Hz)
DQC
-200
-100
0
100
200
Frequency (Hz)
TQC
-300
-150
0
150
300
Frequency (Hz)

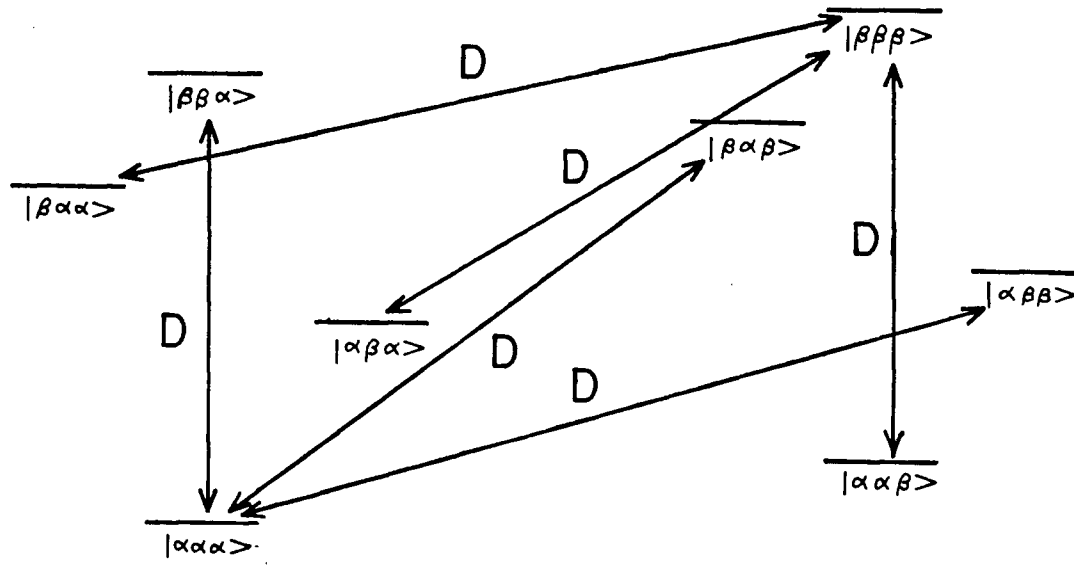

Fig. 2.30 Schematic diagram of the energy levels for an AMX spin system as found in acrylonitrile. The six double quantum transitions are labelled D. Not indicated is one triple quantum transition.

TABLE 2.3

coherence	D ($\times 10^{9}$ $m^2 s^{-1}$)
single	4.2 ± 0.4
double	4.3 ± 0.2
triple	4.1 ± 0.2

Table 2.3 Diffusion coefficient of acrylonitrile from single, double and triple quantum spin echoes. The uncertainties are 98 % confidence intervals from least squares fit to the data in Fig. 2.29.

(90).

7. IMAGING OF GLASS CAPILLARIES CONTAINING WATER AND ACETONE

In Fig. 2.31, two dimensional NMR images of capillary tubes containing water, 1.2 mm i.d. in (A) and 140-220 μm i.d. in (B) are shown, with signal to noise ratio of 15 and 28 respectively. The images correspond to a projection of the proton density along an 11 mm length of the capillaries, corresponding to the extent of the transmitter-receiver coil, into the xy-plane. The ellipsoidal shape of the capillary images in (A) is due to differing field of views along the x and y directions, of 0.47 and 1.01 cm respectively. The transverse resolution in (B) is comparable to that of an image obtained by Eccles and Callaghan *(59)* for capillaries of similar size using a solenoidal rf coil of radius 2.8 mm, but with more demanding experimental parameters including a smaller slice thickness, 1.5 mm, and a spin-spin relaxation time of 5.8 ms. The echo times for these images, 20 ms in Fig. 2.31(A), and 30 ms in Fig. 2.31(B), are much less than the time for which eddy current effects were observed in the pulsed gradient spin echo measurement of Fig. 2.22. In the presence of a large gradient, the weaker gradients produced by eddy currents will have a smaller effect on the shape of the echo than if there were no gradient applied. Also, since the formation of the echo occurs in the middle of the acquisition period, the

Fig. 2.31 Two dimensional images of glass capillary tubes containing water.

(A) Top photograph. NMR image of 1.2 mm i.d. capillary tubes acquired with the pulse sequence shown in Fig 2.2 except that T=0, d=τ and the phase encoding gradient pulse of duration τ was applied immediately after the 90°-pulse instead of the 180°-pulse. The image was acquired with a dwell time of 250 μs, τ of 10 ms, fixed y-gradient of 9.3 mTm^{-1}, x-gradient increment of 0.5 mTm^{-1}, 180° pulse of 28 μs and relaxation delay of 4 s. The field of views were 0.47 and 1.01 cm along x and y respectively.

(B) Bottom photograph. NMR image of capillaries with 140 - 220 μm i.d. and acquired using the pulse sequence in (A). The image was acquired with a dwell time of 167 μs, τ of 15 ms, fixed y-gradient of 38.9 mTm^{-1}, x-gradient increment of 0.6 mTm^{-1}, 180° pulse of 28 μs and relaxation delay of 4 s. The field of views were 0.26 and 0.38 cm along x and y respectively. The 180° pulse length was 28 μs and 4 scans were used for each image.

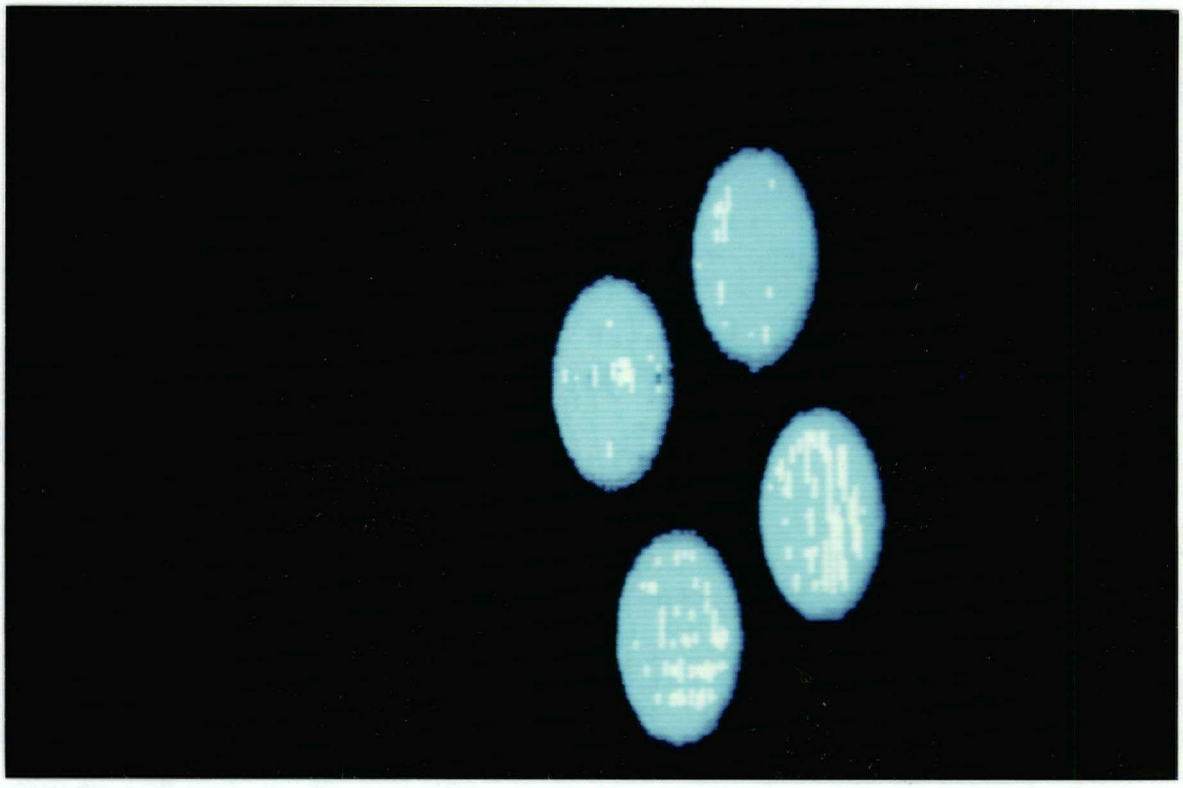

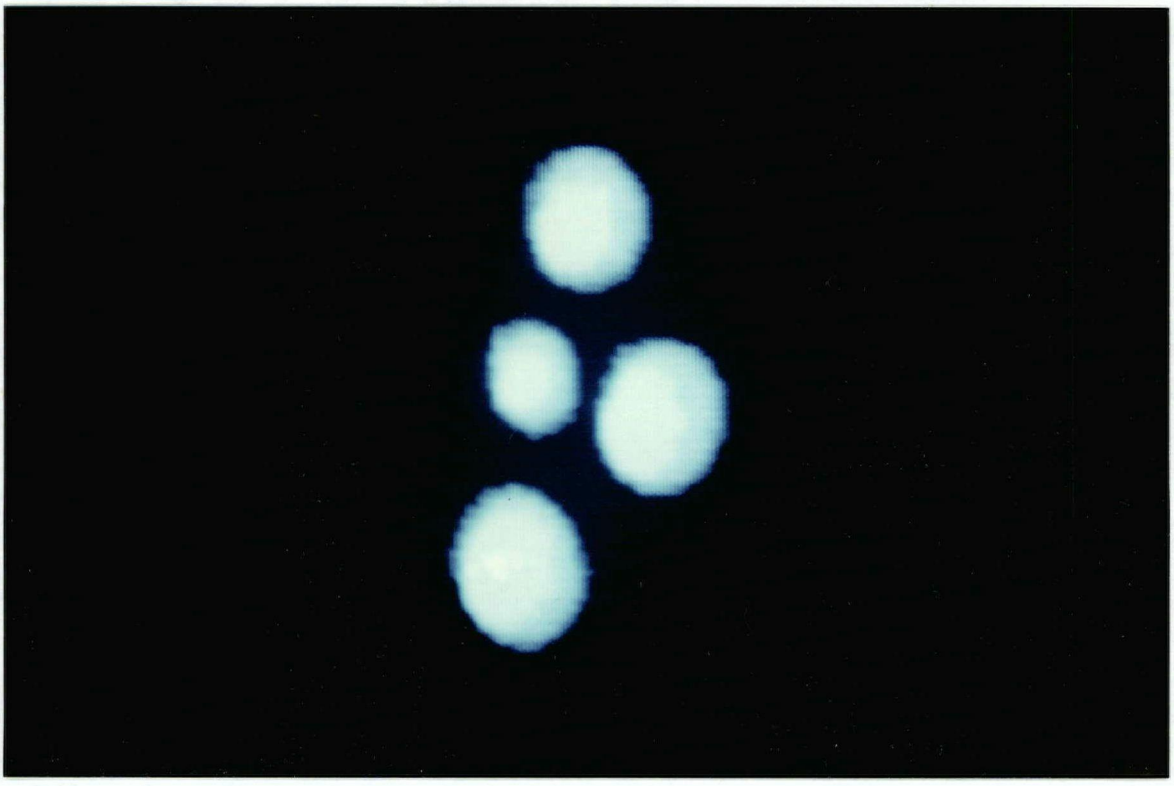

echo may form a little earlier or later than 2τ and the intensity of the signal will not change. Thus the 180° pulse may overlap the tail of the first spin echo gradient pulse. Thus the gradient serves to stabilize the formation of the echo *(13)* and images can be obtained with echo times of 7 ms, as described in chapter IV. In Fig. 2.32, a normal image of 1.2 mm i.d. capillaries, one containing water on the right and the other on the left containing acetone, is shown in (A) and a diffusion contrasted image is shown in (B). The images were acquired using the pulse sequence of Fig. 2.8. The decrease in the intensity of the signals in (B) compared to (A) is greater for acetone which has a larger diffusion coefficient than water. By comparing the intensities in (A) and (B), and taking the diffusion coefficient of water to be 2.19×10^{-9} m^2s^{-1} at 23 °C, the diffusion coefficient of acetone was calculated, using Eq. 2.69, to be 4.10×10^{-9} m^2s^{-1}. This is in agreement with the value obtained in a pulsed gradient diffusion measurement of 4.18×10^{-9} m^2s^{-1} (Fig. 2.33).

Fig. 2.32 (A) NMR image of capillaries containing water (on the right) and acetone (on the left). The image was acquired with the pulse sequence in Fig. 2.8 with a y-gradient pulse of 75.6 mTm^{-1} and and dwell time 50 μs, a x-gradient increment of 1.3 mTm^{-1} with phase encoding time, d, of 3 ms and T of 20 ms. The durations of the 90° and 180° pulses were 13 and 27 μs respectively. The field of view was 0.62 cm along the x and y directions and the z-gradient was not applied. Signal averaging of 4 acquisitions and 128 increments of G_y were used.

(B) Same as in (A) except a z-gradient pulse of 45.8 mTm^{-1} with δ = 5 ms was applied to produce a diffusion contrasted image.

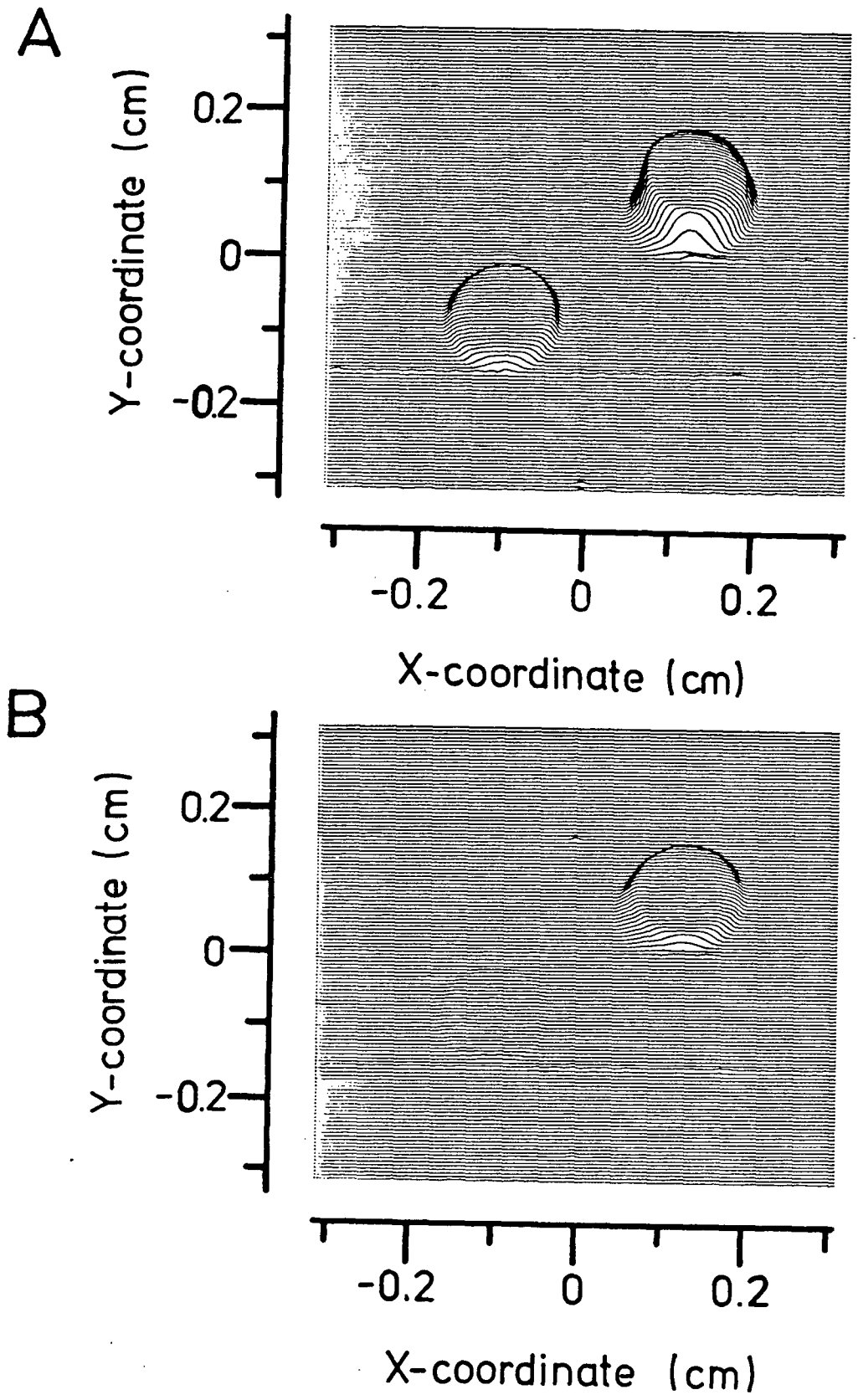
A
Y-coordinate (cm)
0.2
0
-0.2
-0.2
0
0.2
X-coordinate (cm)
B
Y-coordinate (cm)
0.2
0
-0.2
-0.2
0
0.2
X-coordinate (cm)

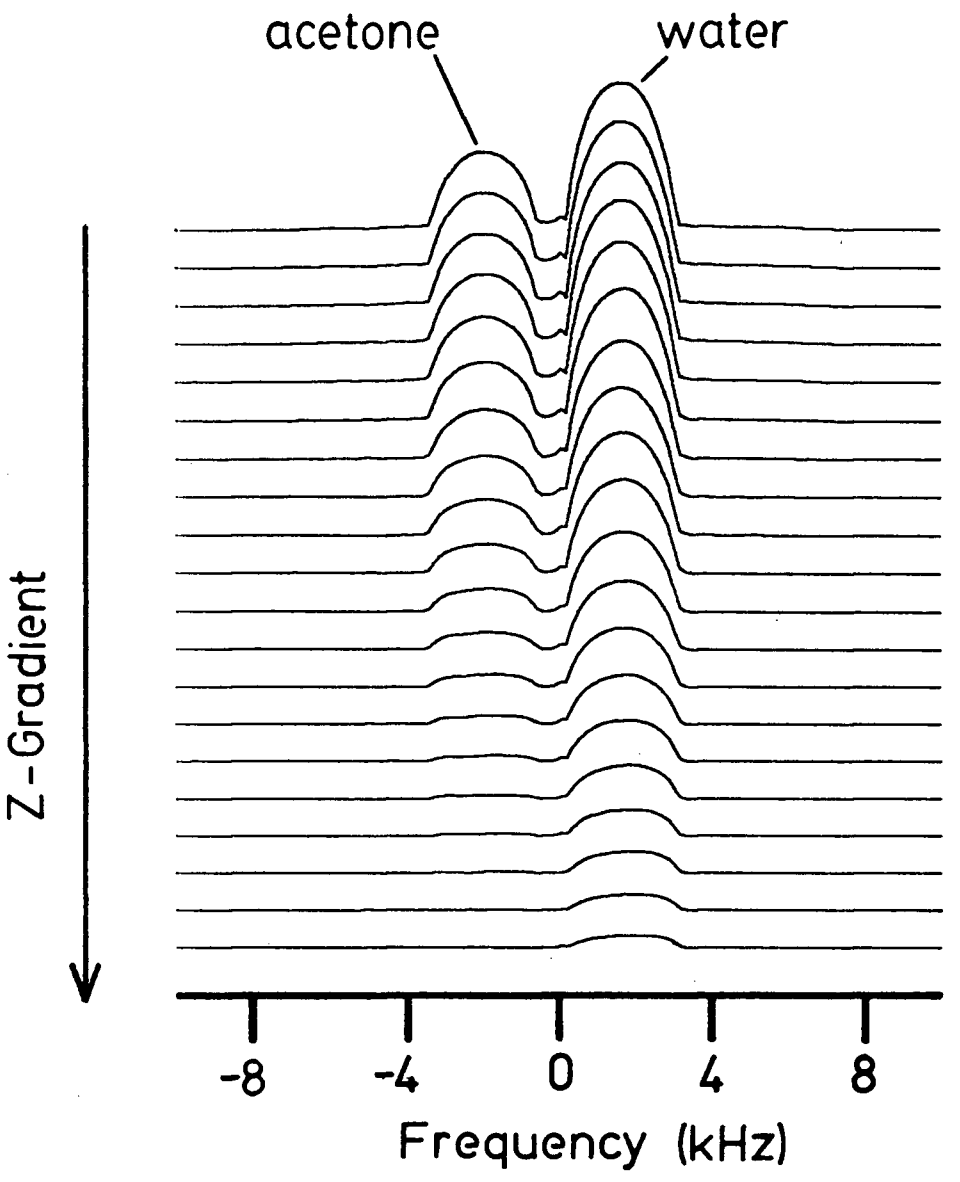

Fig. 2.33 A stacked plot of spectra for capillaries containing water and acetone, acquired with the pulse sequence and parameters of Fig. 2.32 except with the x-gradient turned off and the z-gradient incremented from 3.8 mTm^{-1} to 145 mTm^{-1}.

III. DIFFUSION MEASUREMENT

A. INTRODUCTION

NMR has become an important technique for the study of translational diffusion, with the capability of performing measurements on many different types of samples. The technique possesses a wide dynamic range, from 1 x $10^{-9}m^2s^{-1}$ for liquids to 5 x $10^{-13}m^2s^{-1}$ for dissolved polymers, and is limited only by the magnitude of gradient that can be achieved; in practice gradients may reach 1.5 Tm^{-1}.

The range of application in published work is already quite large, with studies of water in biological systems *(91-94)*, dissolved molecules in colloids *(24, 95-99)*, polymers in solution *(100-103)*, molecules on surfaces *(104)*, hydrogen in metals *(105, 106)* and in aqueous solution *(107-109)*.

Section B of this chapter reports the determination by the pulsed gradient method of the diffusion coefficients of the α- and β- anomers of D-glucose and methyl-D-glucoside in H_2O and in D_2O, and also of dextran, a polysaccharide consisting of 1-6 linked glucose monomeric units, in D_2O. The diffusion coefficient of glucose at infinite dilution was determined by extrapolation from measurements of various concentrations.

Section C describes pulsed gradient spin echo measurements to characterize the motion of water and lipid, *in-vivo*, in human forearm; a surface coil was used to

provide localization of signals.

B. DIFFUSION IN LIQUIDS

The study of diffusion in liquids once (1905-1912) played a role in establishing the molecular theory of matter. Einstein was able to make a connection between the diffusion coefficient obtained by a macroscopic measurement, and the size of suspended particles in a liquid undergoing irregular motion due to collisions with molecules of the liquid

$$D = \frac{kT}{f} \qquad [3.1]$$

where f is the friction coefficient. For a spherical particle of radius r, moving with uniform velocity in a continuous fluid of viscosity η, f_o is given by

$$f_o = 6\pi\eta r \qquad [3.2]$$

From this, Avogadro's number could be determined and was found to be in agreement with the results of studies of other types of phenomena *(110)*.

Today this relation, known as the Stokes-Einstein equation, still provides a very useful means of interpreting diffusion measurements and much effort has been given to establishing a more rigorous connection for the molecules themselves *(111,112)*. The equation is valid strictly in the

limit that the diffusing particle is much larger than the molecules of the surrounding medium. As discussed by Edward, the equation seems to be valid for molecules as small as 5 Å in radius *(113)*. Deviations from the Stokes-Einstein equation are often discussed in terms of the variation of shape of the solute and interactions with the solvent molecules.

In this thesis we apply the pulsed gradient method to measure the diffusion of the α and β anomers of D-glucose and methyl D-glucopyranoside in aqueous solution. Carbohydrates, particularly glucose, occur widely as biological "fuels" and as "building blocks" for polysaccharides such as cellulose. The hydration, conformation and solute interaction of carbohydrates in aqueous solutions have been of some interest. It has been suggested that the number of equatorial hydroxyl groups affects the hydration of sugar molecules *(114)* and that the sugar molecule which has the larger number of equatorial groups has a stronger effect on water structure. In a study of the diffusion of sugars in aqueous solution, a correlation between the limiting values of diffusion coefficients and the number of equatorial hydroxyl groups in the molecule was found *(115)*. By providing an accurate means for determining diffusion coefficients NMR could prove useful in such studies.

1. EXPERIMENTAL

Experiments were performed with the apparatus described previously in section B.1, of chapter II. The gradient magnitudes for all pulsed gradient measurements were determined by calibration with the known diffusion coefficient of water.

2. RESULTS AND DISCUSSION

Fig. 3.1 shows a stacked plot of pulsed gradient spectra for D-glucose, 1.0 M in water. The α and β anomers give rise to distinct peaks at 5.8 and 4.6 PPM respectively. The large signal due to protons of water in the normal ^1H spectrum has been reduced because of chemical exchange with the hydroxyl protons of the glucose molecules. This leads to a shortened spin-spin relaxation time, T_2, so that the water signal can be reduced by using a sufficiently long echo time, 0.38 s in these spectra, to allow relaxation. Thus the diffusion coefficients for each isomer can be determined separately. In Table 3.1, diffusion data for the isomers of D-glucose and methyl D-glycoside are summarized. The observed differences are within the limits of experimental error, estimated to be 2 %. From this we conclude that any differences in shape and hydration between α and β isomers are not sufficient to alter the diffusion coefficient. The diffusion of glucose (1.0 M) in D_2O is slower than in H_2O at the same concentration by 29 %. This reduction can only be partially accounted for by the difference in the viscosity

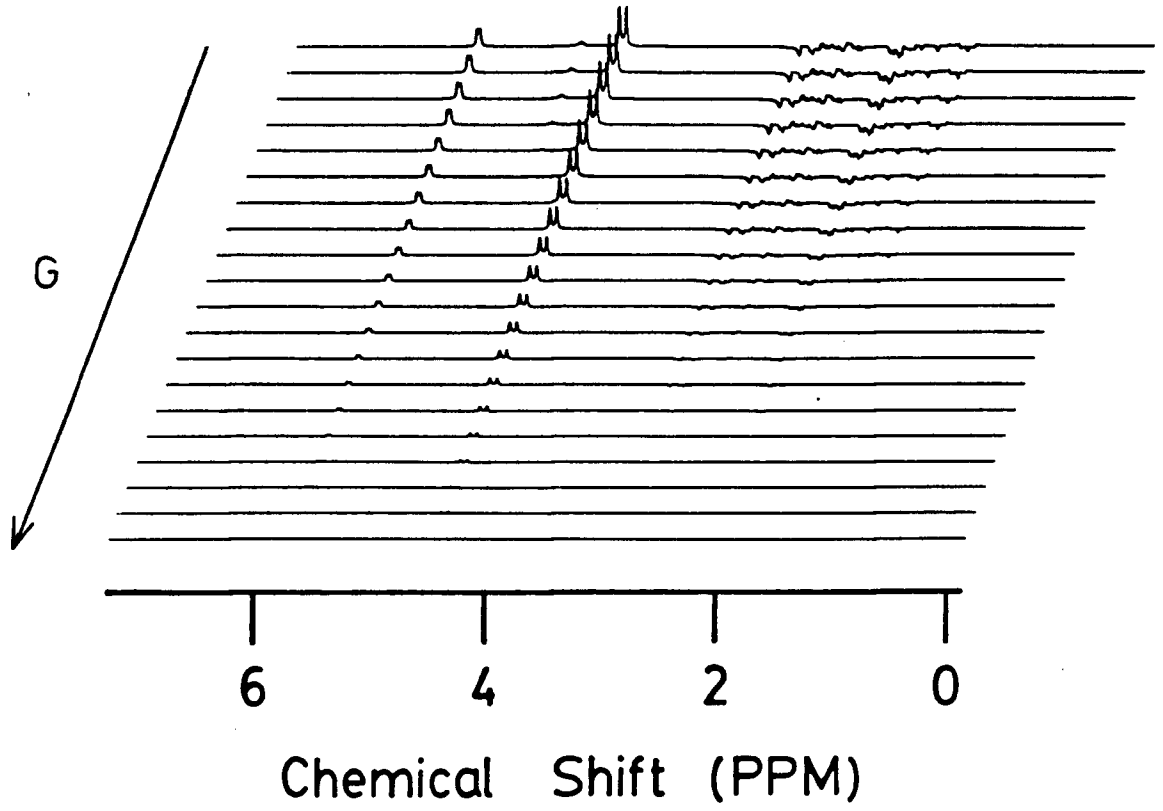

Fig. 3.1 A stacked plot of pulsed gradient ^1H spectra for glucose, 0.5 M in water. The doublets at 4.6 and 5.8 PPM are assigned to the anomeric protons of the β and α anomers of D-glucose respectively.

TABLE 3.1

D-glucose 1.0 M in D_2O	
α-anomer	2.95 $\times 10^{-9}$ $m^2 s^{-1}$
β-anomer	2.97
D-glucose 1.0 M in H_2O	
α-anomer	4.19
β-anomer	4.16
methylglycoside 0.1M in D_2O	
α-anomer	4.84
β-anomer	4.88

Table 3.1 Diffusion coefficients of the α and β anomers of D-glucose and D-methylglycoside.

of D_2O which is 1.23 times greater than that of H_2O at 25° C *(116)*.

In Fig. 3.2, the diffusion coefficient of Dextran (Pharmacia T-10, M_w 9000) 4.3 %(w/v) in D_2O, was determined in an experiment where the gradient was incremented up to 151 mTm^{-1}, to be 6.24 x 10^{-11} m^2s^{-1}, in reasonable agreement with the literature value of 6.3 x 10^{-11} m^2s^{-1} *(102)*.

The diffusion coefficient of glucose in aqueous solutions of various concentrations was measured using the pulsed field gradient method. In Fig. 3.3, extrapolation of the plot of self-diffusion data gives a value for D of 6.70 ± 0.05 x 10^{-10} m^2s^{-1} at infinite dilution. This is in agreement with the literature value of 6.75 x 10^{-10} m^2s^{-1} obtained from the shift of interference fringes *(117)* and of 6.78 x 10^{-10} m^2s^{-1} by the Northrop McBain porous disk technique *(118)*.

The predicted value of 6.17 x 10^{-10} m^2s^{-1} from the Stokes-Einstein equation is smaller than the experimental value. Such deviation is already known and it has been suggested that an empirical correction be made *(113)*.

C. IN-VIVO PROTON SPECTROSCOPY OF HUMAN FOREARM

1. INTRODUCTION

There is interest in the application of NMR to biology and medicine. For example, ^{31}P spectra from human forearm show peaks attributed to ADP, ATP, phosphocreatine and

Fig. 3.2 (A) Stacked plot of pulsed field gradient spectra of dextran (T10), 4.3 % (w/v) in D_2O. The gradient pulses were 15 ms in duration and incremented from 3.98 mTm^{-1} to 151 mTm^{-1} in 19 increments of 7.97 mTm^{-1}. The time between gradient pulses was 115 ms.
(B) The graph of $Ln(A/A_0)$ *vs* $\gamma^2G^2\delta^2(\Delta-\delta/3)$ for spectra in (A). From the slope the diffusion coefficient is 6.24 x 10^{-11} m^2s^{-1}.

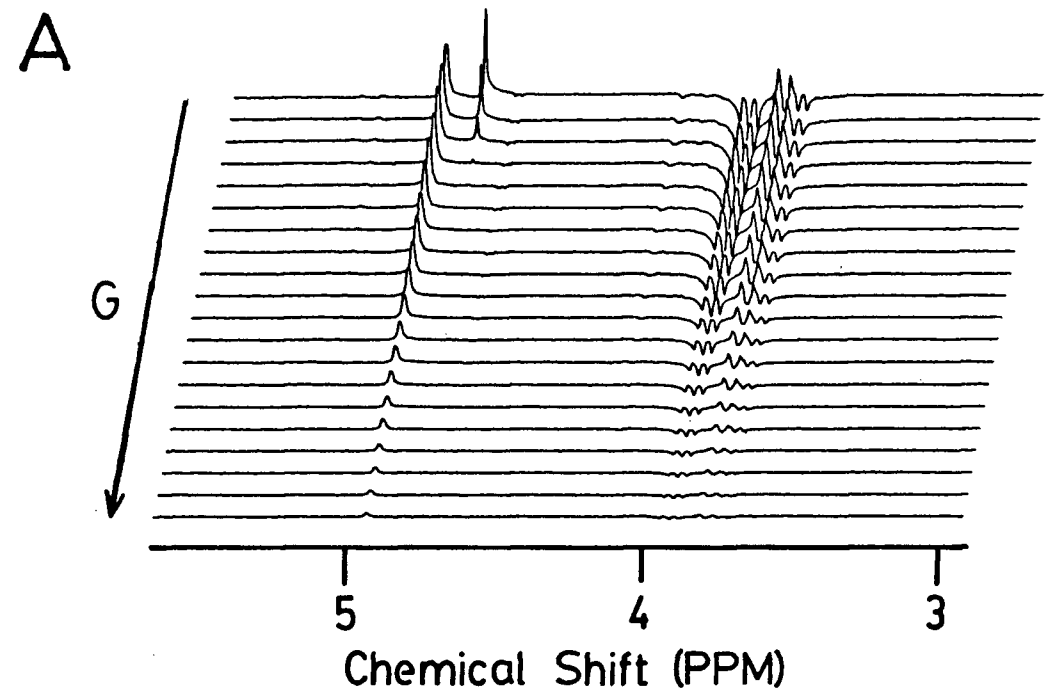
A
G
5
4
3
Chemical Shift (PPM)

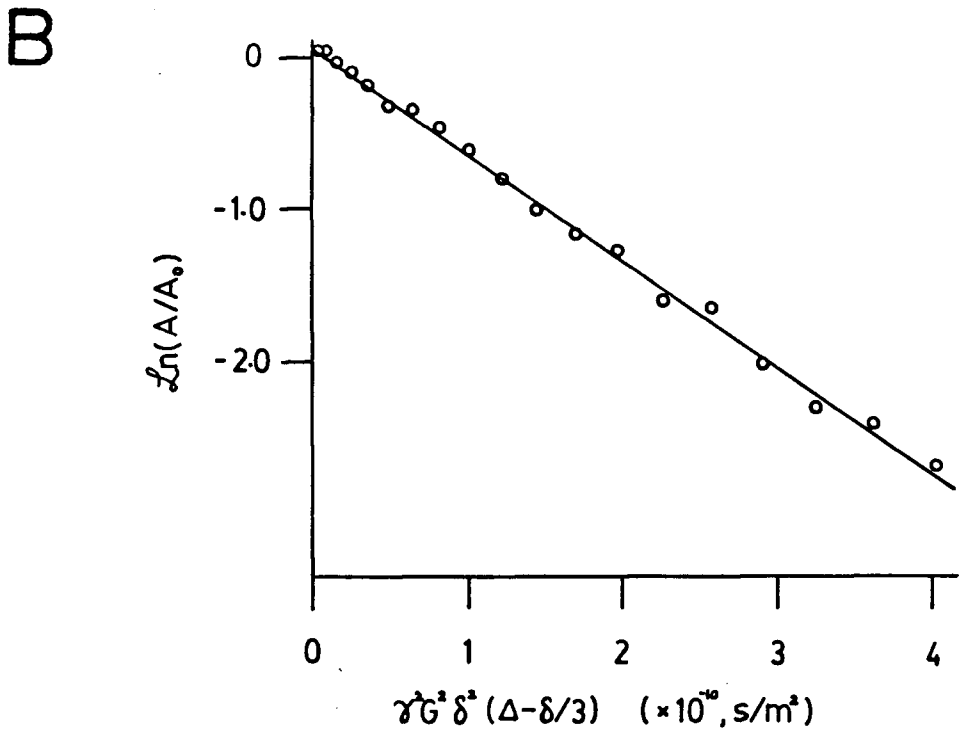
B
0
-1·0
-2·0
ℒn(A/A₀)
0
1
2
3
4
γ²G²δ²(Δ-δ/3) (×10⁻¹⁰, s/m²)

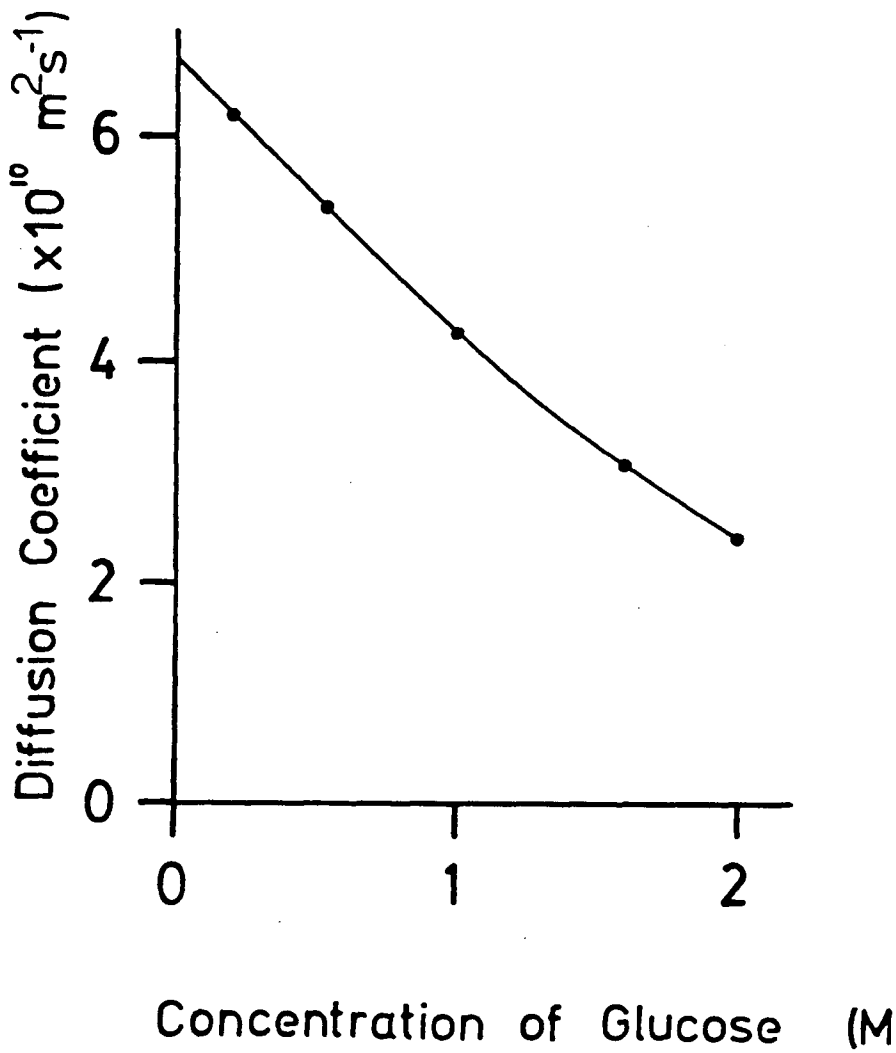

Fig. 3.3 The variation of the diffusion coefficient of D-glucose with concentration in aqueous solution. The room temperature was 23 °C.

inorganic phosphate *(119)*. Changes in the relative intensities reflect differences in the body composition and transport properties of the subject. Considering the heterogeneous nature of the forearm and the metabolic processes carried out within, such spectra are potentially quite complex. The goal of the *in vivo* spectroscopist may be divided into two parts. First, to spatially localize the region from which the signal is obtained and, second, to extract information about the chemical composition and transport properties from the resultant spectra.

Spin echo spectroscopy provides one way of simplifying such spectra. As discussed in chapter II, the contribution to the spin echo signal will be determined by the quantity and also, by the spin-spin relaxation times of the spins. It is possible to discriminate against spins with shorter T_2 values by increasing the echo time and causing the corresponding transverse magnetization to decay. In biological systems, this offers a means for eliminating the large water signal that is observed in normal proton spectra. Recently, ^1H spin echo spectra have been obtained from rat at 360 MHz showing peaks attributed to protons of phosphocreatine, taurine and anserine *(120)*.

In this work we apply the pulsed gradient technique to characterize the translational motion of the water and fat in human forearm muscle. The gradient was applied in the longitudinal (proximodistal) direction along the forearm so that diffusion measurements were effectively one-dimensional

in that direction. A cross-sectional view through the middle of the forearm is shown in Fig. 3.4. The position of the surface coil, placed on the skin, is also shown to scale. The region sampled is probably somewhat more than half muscle, chiefly the flexor carpi radialis and brachio-radialis muscles, and the remainder subcutaneous fat, connective tissue and skin. The greater part of the water in this system should be intracellular, but something like 10% should be flowing blood *(122)*. Muscle fibres, in which about half the water of the system may reside, are a few tens of microns in transverse dimensions, but up to several centimetres long *(123)*.

Water in environments with different chemical composition will have differing degrees of motion due to interactions including chemical exchange with dissolved molecules, and restricted motion at surfaces *(124)*. Spin relaxation times will be correspondingly affected. For a system consisting of n exchanging phases *(125)*, if P_i denotes the fraction of water present in the i^{th} phase, T_i denotes a general relaxation time (T_1 or T_2), the magnetization M(t) for the slow exchange case (T_i<< lifetime in the i^{th} phase) is given by

$$M(t) = \sum_{i=1}^{n} P_i \, e^{-t/T_i} . \qquad [3.3]$$

The magnetization M(t) is taken to be (M_0 - M_z) for longitudinal and $M_{xy,0}$ for transverse components. Each phase

Fig. 3.4 Cross-section through the middle of the forearm (A) and the superficial muscles on the front of the forearm (B) (from Grant's Atlas of Anatomy *(121)*). The approximate location of the 2.7 cm diameter surface coil is shown.

relaxes independently with time constant T_i. Such a situation would pertain, for instance, in the presence of compartmentalization, where the water is physically barred from diffusion between the various regions.

For the case of rapid exchange (T_i >> lifetime in the i^{th} phase),

$$M(t) = e^{-t\sum_{i=1}^{n} P_i/T_i}. \qquad [3.4]$$

In this regime, the whole system relaxes with a single characteristic time T given by

$$1/T = \sum_{i=1}^{n} P_i/T_i. \qquad [3.5]$$

In the forearm, with different types of tissue, compartmentalization is expected to lead to multiexponential relaxation rates. Previous studies of biological tissue have shown that spin-spin relaxation rates of water indeed tend to be multiexponential and are about fifty times faster than spin lattice relaxation rates *(126, 127)*.

Lipids[10] occur in the body in a wide variety of forms. The triacylglycerols (triglycerides, (I)) serve primarily as efficient biological "fuels". The phospholipids (II) are

---

[10] Lipids are constituents of animal or plant tissue that are insoluble in water but can be dissolved and extracted by organic solvents.

essential components of membranes.

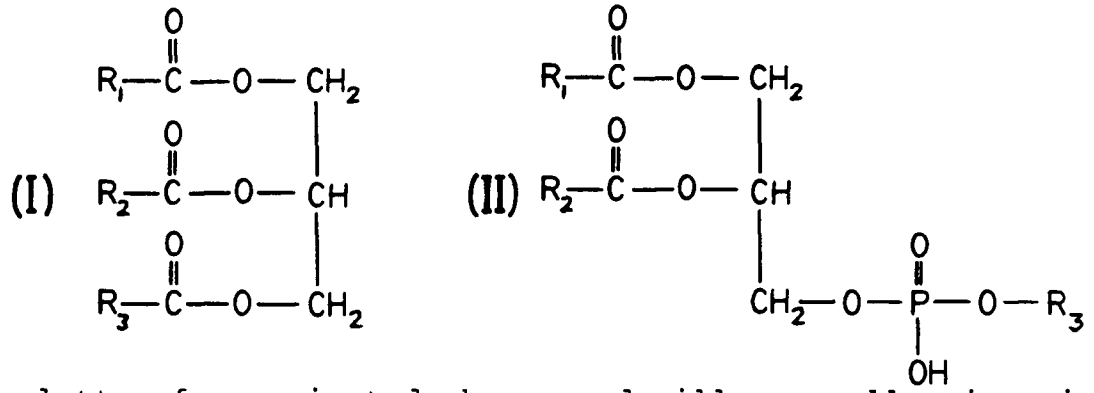

The latter form oriented phases and will generally give rise to broad NMR lines due to only partial averaging of the dipole-dipole interaction and chemical shift anisotropy *(128)*. Consequently, when measured under the conditions of high resolution NMR spectroscopy (as distinct from solid state NMR), the associated signal will decay rapidly, within a few microseconds and will not be detected. In mammals, the major site of storage of triacylglycerols is the cytoplasm of adipose cells (adipocytes) which occur in muscle, mammary glands, the abdominal cavity, and under the skin.

In many cells these insoluble triglycerides coalesce in the cytosol[11] to form large, anhydrous droplets from 0.2 to 5 μm in diameter *(129)*. In adipocytes, the cells specialized for fat storage, these droplets can be as large as 80 μm in diameter, occupying virtually the entire cytosol.

---

[11] All intermediary metabolism takes place in the cytoplasm, most of it in the cytosol. The cytosol generally represents about 55% of the total cell volume and contains thousands of enzymes that catalyze the reactions of glycolysis and gluconeogenesis, as well as the biosynthesis of sugars, fatty acids, nucleotides and amino acids *(129)*.

The release of triacylglycerols from adipose tissue involves their hydrolysis by lipases. The free fatty acids produced this way are transferred to the blood, where they are reversibly bound by the protein serum albumin and transported to various tissues. Immediately after a meal, normal human plasma may contain about a milligram per milliliter of triacylglycerol fat. Whole plasma contains about 7-8 % protein, 55% of which is serum albumin (MW 69000) *(130)*.

THE EFFECT OF BLOOD FLOW

Blood flows from the heart through the aorta into an increasingly more divided system of arteries, arterioles and finally a network of capillaries. If all vessels were put side by side, their total cross sectional area would range from 2.5 cm^2 for the aorta to 2500 cm^2 for the capillaries (Table 3.2 *(131)*). The velocity of blood flow in each segment of the circulation is inversely proportional to its cross-sectional area. Thus, under resting conditions, the velocity averages 33 cm per second in the aorta and about 0.3 mm per second in the capillaries. However, since the capillaries have a typical length of only 0.3 mm to 1 mm, each segment of flowing blood remains in the capillaries for only 1 to 3 seconds. The capillaries are less than 10 μm in diameter and are randomly oriented. Only a few percent of the blood is in the small capillaries at any instant, but about 2/3 of it is in the venous system, in which flow is

TABLE 3.2

	cm^2
Aorta	2.5
Small arteries	20
Arterioles	40
Capillaries	2500
Venules	250
Small veins	80
Venae cavae	8

Table 3.2 Cross-sectional areas of blood vessels *(131)*.

slow, and pooling and back-eddies common, so that velocities of 3 mms^{-1} may exist in a large fraction of the blood supply. Sufficiently randomized in direction, this flow could mimic diffusion on the time scale of a spin-echo experiment.

2. EXPERIMENTAL

Experiments were done using the apparatus previously described in chapter II, B.2. NMR signals were measured using a surface coil which was placed on the skin and echo times were made long enough so that effects from slow gradient response were minimized. The diffusion coefficients were determined from the variation of peak heights of lines in pulsed gradient spectra and gradient magnitudes were determined by calibration using the known value for the diffusion coefficient of water. All experiments were performed at ambient temperature, 23-26 °C.

3. RESULTS AND DISCUSSION

Normal proton spectroscopy of the right forearms of two subjects[12] M & F, in the region of the flexor carpi radialis and brachi-radialis muscles are shown in Fig. 3.5. The increased relative intensity of the lipid peak in Fig. 3.5(B) reflects an obvious difference in the body composition of the two subjects; the lipid peaks at 1.7 and 5.3 PPM in Fig. 3.5(B) are also seen in Hahn spin echo

---

[12]subject M was a male (1.6 m, 52 kg) whereas F was a female (1.5 m, 47 kg).

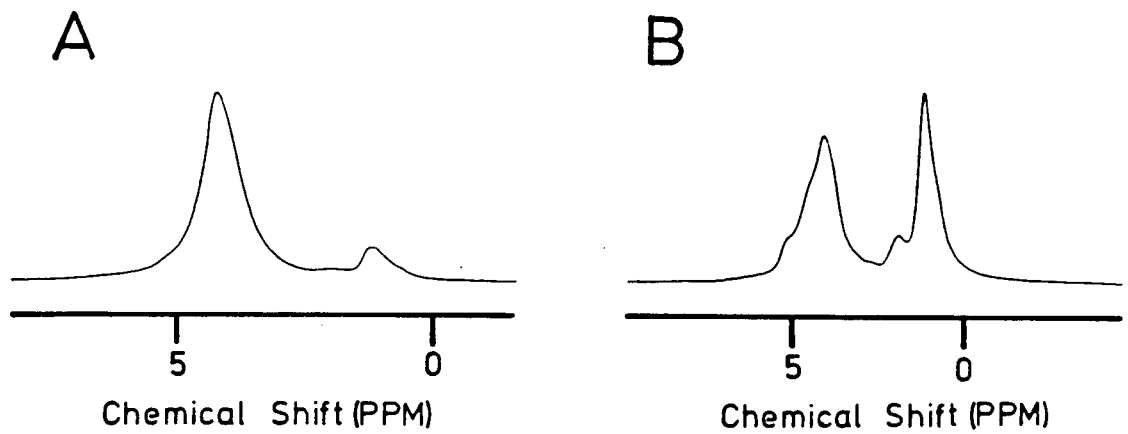

Fig. 3.5 Normal proton spectra of the right forearms of two subjects (M: male, 1.6 m, 52 kg; F: female, 1.5 m, 47 kg).

spectra for subject M. The spin echo spectra in Fig. 3.6(B) were measured with echo times ranging from 400 to 600 ms. Changes in the relative intensities clearly show that the spin-spin relaxation times of the lipid peaks at 1.3 and 1.7 PPM are different. The spectra also show that the water relaxes much more slowly. Further confirmation of this comes from comparison with the large relative intensity of the lipid peaks in the pulsed gradient spectra in Fig. 3.6(C) with shorter spin echo time, 224 ms. The spin-spin relaxation times, for the spectra in Fig. 3.6(B), were determined by linear least squares fit to the graph of $Ln(A/A_0)$ *vs* 2τ (Fig. 3.7) and are summarized in Table 3.3. The shorter values of T_2 ,86 & 88 ms, for the lipid protons compared to that of Williams *et al. (120)* (292 ms) by a CPMG pulse sequence is probably due to diffusion in the inhomogeneous field. However, longer relaxation times for the latter experiment are also expected because the spectral density at 360 MHz is likely to be smaller than at 80 MHz.

The T_2 value for the water, 740ms, is long compared with that of Williams *et al. (120)* (28.8 ms, by the CPMG method). The latter value will be characteristic of the major component, intracellular water, since the echo times ranged from 2.7 to 100 ms. Similar T_2 values for intracellular water have been obtained from studies on giant barnacle muscle *(126,127)*. For echo times of 200 ms the signal from the intracellular component will be attenuated

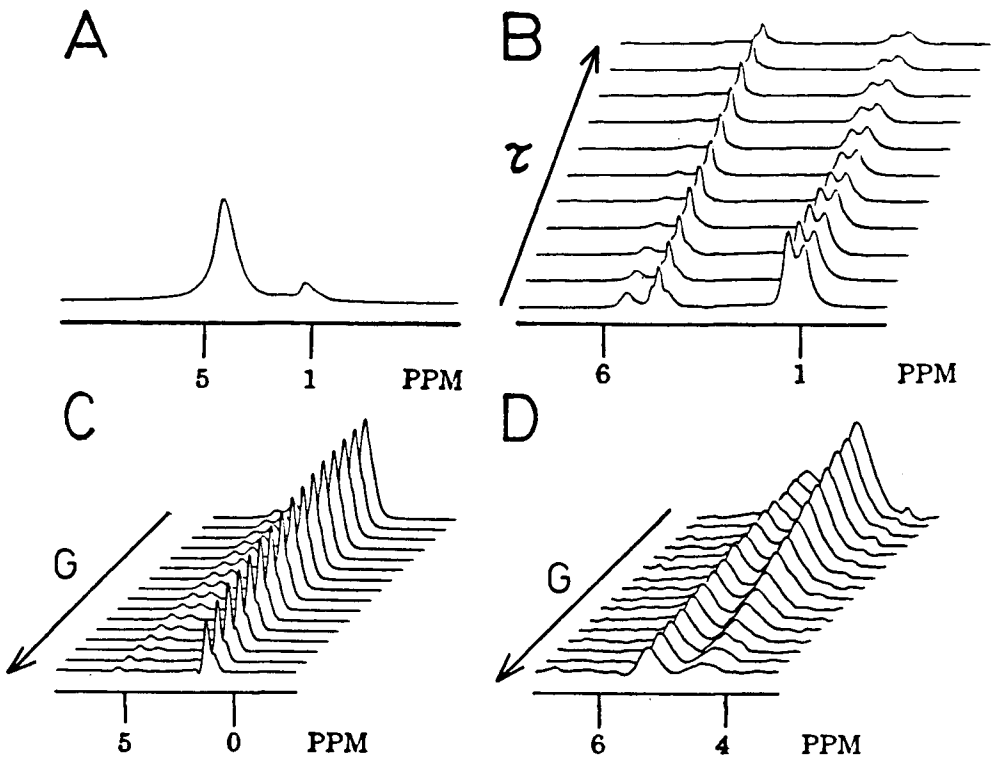

Fig. 3.6 Normal proton spectra and a stacked plot of Hahn echo spectra for subject M in (A) and (B) respectively. Pulsed gradient spin echo spectra with echo time of 224 ms in (C) with an enlarged view of the 4-6 PPM region in (D).

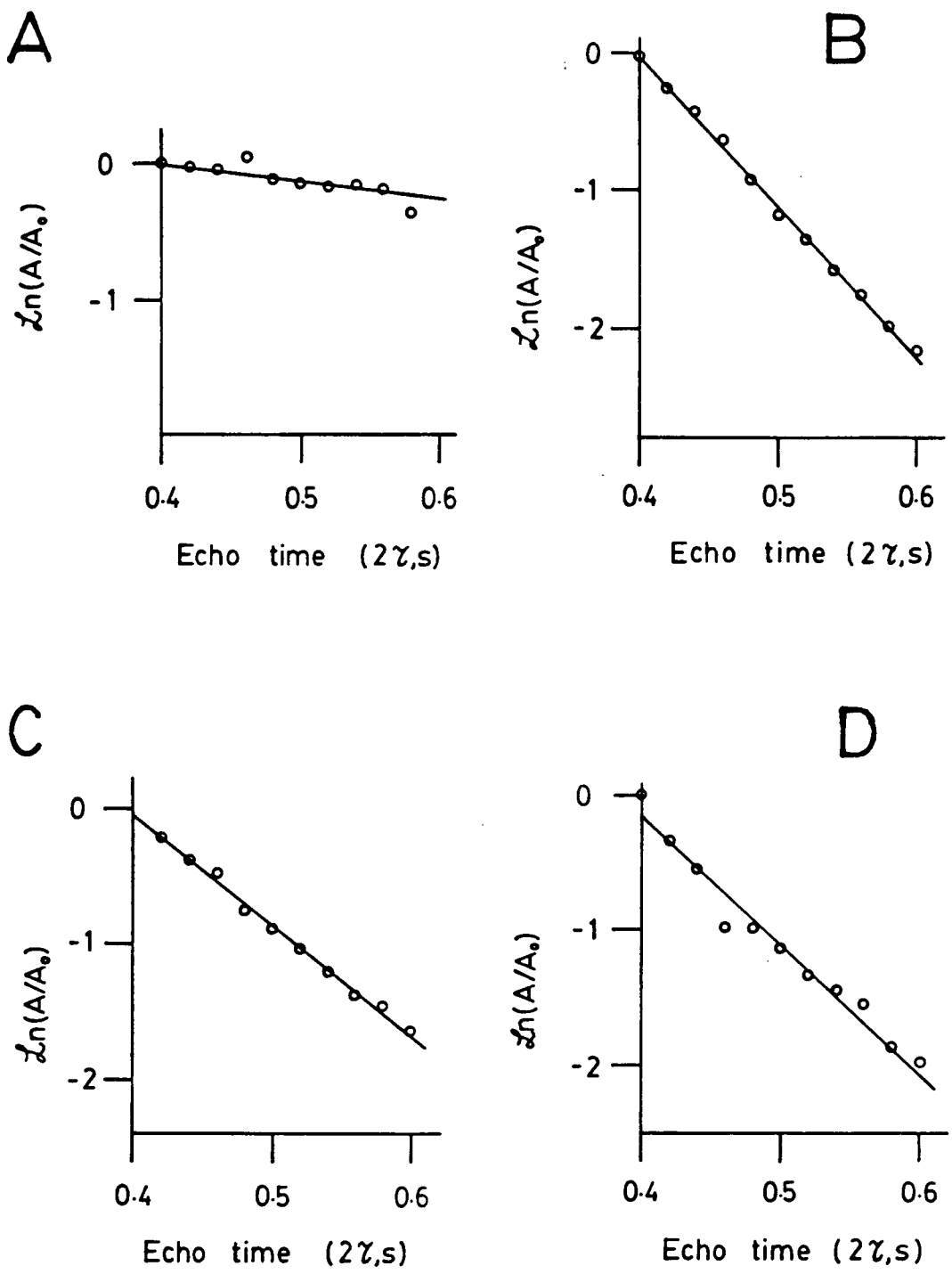

Fig. 3.7 Plot of $Ln(A/A_0)$ *vs* τ for water (A) and lipid (B-D) from Hahn echo spectra of subject M.

TABLE 3.3

EXPERIMENTAL VALUES

	Chemical Shift (PPM)	T_2 (ms)	D/D_O*
Lipid	1.3	120	0.20, 0.23, 0.26, 0.17
Lipid	1.7	88	—
Water	4.8	740	0.70, 0.64, —, 1.11
Unsaturated lipid	5.3	86	0.22, 0.21, 0.21, 0.17

LITERATURE VALUES

Assignment	T_2 (ms)	
Intracellular water	35	Foster et al.
	28.8	Williams et al.
Extracellular water	400	Foster et al.
Fat	292	Williams et al.

Table 3.3 Chemical shifts, spin-spin (T_2) relaxation times and relative diffusion rates (D/D_0) for water and fat *in-vivo*; $D_0 = 3.05 \times 10^{-9}$ $m^2 s^{-1}$.

*: The data (a,b,c,d) correspond to experiments with echo times of 224 ms for a,b and c, and 400 ms for d.

by about three orders of magnitude. Thus the signal at 4.8 PPM in Fig. 3.6(B) is probably due to extracellular water. A previous study of the spin-spin relaxation of water in barnacle muscle gave a component with a T_2 of 400 ms which was also attributed to extracellular water (Foster *et al.*, *(127)*).

Further evidence to support the assignment was obtained from diffusion measurements. Pulsed field gradient spin echo spectra were measured keeping Δ, the separation between the 90° and 180° pulses fixed and incrementing the gradient. Spectra obtained from subject M are shown in Fig. 3.6(C) and an enlarged view of the 4-6 PPM region is shown in Fig. 3.6(D). The increased relative intensity of the lipid signal is due to the shorter T_2 of the majority of the water. The decrease in the amplitude of the signals as the gradient is increased is due to the effect of diffusion. The water signal at 4.5 PPM decays more quickly and reflects the higher mobility. Graphs showing the decay of the water and fat signals for spin echo times of 224 ms and 400 ms are shown in Fig. 3.8. The straight lines are the best fit by linear least squares analysis. Except for the first few points in Fig. 3.8(C), for water at echo time 400 ms, all of the data are nearly on the lines. There is no apparent effect of bulk flow which would cause oscillatory behaviour. All of the motions are diffusive.

Diffusion coefficients from repetitions of these experiments, three with echo time 224 ms and one at 400 ms,

Fig. 3.8 (A) Decay of the water signal from pulsed gradient spin echo spectra acquired with gradient pulse duration, δ, of 12 ms and echo time 0.224 s. Data are shown for two separate experiments (O and x) and the effective z-gradient increment is 1.84 mTm^{-1}.
(B) Decay of water (x) and lipid (O) signals from *in-vivo*, pulsed gradient spin echo spectra of human forearm acquired with the same experimental parameters as in (A).
(C) Decay of water (●) and lipid (O——O) signals from pulsed gradient spin echo spectra of human forearm acquired with gradient pulse duration, δ, of 20 ms and echo time 0.4 s. Calibration data (O---O) using water gave an effective gradient increment of 0.53 mTm^{-1}.

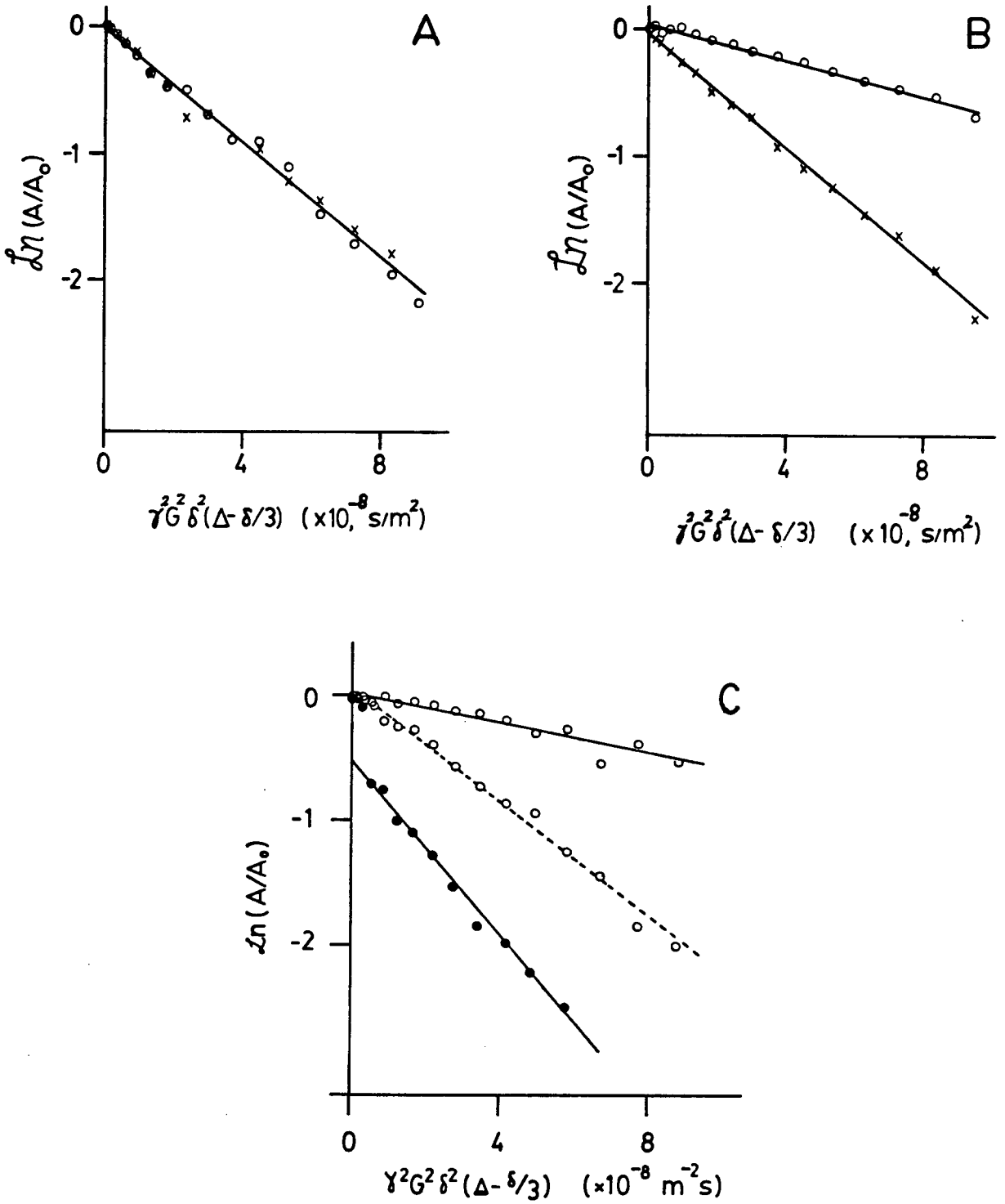
A
B
C
0
-1
-2
4
8
ln (A/A₀)
γ²G²δ²(Δ- δ/3) (x10⁻⁸ s/m²)
γ²G²δ²(Δ- δ/3) (×10⁻⁸ m⁻²s)

are summarized in Table 3.3. One of the measurements with echo time 224 ms was of subject F and the remainder were of subject M. The measurements at echo time 224 ms gave diffusion coefficients of about 2.2 x 10^{-9} m^2s^{-1} which is smaller than that of normal water at 37 °C, 3.05 X 10^{-9} m^2s^{-1} *(11)*, by a factor of 0.7. This reduction may be compared with that observed for the diffusion of intracellular water in excised frog muscle, 0.6-0.66 *(132-134)*, and in barnacle muscle 0.5-0.6 *(92)*. From the measurement with echo time, 400 ms, a larger diffusion coefficient for water was obtained, 3.5 x 10^{-9} m^2s^{-1}. The increase in diffusion rate is an indication that there may be randomized flow. From the data in Table 3.3, and using Eq. [2.81], the contribution due to normal diffusion is 5.5 x 10^{-10} m^2s^{-1} and to randomized flow is 0.14 mms^{-1}. The estimated value for the root-mean-squared velocity is less than would be expected for blood flow in capillaries, 0.33 mms^{-1}, but would indicate that the major part of the motion of the extracellular water is due to randomized flow. The contribution due to normal diffusion corresponds to a reduction of 0.2 compared to the diffusion of normal water and suggests that at echo times of 0.1-0.2 s, the extracellular water is undergoing restricted diffusion.

The lipids giving rise to NMR signals are intracellular for the following reasons. The quantity of fat in the blood plasma is small (Table 3.4, *(135,136)*), and since the T_2 of

TABLE 3.4

	Water content	ref.
Skeletal muscle	79.2	K. Diem 1970
Epidermis	64.5	K. Diem 1970
Blood plasma	93	P.L. Altman 1973

Table 3.4 Normal tissue water content in adult humans expressed as a percentage per kilo of fat-free tissue from Diem *(135)* and Altman *(136)*.

the lipids is less than that of extracellular water, any contribution from extracellular fat would not be detectable under the conditions of these experiments. Furthermore if the signals were due to fat in the blood plasma, the effect of randomized flow should cause the diffusivity to increase as the echo time increased. Instead the diffusivity decreased indicating restricted motion.

The diffusion coefficient of the lipids can be estimated using the Stokes-Einstein equation. Taking as a typical triglyceride, the ester with three oleic acid molecules attached, the molecular volume is estimated using van der Waals atomic and group increments *(113)*. The value obtained is 987 A^3 with a corresponding van der Waals radius of 9.05 A. Since the fat in the cytoplasm forms liquid globules, the viscosity of olive oil at 30 °C, 50 cp *(137)*, is used as a rough estimate and the calculated diffusion coefficient is 5×10^{-12} m^2s^{-1}. The observed value of 6.57×10^{-10} m^2s^{-1} is 100 times larger. The increased diffusivity might be attributable to the effects of cytoplasmic streaming entraining the fat globules. This would produce random motion on the time scale of the NMR experiment. The slight decrease in diffusivity as the echo time is increased, contrary to the prediction of Eq. 3.16 is probably due to restricted motion inside the cell. The root-mean-squared displacement for the observed diffusion coefficient is 17 μm and 23 μm for echo times of 0.224 and 0.4 s respectively. These distances are of the same order of

the size of the globules that would be found in adipocytes. The effective root-mean-squared velocity is 66 μms^{-1}. Measurements of cytoplasmic streaming in plants have given values of about 70 μms^{-1} *(137)* in a few cases, but streaming in animal cells is rarely faster than 5 μms^{-1}. Further experiments will be required to confirm these observations.

IV. NMR IMAGING

A. INTRODUCTION

Two- and three- dimensional proton magnetic resonance imaging is coming into increasing use in medical diagnosis *(1-4)* of soft tissue defects in man. Spatial resolution from a whole body scanner, quoted two years ago *(3)* as at best 5 mm^3 on a volume basis, today can sometimes be better than 1 mm in-plane in a slice thickness about 2 mm. For biological studies of smaller samples, there is considerable current interest in improving spatial resolution, say to 0.1 mm for physiological studies such as water transport in plants, or to 10 μm or better for a wider range of applications in developmental biology. Recent images *(59,139)* of biological samples show identifiable substructures of 0.1 - 0.2 mm dimensions. Here, we use the term "spatial resolution" to mean this quantity. Numbers from 10 to 20 μm in *(59,139)* are pixel sizes, showing that the display capability of the computer system exceeds the spatial resolution of the data, as it should. The mapping of the distribution is achieved by applying gradients as described in chapter II. While T_1 and T_2 contrasted imaging can provide substantial information, and much effort has been directed at manipulating these parameters *(1-4)*, other parameters such as chemical shift and diffusion are also potentially useful.

In this chapter, the previously described apparatus and techniques for imaging are used to map proton distributions in pupae of the Douglas fir cone moth, *Barbara colfaxiana* (section B) and in reproductive caps of the marine alga, *Acetabularia mediterranea* (section C).

B. *BARBARA COLFAXIANA*

1. INTRODUCTION

Although NMR can be used to study any insect species, pharate adults of the Douglas-fir cone moth, *Barbara colfaxiana* (Lepidoptera: Olethreutidae), are particularly suited to proton NMR (^{1}H-NMR) studies because they have more than two separate compartments containing aqueous fluids (haemolymph and moulting fluids) as well as lipid reserves *(140)*[13]. The application of ^{1}H-NMR imaging to the study of these animals has allowed the *in-vivo* observation of these discrete fluid bodies for the first time. In the course of these experiments it was found that *B. colfaxiana* pharate adults responded differently to the two opposing principal orientations with respect to gravity, hereafter referred to as "head-up" and "head-down".

---

[13] The term "pharate" adult is used to describe the stage of insect development in which the developing adult is within the pupal cuticle and separated from it by moulting fluid. Used interchangeably in this paper are the terms "pharate adult", "pupae", "insect" and "animal", they are used to describe this same developmental stage. "Pupae" is used most often as this term is the most descriptive of the external characteristics.

Barbara colfaxiana damages cones and seeds of Douglas-fir, *Pseudotsuga menziesii* (Mirb.), Franco, in both natural stands and seed orchards. This insect exhibits a diapause that spans one, two, or more winters *(141-144)*. The diapause occurs in the pharate adult stage, but the external characteristics are those of a pupa *(140)*. Insects used in this study were contained inside Douglas-fir cones collected near Keremeos, British Columbia. They were kindly provided by Dr. John F. Manville of the Pacific Forestry Centre (Canadian Forestry Service, Victoria, B.C.)

2. EXPERIMENTAL

Cones were stored in unheated sheds until both light (will not eclose next spring) and dark (will emerge next spring) pupae were extracted from their cones and examined during the months of November, 1984 and April, 1985. All experiments were performed on individual pupae. The preferred natural orientation of these pupae inside Douglas-fir cones is head uppermost with the body at +15 to 20 degrees from horizontal (J. Manville, personal communication). ^{1}H-NMR spectra and NMR images of individual pupae were run using the same 6.3 T magnet and imaging hardware as described in Chapter 2. The 90°-pulse was 18 μs and eight transients were used. Experiments were done at ambient temperature (21-24 °C). The pupae were maintained in a vertical position inside a 5 mm NMR tube using a 3 mm i.d. glass tube. The pupae were held at the center of the rf coil

by small pieces of tissue paper placed in the bottom of the NMR tube. The pupae were examined in both the head-up (H/U) and the head-down (H/D) orientations. Proton distribution maps were obtained using the pulse sequence shown in Fig. 2.5. All *in vivo* NMR studies were conducted on whole insects. The entire animal (3 by 7 mm) was well within the sensing field of the rf coil; artifacts of incomplete animal exposure were thus precluded.

3. RESULTS AND DISCUSSION

The proton NMR spectra of two pupae, for the head-up and head-down orientations are shown in Fig. 4.1. The spectra show signals at about 1 PPM and 4.8 PPM due to lipid and water protons respectively. Spectra obtained with the pupae in the head-up orientation also show an increased dispersion and splitting which is more pronounced for the water peak. The orientational differences in the proton spectra were reversible, and were consistent for all viable pupae -- over 50 individuals from two sites, collected over two years; for both light and dark, male and female individuals. The spin-lattice relaxation times determined from another pupa in the head-up orientation were 1.2 and 0.4 s for the water and lipid protons respectively (Fig. 4.2). The decay of the water signal in a Hahn echo experiment with echo times ranging from 2 ms to 120 ms, showed multi-exponential behaviour (Fig. 4.3) suggesting the presence of two distinct water components with spin-spin

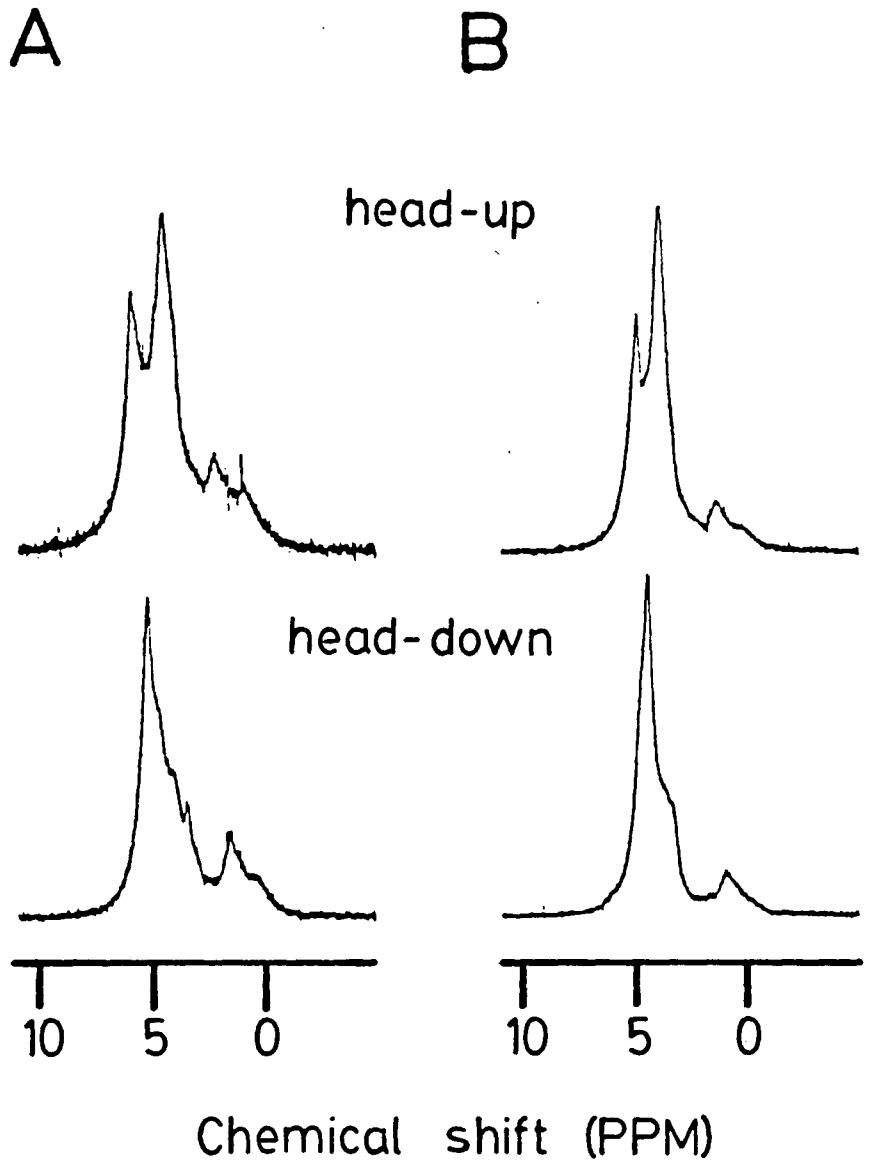

Fig. 4.1 Normal proton spectra of pupae of *Barbara colfaxiana* for the head-up and head-down orientations.

Fig. 4.2 Proton spectra (A) and graphs of peak height *vs* recovery time for water (B) and lipid (C) from inversion-recovery spectra of *Barbara colfaxiana*. The recovery times varied from 7, 12, 17, 22, 32, 42, 52, 77, 102, 152, 202, 252 and 402 ms, 1.0, 1.4, 1.8, 2.2, 2.6 and 3.0 s. Using three parameter fits, the T_1 values were 1.2±0.1 and 0.4±0.04 s for water and fat respectively.

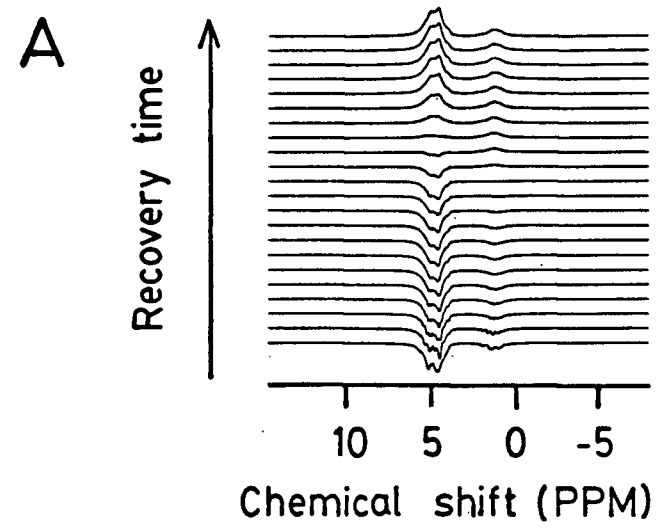
A
Recovery time
10
5
0
-5
Chemical shift (PPM)

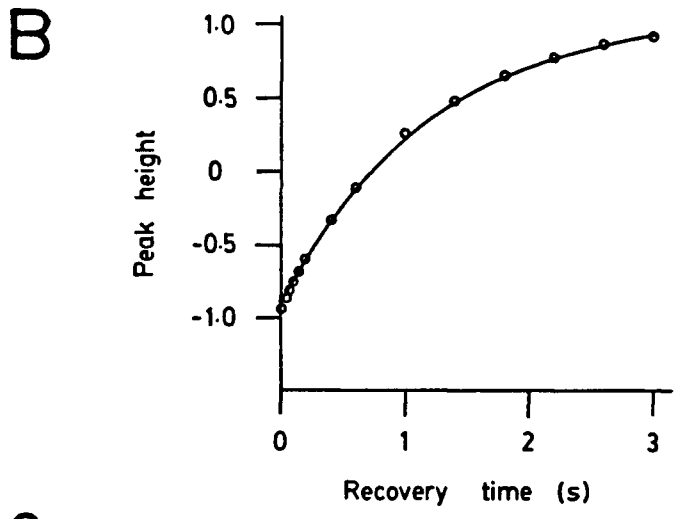
B
1.0
0.5
0
-0.5
-1.0
Peak height
0
1
2
3
Recovery time (s)

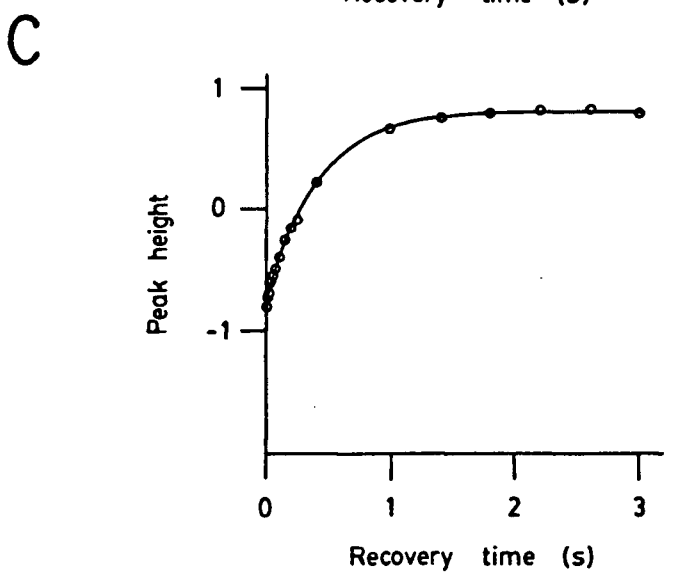
C
1
0
-1
Peak height
0
1
2
3
Recovery time (s)

Fig. 4.3 Proton spectra (A) and plot of peak height *vs* echo time for water (B) and lipid (C) from Hahn echo spectra of *Barbara colfaxiana*. The echo times varied from 2, 4, 8, 12, 16, 20, 24, 30, 36, 44, 52, 60, 70, 80, 90, 100, 110 and 120 ms. The decay of the water signal give two spin-spin relaxation times, 21 and 55 ms, corresponding to 73 % and 27 % of the initial signal and the lipid signal gave a T_2 of 19 ms.

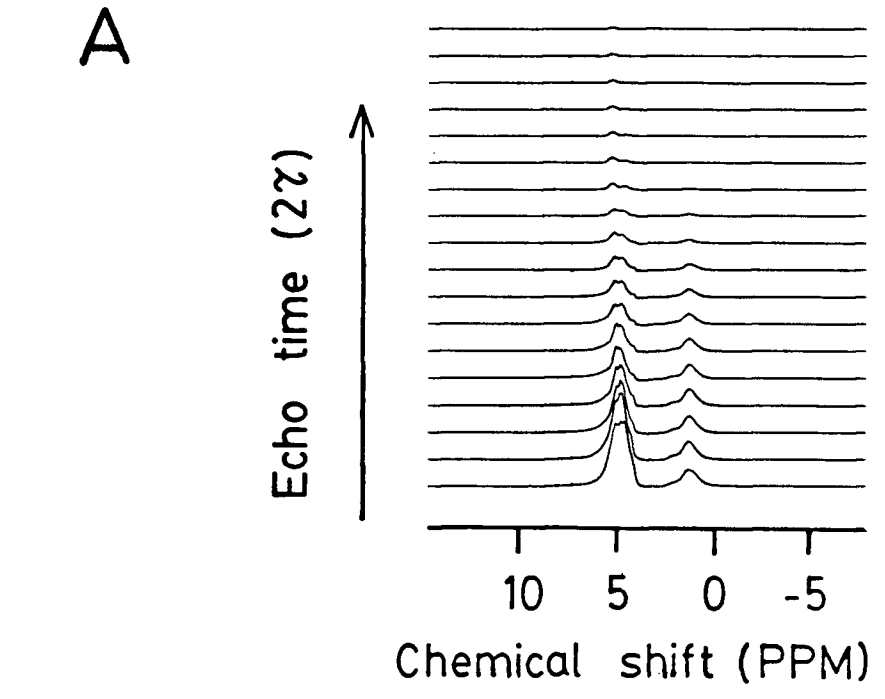
A
Echo time (2τ)
10
5
0
-5
Chemical shift (PPM)

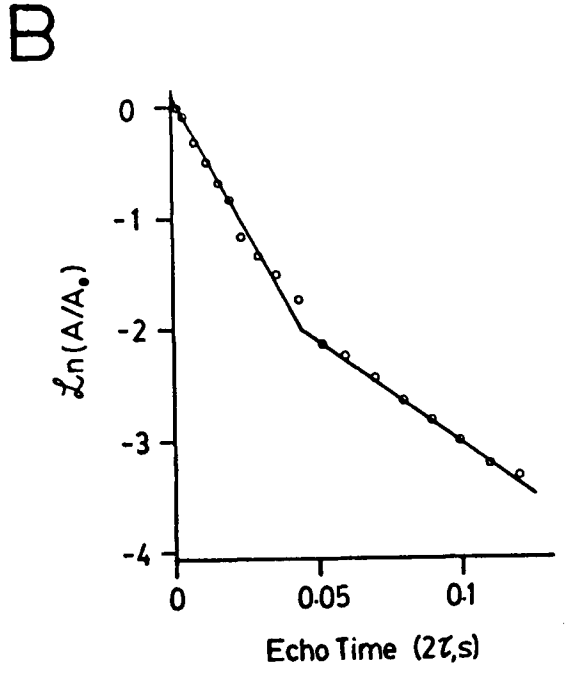
B
0
-1
-2
-3
-4
Ln(A/A₀)
0
0.05
0.1
Echo Time (2τ,s)

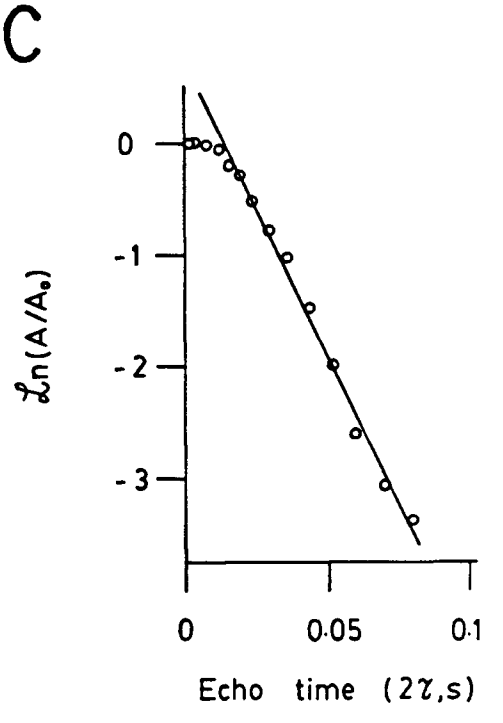
C
0
-1
-2
-3
Ln(A/A₀)
0
0.05
0.1
Echo time (2τ,s)

relaxation times 21 and 55 ms, and corresponding to 73 and 27 % of the observed signal respectively. The T_2 of the lipid protons was 19 ms. The observed linewidths at half height, 280 Hz for water protons and 235 Hz for lipid protons, are much larger than would be expected from the measured spin-spin relaxation times, 15 Hz and 17 Hz respectively. This suggests that magnetic field inhomogeneity is the major factor determining the lineshape and linewidth. The NMR spectrum of haemolymph taken from a pupa using a micropipet is shown in Fig. 4.4. The narrow line observed is further evidence that the broadening of the lines *in-vivo* is due to inhomogeneity.

The distribution of water and lipid along the anteroposterior direction of a healthy pupa, obtained using the pulse sequence of Fig. 2.5, for the head-up and head-down orientations is shown in Fig. 4.5. Comparison of the distributions shows that the lipid reserves are located mainly in the abdomen in both orientations. The aqueous fluids in the upper and lower parts of the pupa are quite well separated and probably correspond to the two components proposed previously to explain the T_2 data.

Comparison of the proton spectra with the distribution maps shows that the changes in the spectra produced by the inversion of the pupae, are associated with the redistribution of the fluids between different parts of the pupae. The resonance frequencies of the water and lipid protons vary continuously between the upper and lower parts

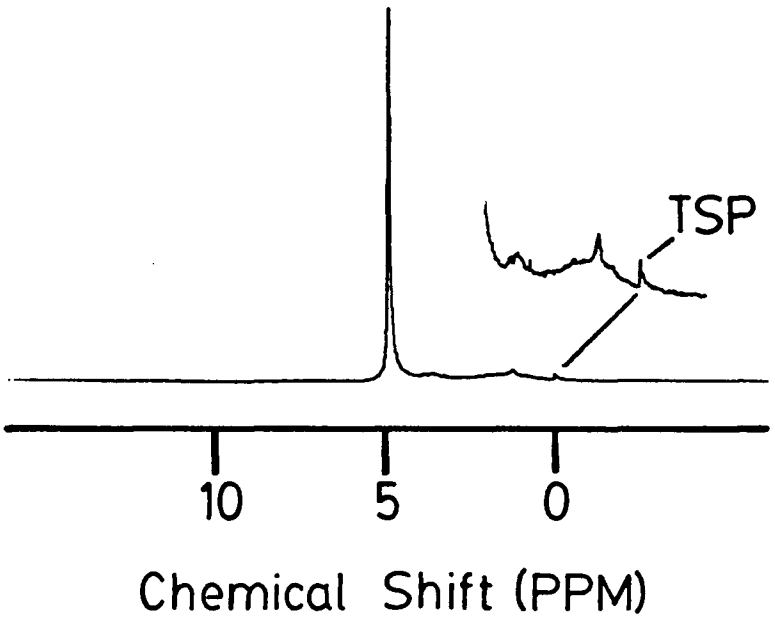

Fig. 4.4 Normal proton spectrum of haemolymph extracted from a pupa of *Barbara colfaxiana*. TSP (Sodium 3 - trimethylsilylpropionate) was added as a reference.

Fig. 4.5 Normal proton spectra and proton distribution maps along the anteroposterior direction of a live *Barbara colfaxiana* pupa in the "head-up" and "head-down" orientations. The maps were acquired using the pulse sequence of Fig. 2.5 with z-gradient increment 1.2 mTm^{-1} and phase encoding time 2 ms, echo time, 16 ms and relaxation delay, 1 s. The field of view was 1.0 cm of which 0.86 cm were displayed. There were 128 gradient increments of four acquisitions and the total time for the experiment was about 17 minutes.

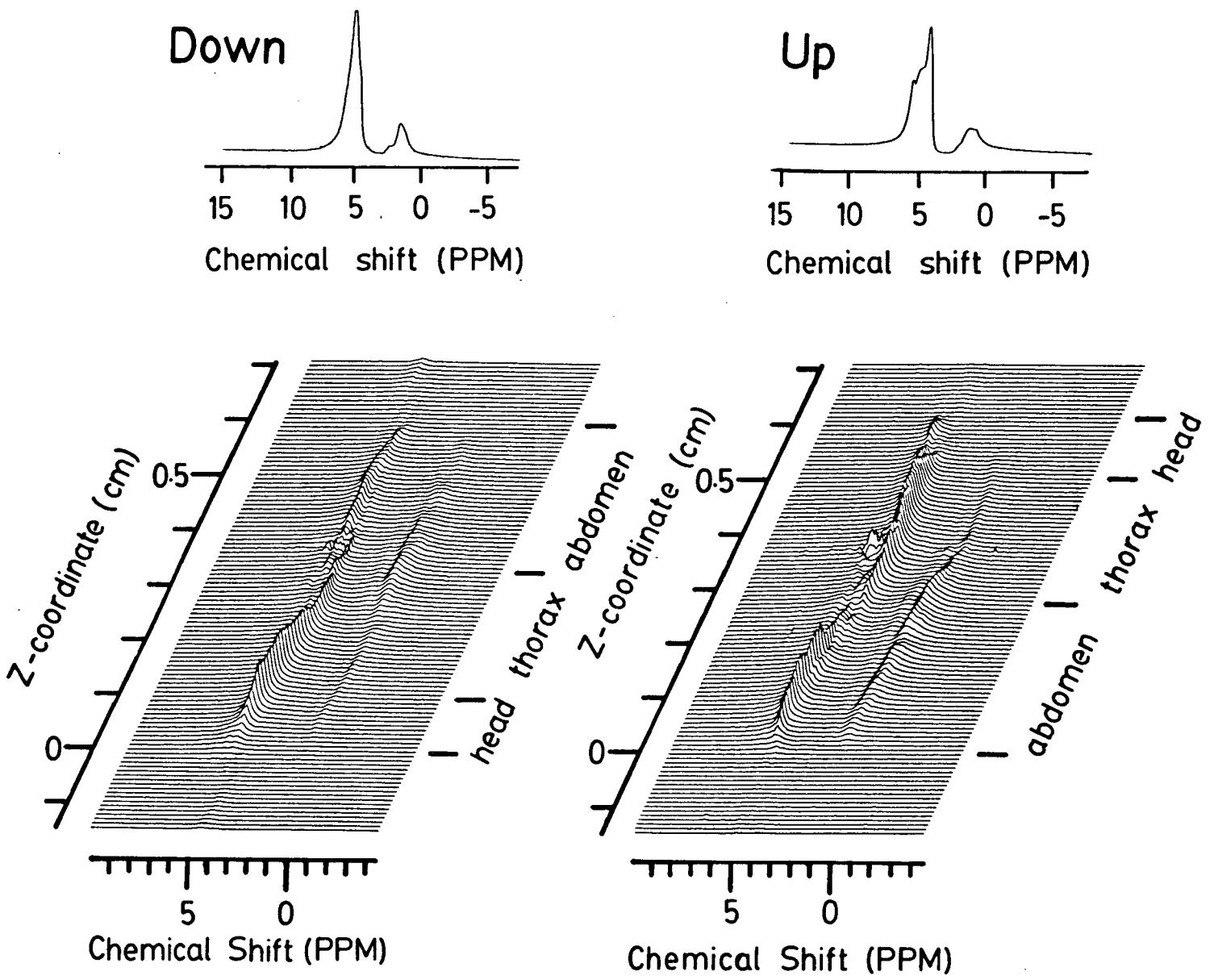
Down
15 10 5 0 -5
Chemical shift (PPM)
Up
15 10 5 0 -5
Chemical shift (PPM)
Z-coordinate (cm)
0.5
0
head thorax abdomen
5 0
Chemical Shift (PPM)
Z-coordinate (cm)
0.5
0
abdomen thorax head
5 0
Chemical Shift (PPM)

of the pupa. Since both the water and lipid resonances are affected in the same way, the variation may be attributed to corresponding changes in magnetic susceptibility. This is more clearly seen in the proton distribution maps (Fig. 4.6) obtained from another pupa, which was removed from a cone several weeks before the experiment was performed. The proton spectrum for this pupa in the head-up orientation also shows an unusual degree of splitting and a corresponding feature at 0.4 cm and 5 PPM is observed in the proton map. A similar feature but with less intensity is also observed in the proton map for the head-down orientation (Fig. 4.6 (A)). The resonance frequencies of the protons in the 0.5 to 3.5 cm region for the head-up orientation (Fig. 4.6 (B)) also show a larger degree of variability compared to that observed in the previous map (Fig. 4.5 (B)). These differences suggest an increased spatial heterogeneity in the pupa of Fig. 4.6 due to a different developmental stage or that the pupa may be dead.

Proton NMR spectra of live and dead pupae are shown in Fig. 4.7 (A)-(D). The first pair of spectra, (A), show a healthy pupa with typical orientational responses. The spectra in (B) and (C) are of the same individual, taken immediately (B), and then twenty minutes (C) after a two minute inmersion in liquid nitrogen. The change in the spectra in (C) with inversion of the pupa is smaller than that in (A), indicating that the distribution of the haemolymph is partly determined by the pupa's heart. The

Fig. 4.6 Normal proton spectra and proton distribution maps along the antero-posterior direction of a *Barbara colfaxiana* pupa, several weeks after harvesting, in the "head-up" and "head-down" orientations. The map was acquired with the pulse sequence of Fig. 2.5 with a z-gradient increment of 1.2 mTm^{-1} with phase encoding time of 2 ms, and echo time 24 ms. The field of view was 0.96 cm of which 0.68 cm are shown. Four acquistions were used for each of the 128 gradient increments and the total time for the experiment was about 17 minutes.

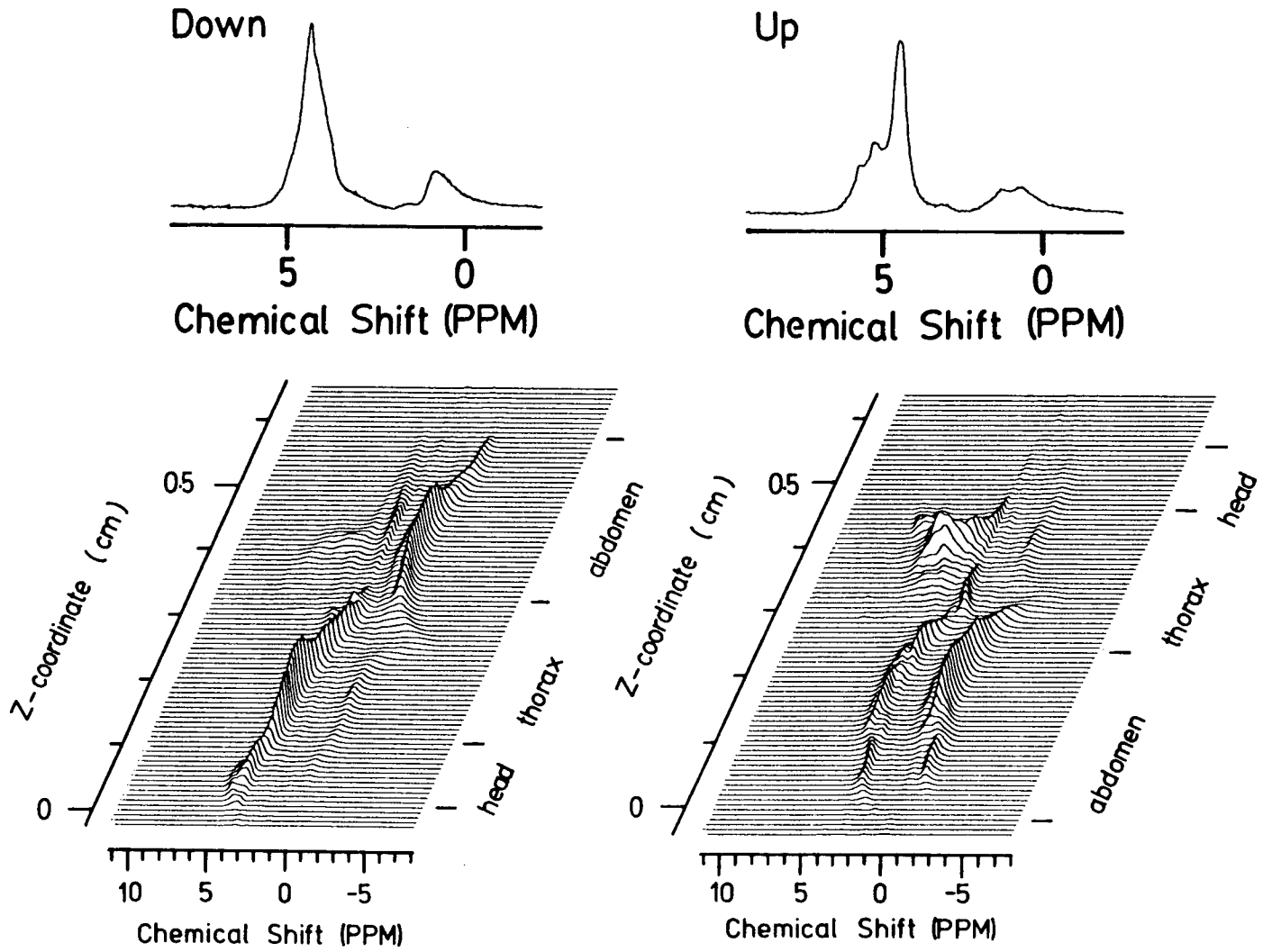
Down
5
0
Chemical Shift (PPM)
Up
5
0
Chemical Shift (PPM)
Z-coordinate (cm)
0.5
0
head
thorax
abdomen
10
5
0
-5
Chemical Shift (PPM)
Z-coordinate (cm)
0.5
0
abdomen
thorax
head
10
5
0
-5
Chemical Shift (PPM)

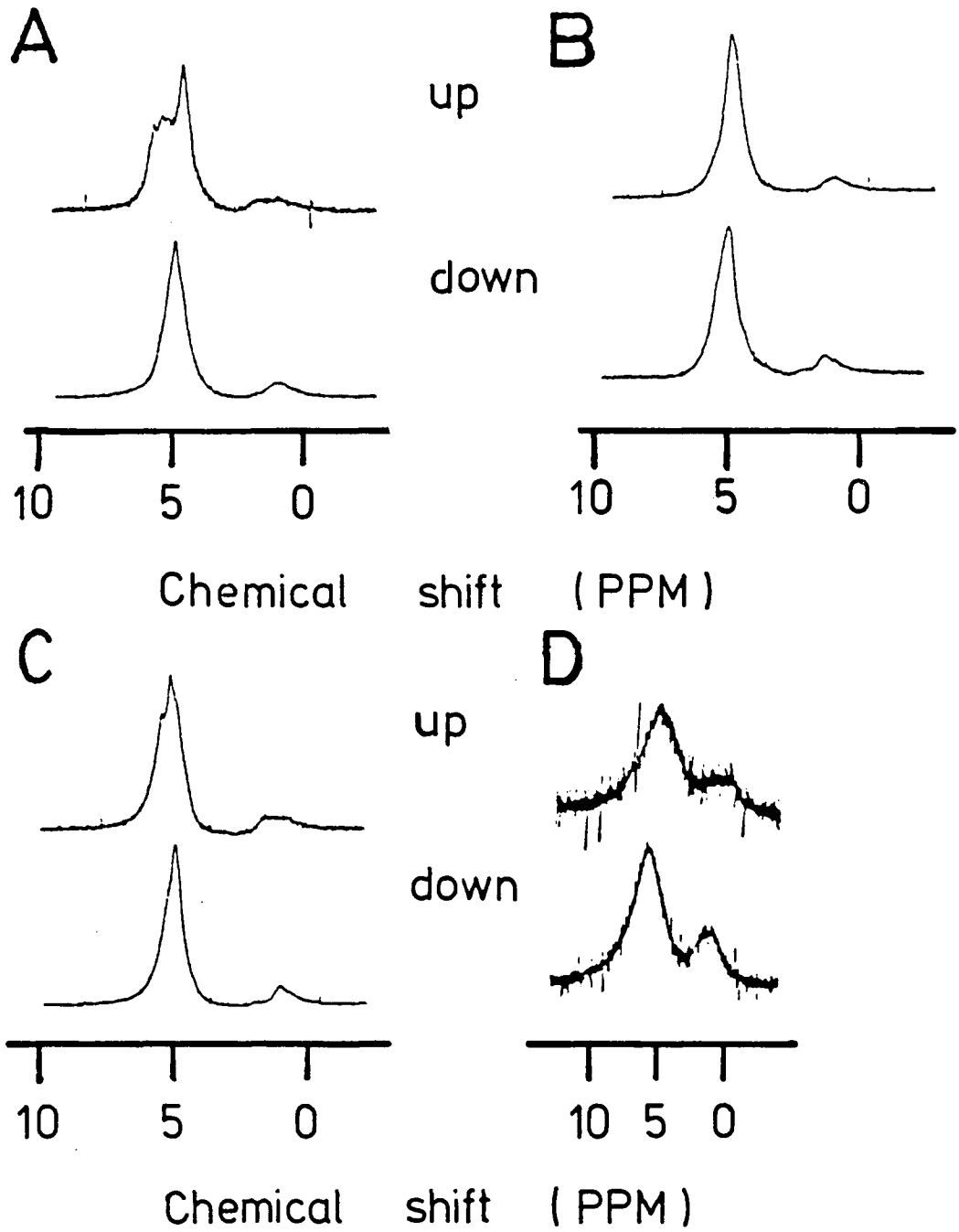

Fig. 4.7 Normal proton spectra of a *Barbara colfaxiana* pupa before (A) and after immersion (B) in liquid nitrogen, and twenty minutes later (C). Spectra in (D) are of a pupa which died of fungal infection.

fourth pair of spectra, (D), are of a pupa that died of a fungal infection, and the reduced signal to noise ratio indicates a loss of body fluids; orientational changes were not observed for this individual.

In conclusion, chemical shift resolved imaging has been used to map the distribution of water and lipid along the anteroposterior direction of *B. colfaxiana* pharate adults. These maps show that the aqueous fluids, consisting mostly of haemolymph, were redistributed when the vertical orientation of the pupae was changed. Variations in the resonance frequencies of the protons probably due to corresponding differences in magnetic susceptibility provided an indicator of spatial heterogeneity.

C. *ACETABULARIA MEDITERRANEA*

1. INTRODUCTION

Acetabularia mediterranea is an unusually large single-celled, marine green alga. Over several months it develops, largely by tip growth, into a cylindrical cell up to 4 cm long and 400 μm in diameter. At the culmination of its vegetative growth, the cell produces at its upper extremity a discoid cap, about 8 mm in diameter and with 40-70 rays. Each ray is about 40 μm wide where it leaves the central stem, and broadens to 400 μm at the periphery. When the cap is fully formed, the rays at first contain continuous cytoplasm with many chloroplasts. The single

nucleus, at the lower extremity of the cell, then divides and numerous daughter nuclei populate the cap rays. Each of these, together with chloroplasts and cytoplasm, becomes encysted in a spherical cyst with a heavy cellulosic wall. The nuclei divide further, and the ultimate daughters are membrane-enclosed to form biflagellate gametes. All the living material is bundled into the rather crowded arrays of multimembranous structures in the cysts; outside, there is only aqueous solution. Water inside the cysts is likely to differ from that outside in ways which affect the various parameters which govern sensitivity in proton magnetic resonance spectroscopy. Without differential sensitivity of different water types, the cap would be a very low contrast object for NMR imaging; it has no dry regions.

Caps vary substantially in shape, from cup-shaped to umbrella-shaped. It is possible to select many which are more or less flat, as was done in this work. Imaging then needs no slice selection and can be achieved two-dimensionally in the plane of the disc (xy plane) with no z-axis spatial discrimination, by projecting the total water signal into the xy plane. The effective spatial resolution can be estimated by comparison of the NMR image with an ordinary photograph, taken in the dissecting microscope.

The cells used in this work are from specimens originally collected in the Bay of Naples, and maintained in culture for many generations, first in Europe, then in the

laboratory of Dr. B.R. Green (Botany, UBC) and currently in the laboratory of Dr. L.G. Harrison (Chemistry, UBC). They are kept in artificial sea-water *(145,146)* called (Shepard's medium) at 20 °C in growth chambers lit at 300-500 ft-candles on a 12:12 light:dark cycle. For imaging, caps were cut off the stalks and kept in Shepard's medium for up to several days.

2. EXPERIMENTAL

Images with T_2 contrasting were obtained by increasing the echo time whilst the inversion-recovery method was used for T_1 contrast. Diffusion contrasting requires two gradient pulses to be applied equally before and after the 180° pulse (Fig 2.8) and this was achieved conveniently using the z gradient, which was not used directly in the imaging.

Experiments were done on caps which were severed from the stalk. For mature caps, the wound at the centre probably never heals. Water inside the outer envelope of the cap, but outside the cysts, is then directly in contact with the surrounding medium. The caps were kept in Shepard's medium. For imaging, they were removed from the medium and mounted on the end of a glass tube which was then placed in the magnet. Contact of the end of this tube with the sample is imaged faintly in Figs. 4.10(B) and very clearly, as a complete circle of 5 mm O.D., in Fig. 4.12(A).

Mounting of the sample in the magnet took only a few minutes. Data acquisition took 17 mins for 128 x 128 points

in the images shown in Figs. 4.10-4.12, using signal averaging of four complete repeats with a 2 s relaxation delay. Specimens lost water during the experiment and were often returned to the medium and used again. The recovery was incomplete and the condition of the caps deteriorated with repeated removal from the medium. This was most clearly seen by their response to brief immersion in Shepard's medium made with D_2O. Water in the cysts of a healthy specimen did not exchange with the D_2O in 5 minutes (Fig. 4.10); but the image of a specimen which had previously been used several times vanished almost completely after this treatment.

The stacked plots required little computer time and demonstrated an effective resolution no better than 0.3-0.4 mm; the count of rays was usually several fewer than those visible in a photomicrograph of the sample. The color-coded images required more computer time and the best contrasted examples gave the same count of rays as the photomicrograph.

3. RESULTS AND DISCUSSION

Proton spectra for one immature and two mature caps are shown in Fig. 4.8. The spin-lattice (T_1) and spin-spin (T_2) relaxation times for mature caps were about 0.58 s and 19 ms respectively (Fig. 4.9). These values are consistent with literature values for intracellular water *(126,127)*. The linewidths of about 1.8 KHz are about 100 times greater than would be expected from the value, 17 Hz from T_2. This

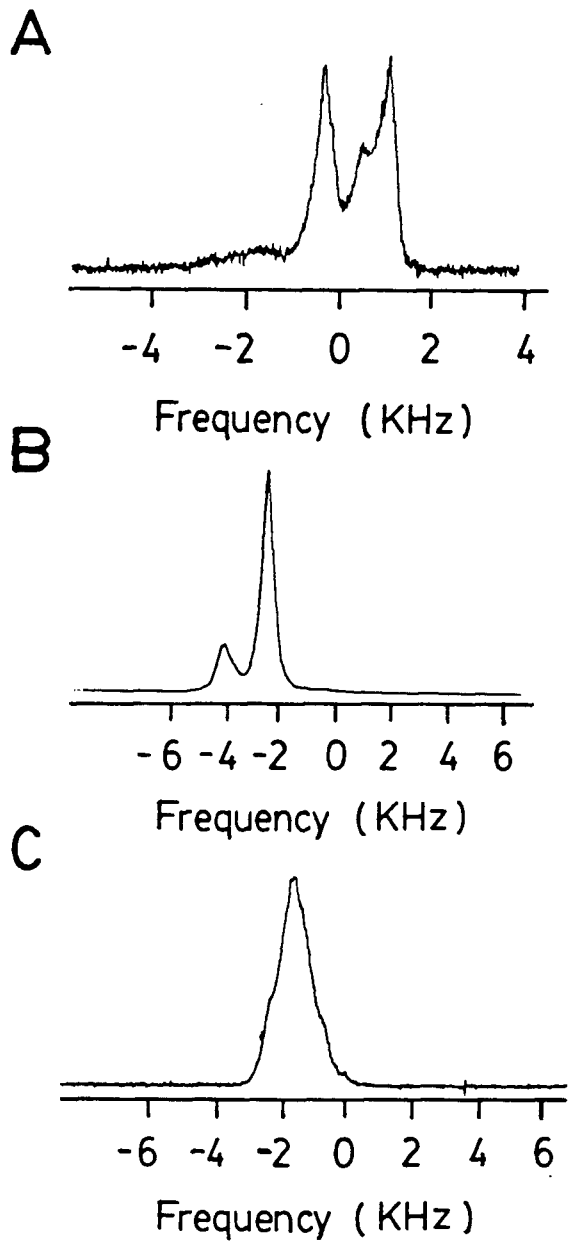

Fig. 4.8 Normal proton spectra for: (A) an immature cap; (B) and (C) two mature caps, acquired with relaxation delay 2 s and 4 complete repeats.

Fig. 4.9 Proton spectra in (A) and graph of intensity *vs* recovery time in (B) from an inversion-recovery NMR experiment on a mature *A. med.* cap. The 90° and 180° pulses were 13 and 27 μs respectively, and the recovery time was varied from 1, 10, 25, 50, 100, 250, 500, to 750 ms and then from 1, 1.5, 2 to 2.5 s. The relaxation delay was 10 s and the calculated T_1 was 0.58 s ± 0.05 s by a three parameter fit.

Hahn echo spectra in (C) and the corresponding plot of echo attenuation *vs* echo time (D) which varied from 2, 4, 8, 12, 16, 20, 30, 40, 50, 60, 70, 80, 90, 100, and 110 ms. The calculated T_2 is 18.7 ms.

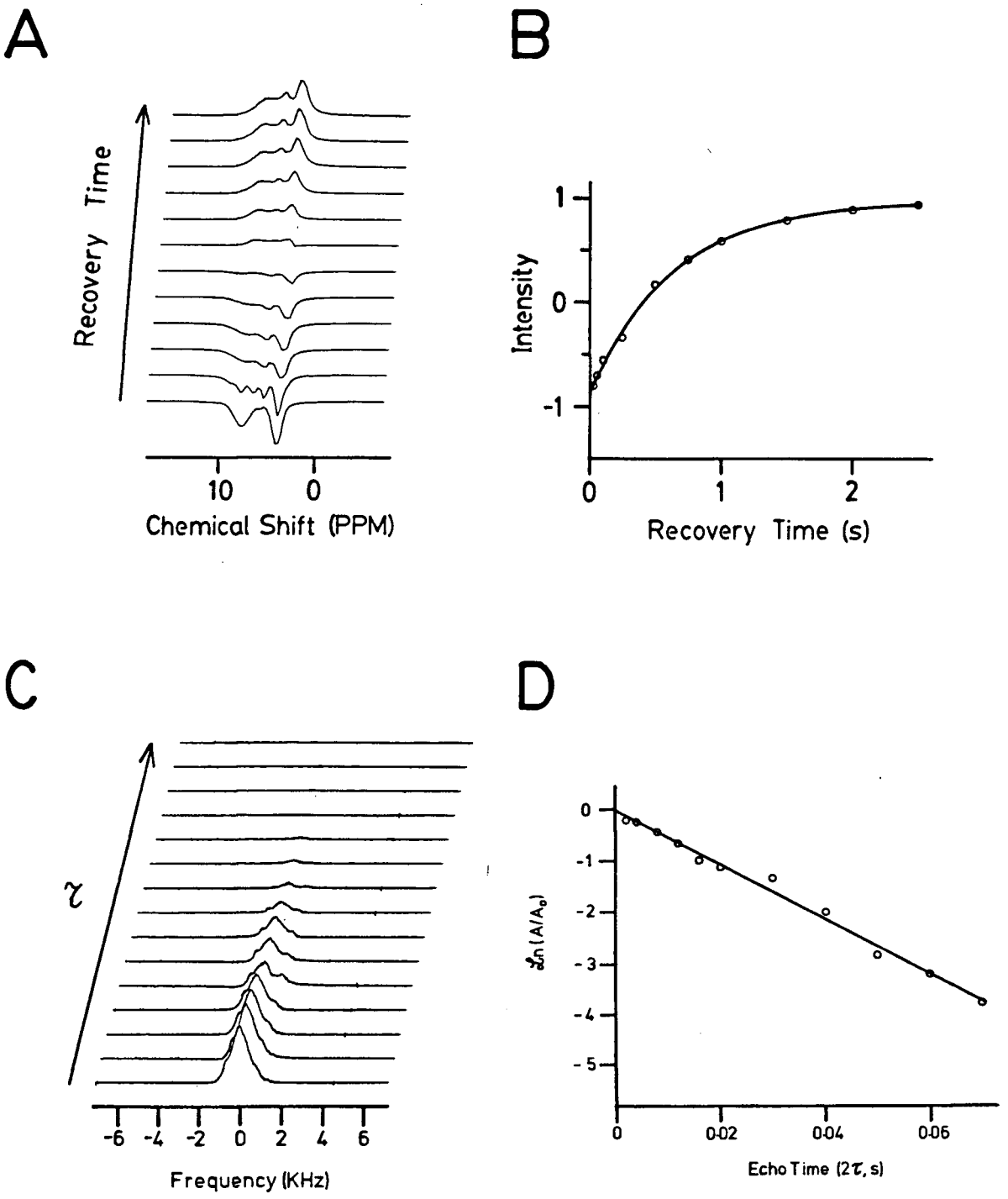
A
Recovery Time
10
0
Chemical Shift (PPM)
B
Intensity
1
0
-1
0
1
2
Recovery Time (s)
C
τ
-6
-4
-2
0
2
4
6
Frequency (KHz)
D
0
-1
-2
-3
-4
-5
0
0·02
0·04
0·06
Echo Time (2τ, s)

indicates that inhomogeneous broadening is the major factor governing the lineshape which varied significantly from one sample to another. The latter was a consequence of differences in the samples and also the positioning on the sample holder. The probable cause of the inhomogeneity are gradients that exist at interfaces due to differences in diamagnetic susceptibility.

A photomicrograph and a deuterium-contrasted image, by the 5 minute immersion in D_2O, of a mature cap are shown in Fig. 4.10. The 47 main clumps of cysts were serially numbered and every ray could be identified as present in both pictures. As the bundles of cysts taper towards the centre of the cap and break up into "dotted lines", it can be seen in the image that the "dots" become confused with spurious noise at about the 0.1 mm level of spatial resolution. In images with T_1 and T_2 contrast (Fig. 4.11), it is not clear whether the "ridges" are the bundles of cysts or the spaces between them. A diffusion contrasted image (Fig. 4.12) with z-gradient pulses of 16 mTm^{-1} and 4 ms long, with echo time 31 ms showed some correspondence; the defective pair of rays at "9 o'clock", which have failed to produce cysts, are clearly visible as low-signal regions in both the "normal" and the diffusion-contrasted image. A "normal" image of a cap with 256 x 256 points is shown in Fig. 4.13. The rays are clearly resolved in two sections and poorly in the remainder of the cap. The uneven intensity and resolution may be due to the drying of the cap during the

Fig. 4.10 (A) Top photograph: Photomicrograph of a mature *A. med.* reproductive cap. The dark patches are bundles of cysts containing essentially all the living material.

(B) Bottom photograph: Proton magnetic resonance image of the same cap, in the same orientation, after 5 min immersion in an artificial sea water medium made with D_2O. The image was acquired with a fixed y-gradient of 10.1 mTm^{-1} with dwell time 22 μs, x-gradient increment of 0.111 mTm^{-1} with phase encoding time 2 ms, echo time 7 ms and relaxation delay of 2 s. Colour-coding: dark is low signal amplitude; light is high signal amplitude. The image is comprised of 128 x 128 data points interpolated to 256 x 256 for display. The vertical line is an image artifact. The white and black lines mark the same feature of the photomicrograph and the image resptively.

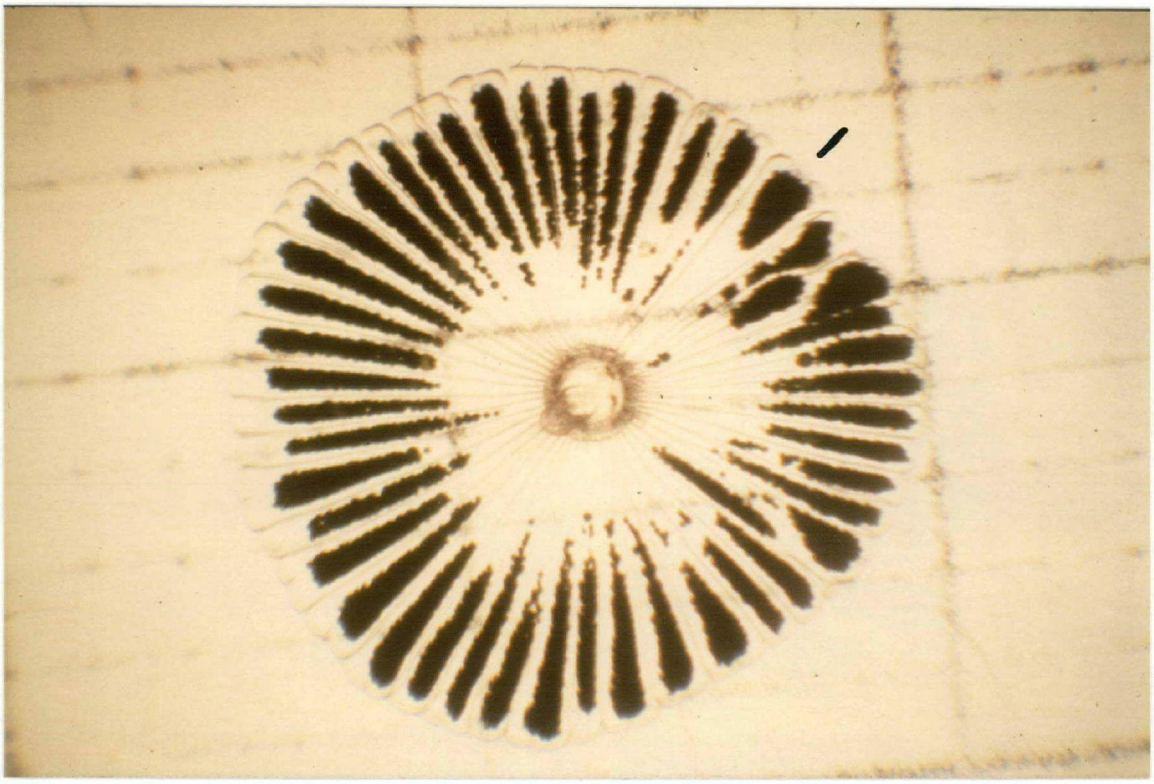

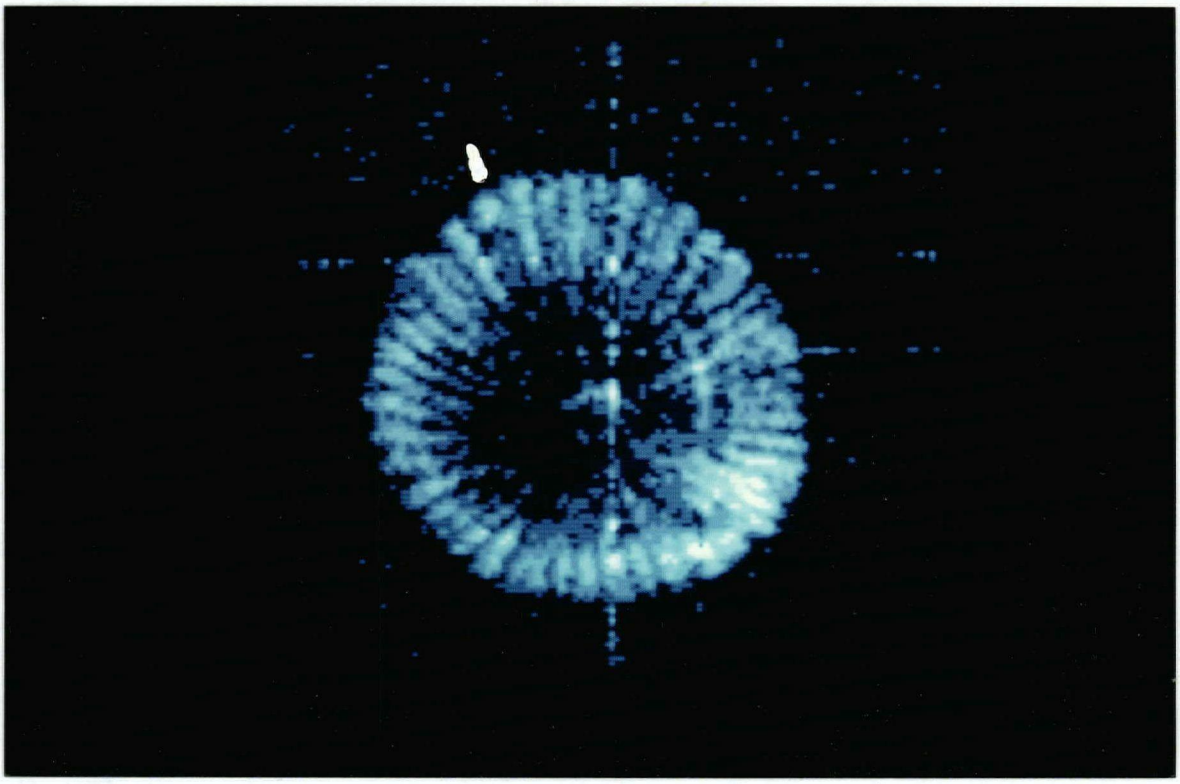

Fig. 4.11 (A) T_1-contrasted image of a mature cap obtained using an inversion pulse followed by a recovery time of 0.3 s. Imaging parameters were a fixed y-gradient of 17.7 mTm^{-1} with dwell time 14 μs, x-gradient increment of 0.124 mTm^{-1} with phase encoding time of 2 ms, echo time 6 ms and relaxation delay of 2 s.
(B) T_2 contrasted image of a mature *Acetabularia mediterranea* cap acquired with a fixed y-gradient of 151 mTm^{-1} and dwell time 16 μs, x-gradient increment 0.48 mTm^{-1} and phase encoding time 5 ms, echo time 32 ms and relaxation delay 2 s. The field of view was 0.97 cm in both the x and y directions.

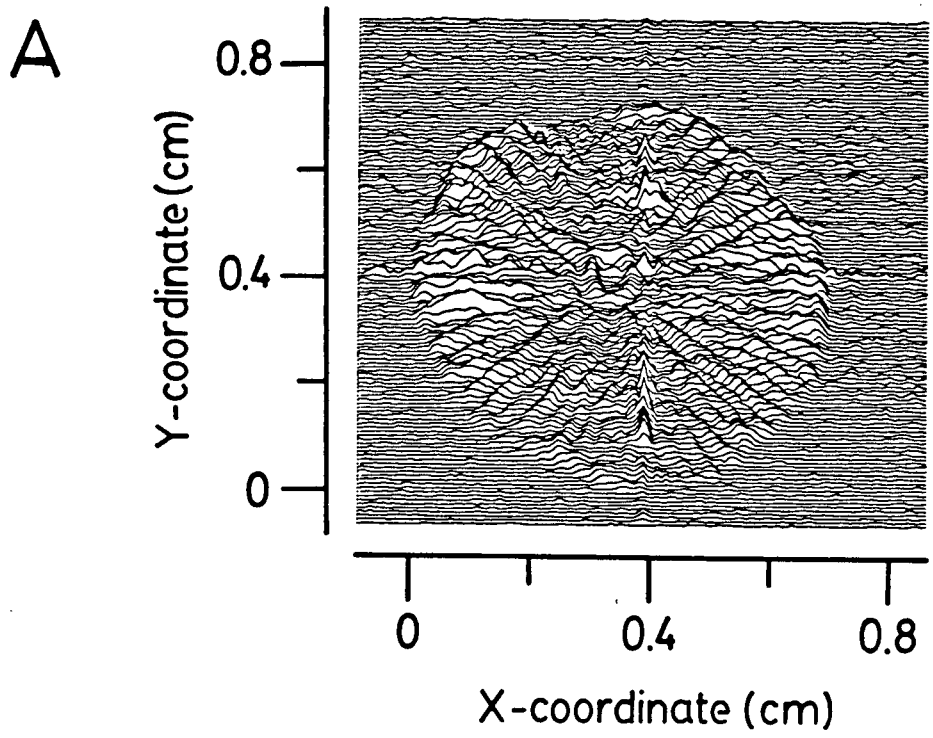
A
0.8
0.4
0
Y-coordinate (cm)
0
0.4
0.8
X-coordinate (cm)

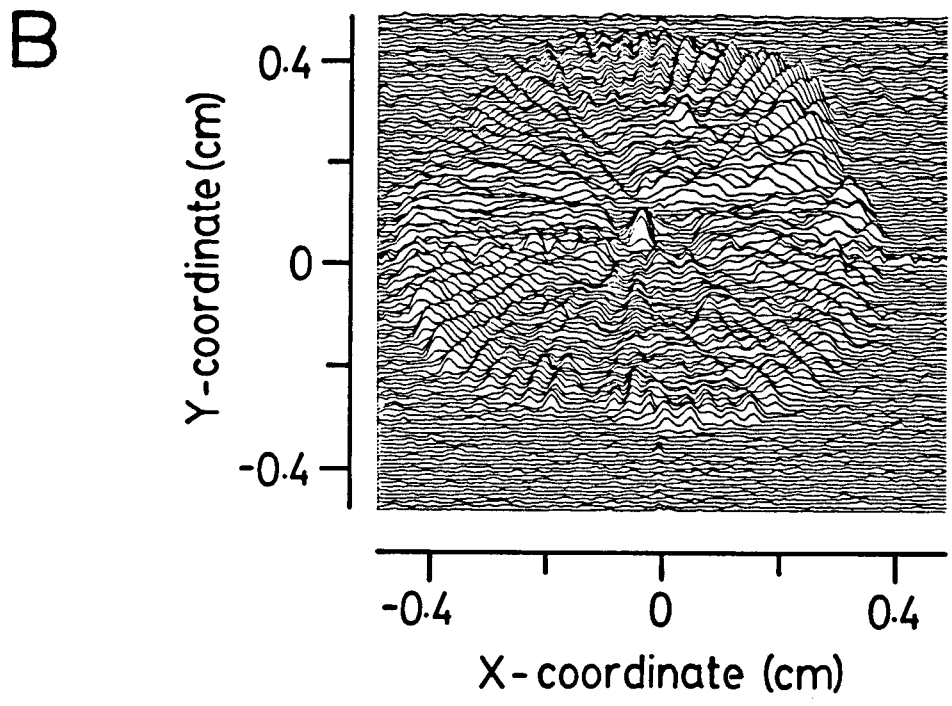
B
0.4
0
-0.4
Y-coordinate (cm)
-0.4
0
0.4
X-coordinate (cm)

Fig. 4.12 (A) Image of a mature cap displayed as 128 plots of signal intensity versus x-coordinate (horizontal), stacked in the y-direction (vertical). The data were acquired using a spin echo sequence with fixed y-gradient of 10.1 mTm^{-1} and dwell time 25 μs, x-gradient increment of 0.126 mTm^{-1} with phase encoding time of 1.5 ms, echo time 7 ms and relaxation delay of 2 s.

(B) Xerographic copy of a photomicrograph of the same cap as (A) and (C), with a scale of mm.

(C) Diffusion-contrasted image of the same cap in the same orientation. The data were acquired with a fixed y-gradient of 10.1 mTm^{-1} with dwell time 24 μs, x-gradient increment of 0.063 mTm^{-1} with phase encoding time 4 ms, echo time 31 ms and relaxation delay 2 s. The z-gradient pulses of 16 mTm^{-1} were 4 ms long, spaced 15.1 ms apart, and applied immediately after the 90° and 180° pulses.

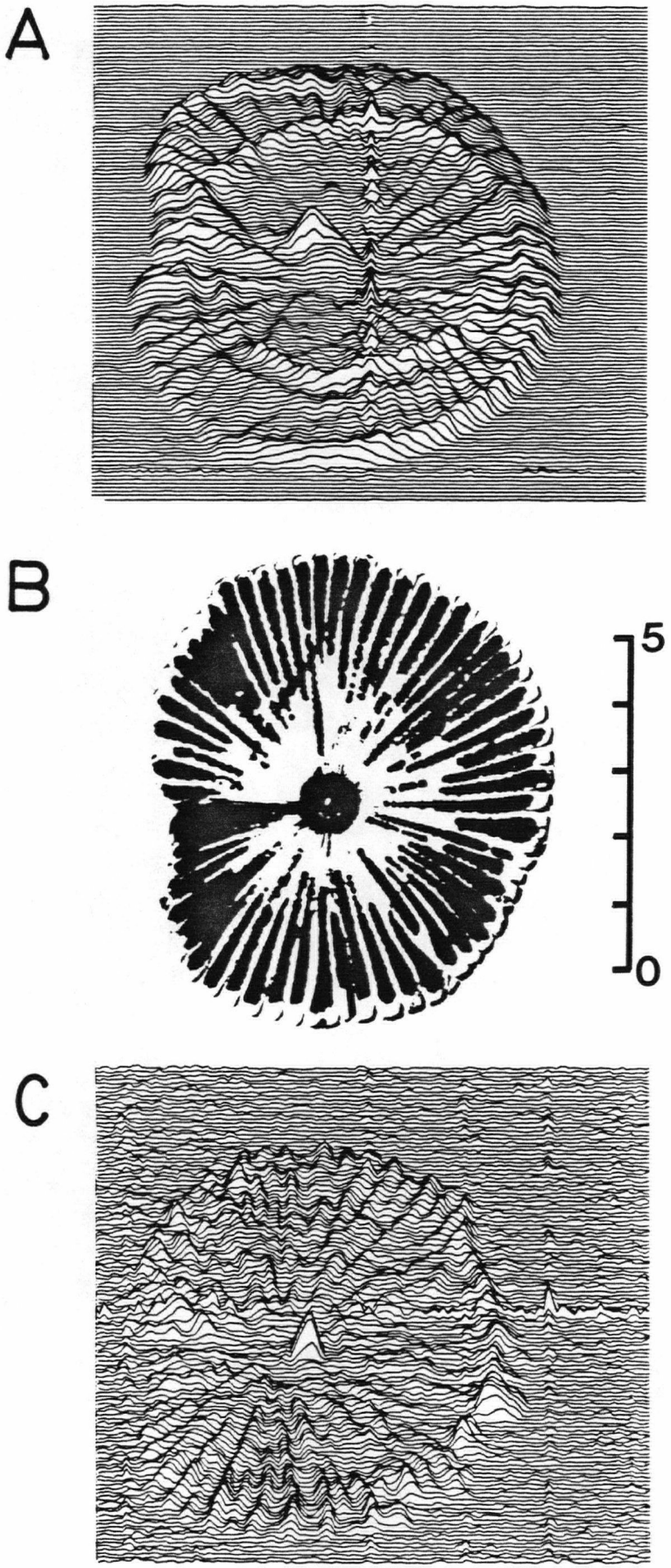
A
B
5
0
C

Fig. 4.13 Normal image of *Acetabularia mediterranea* cap acquired using the pulse sequence of Fig. 2.3 with fixed y-gradient of 151 mTm^{-1} and dwell time 16 μs, x-gradient increment of 1.2 mTm^{-1} and phase encoding time of 2 ms, echo time 8 ms and relaxation delay of 2 s. The image consists of 256 x 256 points and the field of view was 0.97 cm along the x and y directions.

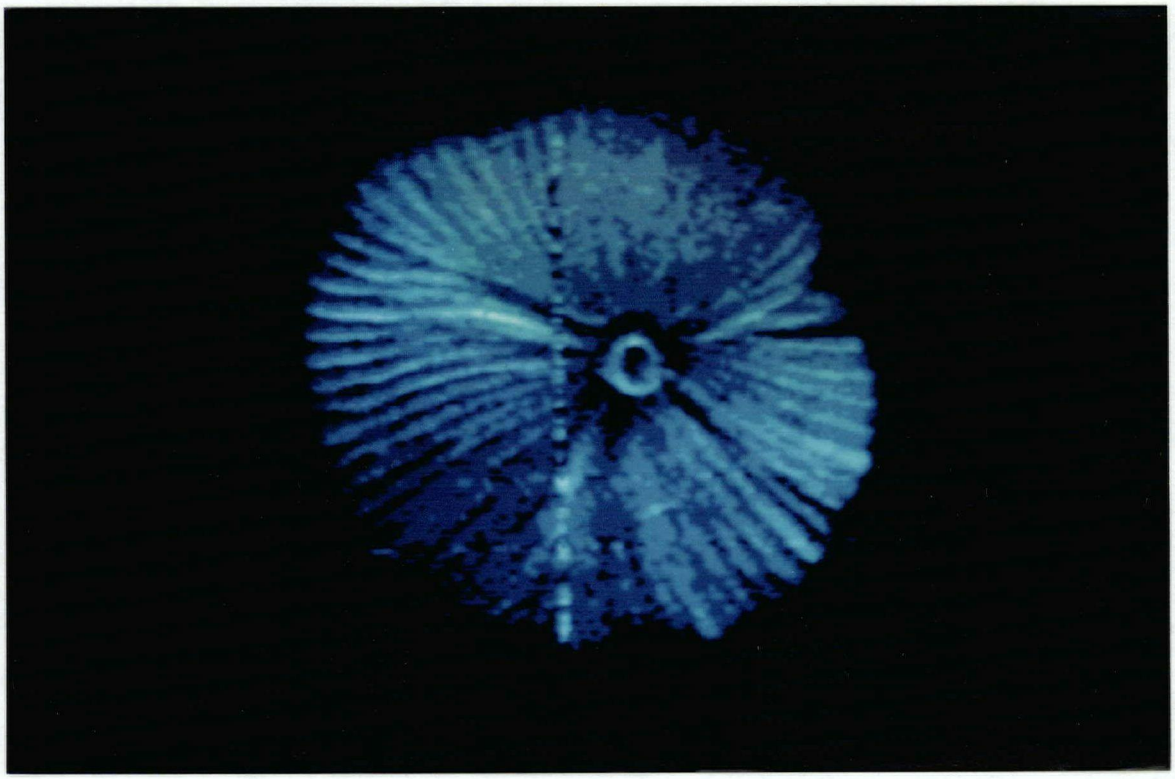

experiment which lasted 34 minutes. Similar intensity variations are observed in the other images but to a lesser extent because the experimental time is less. The signal to noise ratio in normal images, Figs. 4.12(A) and 4.13, was about 25.

Ultimately, the factor limiting resolution is the translational motion of the spins during the intervals for phase encoding and frequency encoding, and also between those intervals. For the frequency encoding gradient only motion during the detection period is important and the initial y-gradient pulse in Fig. 2.2 can be ignored. The pulse sequence in Fig. 2.2 minimized these intervals and for *Acetabularia* times of 4 ms have been achieved. The root-mean-squared displacement for water over that interval is 4.2 μm.

In conclusion, two dimensional NMR images of mature caps of *Acetabularia mediterranea* show features corresponding to the distribution of cysts with spatial resolution of 0.1 mm. Besides signal to noise, a feature limiting image quality is inhomogeneous broadening arising from the variation in diamagnetic susceptibility at the air-cap interface.

CONCLUSIONS

The determination of gradient magnitudes from lineshapes and linewidths gave values which were in agreement with those obtained by calibration using known values for the diffusion coefficient of water. In the study of proton spectra of human forearm, a water signal with T_2 of about 0.8 s was attributed to intercellular water. Measurements of the "diffusivity" of the water suggests that a major part of the motion observed is due to randomized flow in capillaries with a root-mean-square velocity of 0.15 mms^{-1}.

Chemical shift resolved proton maps showing the distribution of water and lipid in the anteroposterior direction of pupae of *Barbara colfaxiana* have been obtained. These maps show that the distribution of the water depended upon the vertical orientation of the pupa. The magnetic susceptibility varied between different parts of the pupa causing the resonance frequencies of the protons to vary correspondingly.

Images of *Acetabularia mediterranea* showed features resembling the radial structure of the caps from mature specimens. The spatial resolution was estimated to be 0.1 mm. For T_1 and T_2 contrasting, it is not clear whether features in the image arise from the groups of cysts within the caps or the spaces between them. D_2O-contrasting gave the best resolution in which the features "highlighted" in the image are probably due to the cysts.

SUGGESTIONS FOR FUTURE WORK

1. IN-VIVO PULSED GRADIENT SPIN ECHO MEASUREMENTS

In-vivo diffusion measurements on the 80 MHz system were complicated by the effects of eddy currents and long echo times were required in order to obtain reliable data. The use of sinusoidal instead of square gradient pulses, because of the less abrupt change will produce less coupling, and reduce eddy currents and acoustical vibration. This should allow more accurate diffusion measurements with shorter echo times. Echo times of 30 to 50 ms would be adequate for the study of restricted diffusion in compartments as small as 10 μm *(24)*, as would be required for measurements of the anisotropic diffusion in muscle cells *(91)*. As described in chapter III, section B, it appears to be feasible, by using long echo times, to suppress the intracellular H_2O signal which has short T_2 and look primarily at blood and other extracellular water, with longer T_2. The existing data showed that the diffusivity of the extracellular water increased with echo time and it was suggested that this might be due to blood undergoing randomly oriented flow instead of motion due to genuine diffusion. Further investigations of these effects may involve measurements over a range of echo times, in the transverse direction of the arm, or with a large proportion of muscle in the sample region, after rest and after

vigorous exercise. Other regions of the arm may also be measured such as over a prominent vein to maximize blood signal; then the flow would be less random.

2. IMAGING

Acetabularia caps proved to be a very suitable object to test "microscopic" spatial resolution of NMR imaging at the 0.1 mm level, because of its size and geometry, and because it could be removed briefly from the H_2O environment without serious damage. Future work on this and other small biological samples could be along three lines:

1) Further work with the same kind of *Acetabularia* sample. Spatial resolution can probably not be improved much, so far as it is determined by instrumental factors with the present equipment because the gradient used is, for this size of coil, the highest compatible with the dwell time of the digitizer, and the rf coil cannot be made smaller because of the sample size. All the possibilities of various kinds of contrasting have not, however, yet been exhaustively investigated. Especially, it is not yet quite certain which parts of the sample, the bundles of cysts or the spaces between them, are highlighted by T_1 and T_2 contrasting, and further work should be done on this.

2) If microscopic NMR imaging is to achieve applicability in developmental biology, especially for animals, it is going

to be necessary to look at samples immersed in aqueous environment. NMR pulse sequences for solvent nulling are not suitable for this application since these rely upon chemical shift differences to selectively prepare transverse magnetization due to the desired component. The problem is to distinguish between water inside and outside the cells and chemical shift differences will be negligible. This may be achieved by adding paramagnetic species to the medium and applying T_2 contrasting to reduce the contribution of the external water; paramagnetic agents which do not diffuse into the cell should be used. *Acetabularia* could serve as a useful sample for preliminary studies of how to eliminate the interference from the aqueous environment. If any of these methods prove successful, so that healthy cells can be studied *in-vivo*, then such properties as the very rapid water transport by cytoplasmic streaming could be studied in the main stalk of this plant, and also in the charophytes (stoneworts) *Chara* and *Nitella*, in which streaming reaches velocities up to 100 μms^{-1}.

3) The spatial resolution may be improved by implementing the following:

a) The sensitivity may be improved by increasing the filling factor (ratio of sample volume to volume of the rf coil) which was about 0.1 for *B. colfaxiana* and *A. mediterranea* samples. This could be achieved by constructing a smaller rf coil preferrably following a solenoidal design; the probe

would then have to be modified to allow insertion of samples from the side.

b) Further improvement may be achieved by increasing the number of scans per gradient increment, the number of points in the image to 512 x 512 and the number of color levels in the displayed image.

c) For imaging of objects 1 mm in size, the existing gradient coils are capable of achieving 400 mTm^{-1} for about 10 A of current. Eddy current effects are likely to present a problem at such gradient magnitudes and a smaller set of gradient coils, radius of about 8-10 mm, should be built.

The implementation of the above, and the attainable spatial resolution will depend upon the characteristics of the sample. In particular, the quantity and partitioning of the water will vary from one sample to another.

Biological systems for study could include immature *Acetabularia* specimens lacking the wide cap and animal embryos. Imaging of the single-cell stage of the embryo of *Xenopus laevis* has already been reported *(139)* and this could be extended to later stages. Many embryos of marine invertebrates, such as echinoderms (e.g. sea urchins and seastars), which are widely studied by developmental biologists, could be suitable objects if the water suppression problems can be solved and resolution improved to tens of microns.

GLOSSARY OF TERMS

Biflagellate gametes: Mature haploid reproductive or sex cells which are motile and possess two flagella (slender, whiplike processes of a cell).

Chloroplast: A type of cell plastid occurring in the green parts of plants, containing chlorophyll pigments, and functioning in photosynthesis and protein synthesis.

Cuticle: A noncellular, hardened or membranous secretion of an epithelial sheet, such as the exoskeleton of arthropods.

Cytoplasm: The living contents of a cell excluding the plasma membrane, vacuoles and nucleus. It is a viscous fluid surrounded by the plasma membrane and contains organelles such as mitochondria, Golgi apparatus, ribosomes.

Diapause: A period of spontaneously suspended growth or development in certain insects, mites, crustanceans and snails.

Eclosion: Emergence of the adult from the pupa case.

Haemolymph: The circulatory fluid of animals with an open circulatory system.

Magnetic susceptibility: Magnetic susceptibility is measured by the ratio of the intensity of the magnetization produced in a susbstance to the magnetizing force or intensity of field to which it is subjected.

Moulting fluids: A fluid which softens the lower layer of the cuticle prior to moulting.

Pharate instar: A stage in the development of an insect during which the cuticle has become separated from the hypodermis but has not yet been ruptured or cast off. A pharate adult is within but free from the pupal integument.

Pupa: A non-feeding and relatively inactive stage between the larva and the adult in Holometabolous insects.

BIBLIOGRAPHY

1. P. Mansfield and P.G. Morris, NMR Imaging in Biomedicine, Academic Press, New York, 1982.

2. P.A. Bottomley, Rev. Sci. Instrum. **53**, 1319 (1982).

3. T.F. Budinger, and P.C. Lauterbur, Science **226**, 288 (1984).

4. R.E. Gordon, Phys. Med. Biol. **30**, 741 (1985).

5. E.O. Stejskal, J. Chem. Phys. **43**, 3597 (1965)

6. K.J. Packer, Mol. Phys. **17**, 355 (1969).

7. D.W. Jones and T.F. Child, Adv. Magn. Reson. **8**, 123 (1976).

8. J.R. Singer, J. Phys. E **11**, 281 (1978).

9. K.J. Packer, C. Rees and D.J. Tomlinson, Advan. Mol. Relaxation Processes **3**, 119 (1972).

10. W.P. Aue, E. Bartholdi and R.R. Ernst, J. Chem. Phys. **64**, 2229 (1976).

11. R. Mills, J. Phys. Chem. 77, 685 (1973).

12. E.O. Stejskal and J.E. Tanner, J. Chem. Phys. **42**, 288(1965).

13. M.I. Hrovat and C.G. Wade, J. Magn. Reson. **44**, 62 (1981).

14. F. Bloch, W.W. Hansen and M. Packard, Phys. Rev. **70**, 474 (1946).

15. E.M. Purcell, H.C. Torrey, and R.V. Pound, Phys. Rev. **69**, 37 (1946).

16. E.L. Hahn, Phys. Rev. **80**, 580 (1950).

17. H.Y. Carr and E.M. Purcell, Phys. Rev. **94**, 630 (1954).

18. D.W. McCall, D.C. Douglas and E.W. Anderson, Ber. Bunsenges. Physik. Chem. **67**, 336 (1963).

19. K. Packer, C. Rees and D.J. Tomlinson, Molec. Phys. **18**, 421 (1970).

20. M.I. Hrovat, C.O. Britt, T.C. Moore and C.G. Wade, J. Magn. Reson. **49**, 411 (1982).

21. D. Zax and A. Pines, J. Chem. Phys. 78, 6333 (1983).

22. J. F. Martin, L.S. Selwyn, R.R. Vold and R.L. Vold, J. Chem. Phys. 76, 2632 (1982).

23. L.W. Reeves, in "Dynamic Nuclear Magnetic Resonance Spectroscopy", Jackman L.M. and Cotton F.A. eds, Academic Press, New York, 1975, p101.

24. J.E. Tanner, in "Magnetic Resonance in Colloid and Interface Science", Resing H.H. and Wade C.G. eds, ACS Symposium Series 1976, p16

25. N.J. Trappeniers, C.J. Gerritsma and P.H. Oosting, Phys. Lett. 18, 256 (1965).

26. J.S. Murday and R.M. Cotts, Z. Naturforsch. A 26, 85 (1971).

27. L. D. Hall and V. Rajanayagam, J. Magn. Reson. 60, 199 (1984).

28. J.S. Murday, J. Magn. Reson. 10, 111 (1973).

29. K.R. Harris, R. Mills, P.J. Back and D.S. Webster, J. Magn. Reson. 29, 473 (1978).

30. P.T. Callaghan, C.M. Trotter and K.W. Jolley, J. Magn. Reson. 37, 247(1980).

31. G. Suryan, Proc. Indian Acad. Sci., Section A 33, 107 (Febuary, 1951).

32. V. Kudravcev and R.L. Bowman, Dig. Tech. Papers, 13th Ann. Conf. Eng. in Med. & Biol., Washington, D. C. (1960), pp. 21 and 25.

33. J.R. Singer, Science 130, 1652 (1959).

34. J.R. Singer and T. Grover, in Modern Developments in Flow Measurement, C.G. Clayton (ed.), London, Peter Peregrinus, 1972, pp. 38.

35. H. van As and T.J. Schaafsma, Bull. Magn. Reson. 2, 359 (1980).

36. J.H. Battocletti, R.E. Halbach, S. Salles-Cunha and A. Sances Jr., Med. Phys. 8, 435 (1981).

37. H. van As and T.J. Schaafsma, in "An Introduction to Biomedical Nuclear Magnetic Resonance", S.B. Petersen, R.N. Muller and P.A. Rinck, eds., George Thieme Verlag, Stuttgart, 1985.

38. J. Stepišnik, Prog. NMR Spectrosc. 17, 187 (1985).

39. R. Gabillard, Phys. Rev. **85**, 694 (1952).

40. P.C. Lauterbur, Nature (London) **242**, 190 (1973)

41. A. Kumar, D. Welti and R.R. Ernst, J. Magn. Reson. **18**, 69 (1975)

42. A. Bax, Two Dimensional NMR, Delft Univ. Press, Delft, The Netherlands, 1982.
K. Nagayama, Adv. Biophys. **14**, 139 (1981).

43. P. Mansfield and P.K. Grannel, J. Phys. C. **6**, L422 (1973)

44. W.S. Hinshaw, J. Apply. Phys. **47**, 3709 (1976).

45. R. Damadian, L. Minkoff, M. Goldsmith, M. Stanford and J. Koutcher, Science **194**, 1430 (1976).

46. A. Abragam, Principles of Nuclear Magnetism, Oxford, London, 1961.

47. C.P. Slichter, Principles of Magnetic Resonance, Springer-Verlag, New York, 1980.

48. U. Fano, Rev. Mod. Phys. **29**, 74 (1957).

49. K. Blum, Density Matrix Theory and Applications, 1981, Plenum Press, New York.

50. I.J. Lowe and R.E. Norberg, Phys. Rev. **107**, 46 (1957).

51. A.G. Redfield and R.K. Gupta, Adv. Magn. Reson. **5**, 81 (1971).

52. F. Bloch, Phys. Rev. **70**, 460 (1946).

53. R.G. Gordon, Adv. Magn. Resonance **3**, 43 (1968).

54. E.L. Hahn and D.E. Maxwell, Phys. Rev. **88**, 1070 (1952).

55. E. Fukushima and S.B.W. Roeder, Experimental Pulse NMR; A Nuts and Bolts Approach, Addison-Wesley, Massachusetts, 1981.

56. P.A. Bottomley, J. Phys. E **14**, 1081 (1981).

57. S. Ljunggren, J. Magn. Reson. **54**, 338 (1983).

58. L.D. Hall, V. Rajanayagam and S. Sukumar, J. Magn. Reson. **61**, 188 (1985).

59. C.D. Eccles and P.T. Callaghan, J. Magn. Reson. **68**, 393 (1986).

60. H.C. Torrey, Phys. Rev. **104**, 563 (1956).

61. D.E. Woessner, J. Phys. Chem. **67**, 1365 (1963).

62. B. Muller and M. Bloom, Can. J. Phys. **38**, 1318 (1960).

63. H.S. Gutowsky, D.W. McCall, and C.P. Slichter, J. Chem. Phys. **21**, 279 (1953).

64. P. Stilbs, J. Colloid Interface Sci. **87**, 383 (1982).

65. P.T. Callaghan, K.W. Jolley and C.M. Trotter, J. Magn. Reson. **39**, 525 (1980).

66. G.E. Wesbey, A. Maudsley and R.L. Ehman, Investigative Radiol. **19**, 491 (1984).

67. D.G. Taylor and M.C. Bushwell, Phys. Med. Biol. **30**, 345 (1985).

68. K. Merboldt, W. Hänicke and J. Frahm, J. Magn. Reson. **64**, 479 (1985).

69. M.H. Levitt and R.R. Ernst, Chem. Phys. Lett 100, **119** (1983).

70. A. Wokaun and R.R. Ernst, Mol. Phys. **36**, 317 (1978)

71. A. Bax, P.G. DeJong, A.F. Mehlkopf and J. Smidt, Chem. Phys. Lett. **69**, 567 (1980).

72. G. Bodenhausen, R.L. Vold and R.R. Vold , J. Magn. Reson. **37**, 93 (1980)

73. S. Vega and A. Pines, J. Chem. Phys. **66**, 5624 (1977).

74. L.E. Kay and J.H. Prestegard, J. Magn. Reson. **67**, 103 (1986).

75. B.C. Sanctuary, J. Chem. Phys. **64**, 4352 (1979).

76. O.W. Sørensen, G.W. Eich, M.H. Levitt, G. Bodenhausen and R.R. Ernst, Prog. NMR Spect. **16**, 163 (1983).

77. D.P. Weitekamp, Adv. Magn. Reson. **11**, 111 (1983).

78. M.H. Levitt and R.R. Ernst, J. Chem. Phys. **83**, 3297 (1985).

79. A.A. Maudsley, A. Wokaun and R.R. Ernst, Chem. Phys. Lett. **55**, 9 (1978).

80. D.I. Hoult and R.E. Richards, Proc. R. Soc. Lond. A. **344**, 311 (1975).

81. D.S. Webster and K.H. Marsden, Rev. Sci. Instrum. **45**, 1232 (1974).

82. G. Ödberg and L. Ödberg, J. Magn. Reson. **16**, 342 (1974).

83. S. Gartenhaus, Physics; Basic Principles. Holt, Rhinehart and Winston. New York, 1977.

84. W.A. Anderson, Rev. Sci. Instr. **32**, 241 (1961).

85. M.J.E. Golay, U.S. Patent, Ser. No. 733 522, (1968).

86. J. L. Evelhoch and J. J. H. Ackerman, J. Magn. Reson. **53**, 52 (1983).

87. A. Haase, W. Hanicke and J. Frahm, J. Magn. Reson. **56**, 401 (1984).

88. G. Levy and I. Peat, J. Magn. Reson. **18**, 500 (1975).

89. M. Bloom, J.H. Davis and M.I. Valic, Can. J. Phys. **58**, 1510 (1980).

90. C. Dumoulin and D. Vatis, Magn. Reson. Med. **3**, 282 (1986).

91. D.B. Chang, R.L. Cooper, A.C. Young, C.J. Martin and B. Ancker-Johnson, J. Theor. Biol. **50**, 285 (1975), R.L. Cooper, D.B. Chang, A.C. Young, C.J. Martin and B.Ancker-Johnson, Biophys. J. **14**, 161 (1974).

92. M.E. Clark, E.E. Burnell, N.R. Chapman and J.A.M. Hinke, Biophys. J. **39**, 289 (1982).

93. R. Mathur-De Vré, Prog. Biophys. Molec. Biol. **35**, 103 (1979).

94. J.E. Tanner, Biophys. J. **28**, 107 (1979).

95. R. Blinc, V. Dimic, J. Pirs, M. Vilfan and I. Zupancic, Molec. Crys. Liq. Crys. **14**, 97 (1971)

96. G. Lindblom and H. Wennerstrom, Biophys. Chem. **6**, 167 (1977).

97. A. Kuo and C.G. Wade, Biochemistry **18**, 2300 (1979).

98. B. Lindman, P. Stilbs and M.E. Moseley, J. Colloid Interface Sci. **83**, 569 (1981).

99. P.T. Callaghan and O. Soderman, J. Phys. Chem. **87**, 1737 (1983)

100. R.D. Ferguson and E. Von Meerwall, J. Polym. Sci. Polym. Phys. Ed. **18**, 1285 (1980)

101. W. Brown and P. Stilbs, Polymer **24**, 188 (1983)

102. P.T. Callaghan and D.N. Pinder, Macromolecules **16**, 968 (1983)

103. P.T. Callaghan and D.N. Pinder, Macromolecules **17**, 431 (1984)

104. J. Tabony and S. Roser, Molec. Phys. **44**, 329(1981)

105. L.D. Bustard, R.M. Cotts and E.F.W. Seymour, Phys. Rev. **22**, 12 (1980)

106. P.A. Hornung, A.D. Khan, D.R. Torgeson and R.G. Barnes, Z. fur Physik. Chemie. Neue Folge, Bd. **116**, 77 (1979)

107. H.G. Hertz, B. Lindman and V. Siepe, Ber. Bunsenges. physik. Chem. **73**, 542 (1969)

108. A. Weiss and K.H. Nothangel, Ber. Bunsenges. physik Chem. **75**, 216 (1971)

109. I. Artaki and J. Jonas, J. Chem. Phys. **82**, 3360 (1985)

110. A. Einstein, Ann. der Physik (Leipzig) **17**, 549 (1905). Translated in R. Furth, ed., "Investigations on the Brownian Movement". Methuen, London, 1926.
J. Perrin, "Atoms" (D.L. Hammick, translator). Van Nostrand, New York, 1916.

111. R. Zwanzig and A.K. Harrison, J. Chem. Phys. **83**, 5861 (1985).

112. G.L. Pollack and J.J. Enyeart, Phys. Rev. A **31**, 980 (1985).

113. J.T. Edward, J. Chem. Ed. **47**, 261 (1970).

114. M.J. Tait, A. Suggett, F. Franks, S. Ablett and P.A. Quickenden, J. Solution Chem. **1**, 131 (1972).

115. H. Uedaira and H. Uedaira, J. Solution Chem. **14**, 27 (1985).

116. M. Windholz, ed., "The Merck Index, An Encylopedia of Chemicals and Drugs", Merck & Co., Inc., New Jersey, 9th edition, 1976.

117. J.K. Gladden and M. Dole, J. Amer. Chem. Soc. **75**, 3900 (1953).

118. L. Freidman and P.G. Carpenter, J. Amer. Chem. Soc. **61**, 1745 (1939).

119. J.J.H. Ackerman, T.H. Grove, G.G. Wong, D.G. Gadian and

G.K. Radda, Nature(London) 283, 167 (1980); R.E. Gordon, P.E. Hanley, D. Shaw, D.G. Gadian, G.K. Radda, P. Styles, P.J. Bore, and L. Chan, ibid. 287, 736 (1980).

120. S.R. Williams, D.G. Gadian, E. Proctor, D.B. Sprague, D.F. Talbot, I.R. Young and F.F. Brown, J. Magn. Reson. 63, 406 (1985).

121. J.C. Grant, Grant's Atlas of Anatomy, Sixth ed., The Williams and Wilkins Co., Baltimore, 1972.

122. W.F. Ganong, Review of Medical physiology, Lange Medical Publications, Los Altos, California, 1981, p.12

123. W.A.R. Thomsod, ed., Black's Medical Dictionary, A. and C. Black Ltd., London, 1984.

124. K.J. Packer, Phil. Trans. R. Soc. Lond. B. 278, 59 (1977).

125. J.R. Zimmerman and W.E. Brittin, J. Phys. Chem. 61, 1328 (1957).

126. E.E. Burnell, M.E. Clark, J.A.M. Hinke and N.R. Chapman, Biophys. J. 33, 1 (1981).

127. K.R. Foster, H.A. Resing and A.N. Garroway, Science 194, 324 (1976).

128. M. Bloom, K.T. Holmes, C.E. Mountford and P.G. Williams, J. Magn. Reson. 69, 73 (1986).

129. B. Alberts, D. Bray, J. Lewis, M. Raff, K. Roberts, J.D. Watson, Molecular Biology of the Cell, Garland Publishing, New York, (1983).

130. R.F. Steiner and S. Pomerantz, The Chemitry of Living Systems, D. Van Nostrand, New York, 1981.

131. A.C. Guyton, Textbook of Medical Physiology, Sixth ed., W.B. Saunders Co., 1981.

132. G.G. Cleveland, D.C. Chang, C.F. Hazelwood and H.E. Rorsach, Biophys. J. 16, 1043 (1976).

133. J.E. Tanner, Biophys. J. 28, 107 (1979).

134. K. Yoshizaki, Y. Seo, H. Nishikawa and T. Morimoto, Biophys. J. 38, 209 (1982).

135. K. Diem and C. Leutner (Eds.), "Documenta Geigy Scientific Tables", Gregory, Basel, (1970) p. 517.

136. P.L. Altman and D.S. Dittmev (Eds.), "Biology Data Book

2", Fed. of Amer. Soc. for Exp. Biol., Bethesda, Maryland, (1973) p. 1206.

137. R.C. Weast, Ed., CRC Hanbook of Chemistry and Physics, 58th ed., CRC Press, Palm Beach, (1977).

138. N. Kamiya, Annu. Rev. Plant Physiol. **32**, 205 (1981).

139. J.B. Aguayo, S.J. Blackband, J. Schoeniger, M.A. Mattingly and M. Hinterman, Nature **322**, 190 (1986).

140. T.S. Sahota, D.S. Ruth, A. Ibaraki, S.H. Farris and F.G. Peet, Can. Ent. **114**, 1179 (1982).

141. D. N. Radcliff, Can. Dep. Agric., For. Biol. Div., Bi-mon. Prog. Rep. **8**, 3 (1952).

142. A.F. Hedlin, Can. Ent. **92**, 826 (1960).

143. A.F. Hedlin *et al.*, Can. For. Serv. Ottawa, **60** (1980).

144. T.S. Sahota, A. Ibaraki and S.H. Farris, Can. Ent. **117**, 873 (1985).

145. B.R. Green, Phycologia **16**, 87 (1977).

146. D.S. Shepard, Methods of Cell Physiol., vol. IV (D. Prescott, ed.), Academic Press, New York, 1970, p. 49.